UNIVERSIDADE FEDERAL FLUMINENSE
INSTITUTO DE FÍSICA
DOUTORADO EM FÍSICA

HUGO SOLER DE OLIVEIRA

Reaction mechanisms in neutron-rich nuclei

Niterói-RJ
2023

HUGO SOLER DE OLIVEIRA

Reaction mechanisms in neutron-rich nuclei

Tese realizada sob orientação do Prof. Dr. Jesús Lubián Ríos, apresentada ao Departamento de Física, em complementação aos requisitos para obtenção do título de Doutor em Física.

Orientador:
Prof. Dr. JESÚS LUBIÁN RÍOS

Niterói-RJ
2023

Ficha catalográfica automática - SDC/BIF
Gerada com informações fornecidas pelo autor

O48r Oliveira, Hugo Soler de
Reaction mechanisms in neutron-rich nuclei / Hugo Soler de Oliveira. - 2023.
98 f.: il.

Orientador: Jesús Lubián Ríos.
Tese (doutorado)-Universidade Federal Fluminense, Instituto de Física, Niterói, 2023.

1. Neutron-rich nuclei. 2. Nuclear fusion. 3. Transfer reactions. 4. CDCC. 5. Produção intelectual. I. Ríos, Jesús Lubián, orientador. II. Universidade Federal Fluminense. Instituto de Física. III. Título.

CDD - XXX

Bibliotecário responsável: Debora do Nascimento - CRB7/6368

Hugo Soler de Oliveira

Reaction mechanisms in neutron-rich nuclei

Aprovada em ——.

BANCA EXAMINADORA

Prof. Dr. Jesús Lubián Ríos
Orientador

Sergio Jose Barbosa Duarte
Centro Brasileiro de Pesquisas Físicas

Jeannie Rangel Borges
Universidade do Estado do Rio de Janeiro

Luiz Felipe Alvahydo de Ulhoa Canto
Universidade Federal Fluminense

Vinicius Antonio Bocaline Zagatto
Universidade Federal Fluminense

Niterói-RJ
2023

"Time is the cruelest force of all."

Cixin Liu, Death's End

Acknowledgment

Primeiramente, agradeço ao meu avô, que infelizmente não está mais presente, mas cuja memória estará sempre viva em mim enquanto eu estiver aqui.

À minha companheira, Isabella, sou imensamente grato por todo o apoio, carinho e compreensão que me proporciona.

À minha mãe, por todo o amor, carinho e apoio incondicional ao longo desta jornada.

Ao meu orientador, agradeço por sua orientação constante e espero que continue a me aturar no futuro próximo.

À professora Manuela Rodríguez, que desempenhou um papel fundamental na construção deste trabalho, sou imensamente grato por sua ajuda e contribuições.

Agradeço a todos os meus professores, cujos ensinamentos foram essenciais para expandir meus conhecimentos e reduzir minha ignorância.

Aos meus colaboradores, agradeço por compartilharem seu conhecimento e acredito que ainda tenho muito a aprender com eles.

Por fim, aos meus amigos, que trazem sentido à vida mesmo em meio ao caos, agradeço por sua amizade e apoio contínuos.

Minha gratidão a todos vocês é imensurável.

Hugo Soler de Oliveira

Resumo

Reações nucleares envolvendo núcleos ricos em nêutrons desempenham um papel crucial no estudo da física nuclear, astrofísica e tecnologia nuclear. Nesta tese, investigamos o comportamento de núcleos ricos em nêutrons em reações nucleares usando algumas ferramentas teóricas. Canais acoplados, canais de reação acoplados e canais acoplados discretizados em 3 e 4 corpos (CDCC) são usados com sucesso para descrever reações envolvendo um grande número de sistemas. Este trabalho aplica esses métodos em alguns sistemas e, quando possível, compara os resultados com dados experimentais.

Este trabalho analisa as seções de choque elástica, inelástica, de transferência de um nêutron (*stripping* e *pickup*), fusão completa e incompleta para o sistema ^{9}Be+^{197}Au. Dados experimentais foram relatados para todos esses mecanismos de reação. Cálculos de canal acoplado foram usados para determinar as seções de choque elástica, inelástica e de transferência. Cálculos de canal de reação acoplada foram realizados para derivar as seções de remoção e captura de um nêutron. Cálculos de canais acoplados discretizados em 3 corpos foram usados para determinar o efeito do canal de quebra em outros mecanismos de reação. A fusão completa e total mostraram-se suprimidas acima e incrementada abaixo da barreira Coulombiana em comparação com a *Universal Fusion Functions*.

Além disso, a influência dos efeitos de camada na fusão de núcleos de massa média é explorada usando cadeias isotópicas de íons K e Ar em um alvo de oxigênio e silício. A seção de choque de fusão para os projéteis de camada de nêutrons fechada é menor do que para a camada de nêutrons aberta. O potencial de São Paulo não mostra uma boa descrição para os dados experimentais. Para o alvo de oxigênio, o uso de densidades mais realistas obtidos através de uma abordagem Dirac-Hartree-Bogoliubov melhora significativamente a descrição dos dados experimentais. No entanto, para o alvo de silício, subestima significativamente a seção de fusão para núcleos de camada aberta.

Finalmente, para descrever a reação envolvendo o projétil instável e rico em nêutrons ^{6}He e os alvos ^{208}Pb e ^{197}Au, é aplicado o CDCC de 4 corpos. Para discretizar o contínuo, são usados métodos bin. Nesse tipo de discretização, é necessário truncar o hiper-momento. Por causa disso, é feito um estudo sistemático da importância do hiper-momento máximo considerado nos observáveis. Alguns dados experimentais para a seção de choque elástica para esse sistema são relatados, e é observado um bom acordo entre os dados experimentais e os cálculos teóricos.

Abstract

Nuclear reactions involving neutron-rich nuclei play a crucial role in studying nuclear physics, astrophysics, and nuclear technology. In this thesis, we investigate the behavior of neutron-rich nuclei in nuclear reactions using some theoretical tools. Coupled channels, coupled reaction channels, and 3- and 4-body continuum discretized coupled channels (CDCC) are successfully used to describe reactions involving a large number of systems. This work applies these methods in some systems and, when possible, compare the results with experimental data.

This work analyzes the elastic, inelastic, one-neutron transfer (pickup and stripping), complete and incomplete fusion cross sections for the ^{9}Be+^{197}Au system. Experimental data were reported for all these reactions mechanism. Coupled-channel calculations were used to determine the elastic, inelastic, and transfer cross sections. Coupled reaction channel calculations were performed to derive the one-neutron stripping and pickup cross sections. The reduced complete and total fusion were found to be hindered above and enhanced below the Coulomb barrier compared with the universal fusion function.

Also, the influence of shell effects on the fusion of mid-mass nuclei is explored using isotopic chains of K and Ar ions on an oxygen and silicon target. The fusion cross section for the closed neutron shell projectiles is smaller than for the open neutron shell. The São Paulo systematic does not show a good description for the experimental data. For the oxygen target, using more realistic densities from a Dirac-Hartree-Bogoliubov approach significantly improves the description of the experimental data. Yet, for the silicon target, significantly underpredict the fusion cross section for open-shell nuclei.

Finally, to describe the reaction involving the unstable neutron-rich ^{6}He projectile and ^{208}Pb, and ^{197}Au targets it is applied the 4-body CDCC. To discretize the continuum it is used the bin methods. In this type of discretization, it is necessary to truncate the hypermomentum. Because of that, it is made a systematic study of the importance of the maximum hypermomentum considered in the observables. Some experimental data for the elastic cross section for this system are reported, and it is observed a good agreement between the experimental data and the theoretical calculations.

List of Figures

List of Tables

Contents

Chapter 1
Introduction

The divisibility of the matter is a subject that has fascinated humanity since antiquity. Atomism was a natural philosophy that proposed that the universe is composed of fundamental, indivisible components, the atom. This concept appeared separately in both ancient Greek and ancient India. In India, some philosophical currents defended the idea of atomism. For the Greeks, Democritus (546-460 B.C.) idealized a minor divisible part of the matter. This conception was largely diffused by natural philosophers, mathematicians, and later physicists. However, most of the time, without any empirical proof. Nevertheless, this concept led to a discovery even in math with the idealization of a mathematical atom, the infinitesimal number that led to the creation of calculus [11].

The first big step of the atom idea in physics was the discovery of radiation by Becquerel (1852-1908) in 1896 [12]. This discovery earned him the Nobel prize in 1903, with the Marie Curie (1867-1934) and Pierre Curie (1859-1906). Later, J. J. Thomson (1856-1940) showed that cathode rays were composed of negative particles called electrons [13]. That was followed by the discovery of the atom in the plum pudding model [14].

Ernest Rutherford (1871-1937) proposed that the positive charge of the nucleus is concentrated in a small region in the center of the atom, the atom nucleus [15]. Also, Rutherford realized the transmutation of matter [16], which can be considered the beginner of nuclear physics and the death of the idea that the physical atom was indivisible. Still, in the standard model, the concept of an atom exists, but in physics, it is called an elementary particle. The elementary particles are particles that do not have any substructure. In other words, particles are not composed of other smaller particles. However, some researchers are still looking for substructure in the actual elementary particles, and one famous example is the string theory.

In the last century, many discoveries have been made in nuclear physics. However, we still need a global model that includes all the nuclear phenomena, motivating the hard effort of many scientists to investigate that area. The vast applicability boosts investment in nuclear physics. Since it has many applications, like the dating by radioactive isotopes, carbon dating was used to measure the age of many objects and lead dating that was used to determine the Earth's age. In medicine are used for the treatment of cancer, detection of diseases using radioactive isotopes, and others.

Another area in which nuclear physicists are interested is astrophysics. The nucleosynthesis of the light nucleus is very important to understand the primordial Universe [17]. The formation of hydrogen, helium, and perhaps lithium nuclei is due to the combination of protons and neutrons in the initial minutes of the universe when the av-

erage thermal energy is about 1 MeV. On the other hand, the hydrogen burns inside the stars, winning the gravity force and maintaining the star structure. This amount of energy released in the stars results from several nuclear reactions, such as the proton-proton chains, that is, the conversion of 4 protons (and two electrons) in one alpha(α) particle, two positrons, two neutrinos, and 26 MeV of released energy. Other chains are the CNO and Triple-α. It is important to note that chains are composed of a few direct nuclear reactions. The synthesis of the heavier nucleus is essential too. In this synthesis, the unstable and weakly-bound nucleus plays an important role. In this way, this shows the need to know the probabilities of the reactions with these nuclei.

Nevertheless, it is very difficult, or even impossible, to directly study stars and the primordial universe. Because of that, researchers use particle accelerators that can simulate this extremes situations. In these accelerators, when a nuclear particle beam, the projectile, interacts with other nuclei, the targets, many processes can occur. One example is elastic scattering. This is the most likely reaction, and it is susceptible to the nuclear potential on the nucleus's surface. Theoretically, nuclear physics commonly uses this type of scattering to test the suitability of the potential. Other examples are the fusion process which depends on the behavior of the imaginary part of the potential near the barrier (in fact, in the internal part of it); the inelastic scattering, where the projectile and target can be excited depending on other quantities like the electric transition probabilities $B(E\lambda)$; the breakup and rearrangement reactions that strongly depend on the structure of the interacting nuclei. These examples of reactions can be used to check the theoretical models of nuclear structure and nuclear reactions upon the convergence of some quantities that must be truncated.

The dynamic of nuclear reactions is very complex, involving many interactions and many degrees of freedom. Because of that, one has to apply some approximations like to use effective interactions to obtain numerical results when allowed by computational limitations. One of these methods is the optical potential calculations that use a complex potential to take into account, effectively, thought polarization potentials, the reactions that are not included explicitly. This method was a significant advance allowing calculating the elastic and reactions cross section for several systems. Another significant step is the coupled channel(CC) method. In this method, it is possible to explicitly consider the excited states of the nuclei in the reactions, allowing the theoretical calculation of the inelastic cross section. However, another critical mechanism in the nuclear reaction is the transfer. To calculate the observables related to these channels, the coupled reaction channel (CRC) method was developed.

Some projectiles have closed structures with low binding energies. They can breakup when they interact with a target. The continuum discretized coupled channel (CDCC) method [18, 19] can be used to describe this type of reactions when the collision of a weakly-bound nucleus populate states in the continuum, as ^{6,8}He [20, 21], ^{6,7,11}Li [6, 22, 23], ^{9}Be [2, 5–7, 24–26], and ^{8}B [27]. The three-body CDCC has been largely used in systems where one nucleus breaks into two fragments [28–38]. However, some of the weakly-bound nuclei shows a Borromean structure composed of three particles where any subsystem of two particles is unbound. In these systems, a four-body treatment needs to be employed.

The four-body CDCC formalism was first developed using pseudo-state methods [39–41]. However, for reactions on heavy targets and at energies around the Coulomb barrier, convergence problems might appear, and a more detailed description of the low continuum spectrum is mandatory. To solve this problem, the four-body CDCC formalism developing the binning procedure for three-body projectiles was presented in Ref. [42]. The binning procedure was developed using the hyperspherical coordinates, making necessary the truncation in the number of hyperspherical momentum K, which determines the maximum relative orbital angular momenta included in the calculation. The convergence with the maximum hypermomentum must be studied since it can generate inaccurate results for some observables.

Although several nuclei have already been studied, those far from the stability line present unknown features from the experimental and theoretical points of view. In this way, the reaction involving neutron-rich nuclei can be fascinating. The light ones can show peculiar structures. This call for a more sophisticated theoretical approach. One example is the ^{6}He, where the four-body CDCC should be used. In other cases, the neutron-rich nuclei present the shell quenching [43], where the ground-state structure is modified, leading to new magic numbers [44].

The present thesis is devoted to the study of the reaction mechanisms involving light neutron-rich projectiles and the static and dynamic effect of its low-binding energy on other reaction mechanisms. Firstly, we are going to study in detail the reaction involving the neutron-rich ^{9}Be projectile colliding with ^{197}Au targets. Although the ^{9}Be nucleus is stable, it is weakly bound, easily breaking in the presence of an external potential. The ^{9}Be can breakup into $n + 2\alpha$ with a separation energy of 1.665 MeV, which is comparable with the energy of the first excited state at 1.68 MeV, or into α+^{5}He with a separation energy of 2.47 MeV. Therefore, in reactions involving this beryllium isotope, the breakup channel must be treated carefully, mainly when one wants to analyze the transfer reactions because the formation of a final nucleus can occur by the stripping process or by the breakup followed by fusion. The breakup might also affect the elastic cross section, most commonly suppressing the rainbow peak [45, 46].

We also perform a systematic study of the fusion in the mid-mass neutron-rich nuclei. We are going to discuss the impact of realistic charge and matter density on the fusion cross section, and the relevance of the coupling with the transfer channel. To this, the theoretical calculations are compared with the experimental data for ^{39,41,45,47}K,^{36,44}Ar+^{16}O and ^{39,41,45,47}K,^{36,44}Ar+^{28}Si systems.

Another objective of this work is to study the ^{6}He+^{208}Pb,^{197}Au reactions by means of four-body CDCC calculations. The ^{6}He projectile is considered a system formed by an inert alpha particle plus two neutrons in this work. As discussed in the sec 6, the ^{6}H projectile has a single bound state with a binding energy of 0.973 MeV, total angular momentum $J^{\pi} = 0^{+}$, and a narrow resonance at 1.792 MeV over the ground state, with a width of 0.113 MeV, and total angular momentum $J^{\pi} = 2^{+}$. The reaction ^{6}He+^{208}Pb has already been studied in the literature, and the four-body CDCC method has shown to be a powerful tool to describe the elastic angular cross sections [42]. Also, the three-body CDCC has been successfully used to describe the ^{6}He as an alpha particle plus a dineutron [47, 48]. Nevertheless, the accuracy of the present calculations to describe other than

elastic scattering quantities has not been tested. This will be done in the present thesis.

For the treatment of the breakup, some methods are developed to discretize the continuum as the bin method [42, 49] or pseudostate (PS) method [40, 41]. The CDCC using the PS method shows good results for treating breakup processes for two-body projectiles. In these cases, the PS method has two advantages: no need for the exact wave function for the projectile and easy calculations of the Gaussian bases [39]. The three-body projectiles using the PS method has been used with a reasonably good description of the elastic scattering data [50,51]. However, some convergence problems arise in reactions involving strong Coulomb interactions [42]. The CDCC using energy-bin technique can be an alternative for these cases.

In the CDCC calculations, the dynamics of the nuclear reactions is described with a significant number of degrees of freedom. Any coupled channel calculation method truncates the model space for numerical reasons, and the consideration of effective potentials is required. In the CDCC calculations, using the energy-bin method, this occurs in the truncation of the maximum hypermomentum and in consideration of potentials that describe the interaction of the projectiles- fragments with the target. For these reasons, comparing the theory with some observables is necessary.

Some of these observables are hard to measure experimentally. One example, is the reaction between ^{9}Be and ^{197}Au when the residual nucleus ^{198}Au is measured. The formation of ^{198}Au can occur through a transfer process or by the breakup of ^{9}Be into two α plus one neutron and then the absorption of the neutron. From the experimental point of view, these two different processes led to the formation of the ^{198}Au. However, these processes are very different. Some theoretical techniques have been developed to overcome this issue, such as the Ishimura-Austern-Vicent (IAV) model [52], based on the spectator model.

How with the availability of different theoretical methods to describe observables and due to the difficulties of measuring these observables, it is interesting to check upon the validity of these models. It is also interesting to determine the accuracy of these models to predict cross sections. In some reactions, including more detailed models shows a better description of the reaction mechanism [48]. Nevertheless, some of these methods can not be implemented in any reaction. The 4-body CDCC is used in the reaction involving a weakly bound nucleus that breaks into three fragments. If more than one fragment has a charge, the solutions of the intrinsic wave functions become more complex, and the discretize bins methods become more difficult to implement. However, the bin methods can better describe the reaction for simpler cases, such as the ^{6}He and ^{11}Li. In the case where more than one fragment has a charge, as in the ^{9}Be case, the transformed harmonic oscillator (THO) method to discretize the continuum can be a good solution to account for the structure of the nucleus.

Chapter 2
Coupled channels and Coupled reaction channels

2.1 Nuclear scattering

When dealing with quantum systems, comparing the theoretical predictions and the real behavior of nature is quite complicated. In quantum theory, not all quantities can be directly measured. One example is wave functions. In general, they are related to the dynamics of the quantum system, yet it is not an observable. In other words, measuring the wave function in nature is impossible. However, other quantities of the states of the quantum systems, such as energy or parity, can be measured.

Even if the quantity is an observable, this does not mean it is easy to measure. So, one question remains: how to measure the observables of a quantum system? The most straightforward answer to this question is with some interactions. In this sense, one of the observables that nuclear physicists are concerned about are the cross sections.

In the simplest way, the cross section is related to the probability that a given particle is detected in relation to other particles. For example, the Rutherford elastic cross section is related to the probability that an atomic nucleus will be deflected to a given angle during a Coulomb interaction with another nucleus. However, a good nuclear scattering theory is necessary to determine the cross section of some processes in a nuclear reaction. This section purports to provide the basis for this scattering theory.

To start describing the nuclear reaction, we want needs to solve the usual task, find eigenstates and eigenvalues of a Hamiltonian. For this purpose, we will look at the time-independent Schrödinger equation with a spherically symmetric and finite potential. The sphericity assumption rises that we expect that the nucleus is spherical. This is not true for a large number of nuclei. However, it is a good first-order approximation. The finitude of the potential is expected for the nuclear potential as a short-range potential. However, the Coulomb potential has a long-range interaction. This implies a specific boundary condition to the wave functions. The Schrödinger equation for this problem can be written as,

$$[\hat{T} + \hat{V} - E]\psi(R, \theta, \phi) = 0, \tag{2.1}$$

where $\hat{T}$ is the kinetic energy operator, E is the energy of the relative motion in the center of mass system, and V is the potential. The kinetic energy operator can be writen in the

spherical polar coordinates, where $z = R\cos\theta$, $x = R\sin\theta\cos\phi$ and $y = R\sin\theta\sin\phi$

$$\begin{aligned}\hat{T} &= -\frac{\hbar^2}{2\mu}\nabla_R^2 \\ &= \frac{\hbar^2}{2\mu}\left[-\frac{1}{R^2}\frac{\partial}{\partial R}\left(R^2\frac{\partial}{\partial R}\right) + \frac{\hat{L}^2}{R^2}\right].\end{aligned} \tag{2.2}$$

$\hat{L}^2$ is the square of the angular momentum operator,

$$\hat{L}^2 = -\hbar^2\left[\frac{1}{\sin^2\theta}\frac{\partial^2}{\partial\phi^2} + \frac{1}{\sin\theta}\frac{\partial}{\partial\theta}\left(\sin\theta\frac{\partial}{\partial\theta}\right)\right]. \tag{2.3}$$

If the beam direction is along the z-axis, the equation does not depend on the ϕ coordinates. That is, the eigensolution of the z components of the angular momentum operator is zero, showing a cylindrical symmetry. Furthermore, as the potential was considered spherical, the Hamiltonian commutes with the momentum vector operator. Thus only the polar (θ) components matters in the wave functions $\psi(R,\theta,\phi) \to \psi(R,\theta)$. Now the problem is,

$$\left[\hat{T} + V - E\right]\psi(R,\theta) = 0. \tag{2.4}$$

The wave function can be expanded using the following linear combinations

$$\psi(\boldsymbol{\kappa},\mathbf{R}) = A\sum_{lm} C_{lm}Y_{lm}(\hat{\mathbf{R}})\frac{u_l(\kappa,R)}{\kappa R}, \tag{2.5}$$

where $u_l(k,R)$ is the modified radial wave function, Y_{lm} is the usual spherical harmonic, and C_{lm} is an appropriate normalization factor. Using these expansion in the eq. 2.4 we have,

$$\begin{aligned}&\left[-\frac{\hbar^2}{2\mu}\nabla_R^2 + V - E\right]A\sum_{lm} C_{lm}Y_{lm}(\hat{\mathbf{R}})\frac{u_l(\kappa,R)}{\kappa R} = 0 \\ &\to \int d\Omega\, Y_{l'm'}(\hat{\mathbf{R}})\sum_{lm} C_{lm}\left[-\frac{\hbar^2}{2\mu}\nabla_R^2 + V - E\right]Y_{lm}(\hat{\mathbf{R}})\frac{u_l(\kappa,R)}{\kappa R} = 0 \\ &\to \left[-\frac{\hbar^2}{2\mu}\left(\frac{d^2}{dR^2} - \frac{l(l+1)}{R^2}\right) + V - E\right]u_l(\kappa,R) = 0\end{aligned} \tag{2.6}$$

This equation corresponds to a one-dimensional Schrödinger equation with a repulsive potential with infinite strength at negative R-values plus the effective L-dependent potential. Also, it is possible to write the wave function in the form:

$$\psi(\boldsymbol{\kappa},\mathbf{R}) = \phi(\boldsymbol{\kappa},\mathbf{R}) + \psi^{\mathrm{sc}}(\boldsymbol{\kappa},\mathbf{R}). \tag{2.7}$$

Using the Ricatti-Bessel function, $\hat{j}_l(kr)$, the first term is the free particle state wave function and can be written as:

$$\phi(\boldsymbol{\kappa},\mathbf{R}) = \frac{1}{(2\pi)^{3/2}}\sum_{lm} 4\pi Y_{lm}^*(\hat{\boldsymbol{\kappa}})Y_{lm}(\hat{\mathbf{R}})i^l\frac{\hat{j}_l(kr)}{kr}. \tag{2.8}$$

And in the limit where $R \to \infty$,

$$\phi(\boldsymbol{\kappa}, \mathbf{R}) \to \frac{1}{(2\pi)^{3/2}} \left[\frac{e^{-ikR}}{R} Z_- + \frac{e^{ikR}}{R} Z_+ \right], \tag{2.9}$$

with

$$\begin{aligned} Z_- &= -\frac{1}{2ik} \sum_{lm} 4\pi Y^*_{lm}(\hat{\boldsymbol{\kappa}}) Y_{lm}(\hat{\mathbf{R}}) i^{2l}, \\ Z_+ &= \frac{1}{2ik} \sum_{lm} 4\pi Y^*_{lm}(\hat{\boldsymbol{\kappa}}) Y_{lm}(\hat{\mathbf{R}}). \end{aligned} \tag{2.10}$$

In the asymptotic limit, the free particle state wave function corresponds to the superposition of an incoming spherical wave with amplitude Z_- and an outgoing spherical wave with amplitude Z_+.

The asymptotic limit of the scattered wave has the form

$$\psi^{\text{sc}}(\boldsymbol{\kappa}, \mathbf{R}) \to \frac{1}{(2\pi)^{3/2}} \left[f(\theta) \frac{e^{ikR}}{R} \right]. \tag{2.11}$$

The scattering wave function in the asymptotic limit, can be written as

$$\psi(\boldsymbol{\kappa}, \mathbf{R}) \to \frac{e^{-ikR}}{R} Z_- + \frac{e^{ikR}}{R} \bar{Z}_+. \tag{2.12}$$

It is important to note that the outgoing amplitude has contribution from the ψ^{sc} and ϕ. However, the ingoing wave has only the contribution from ϕ. Because of that, only the outgoing amplitude should be modified,

$$\begin{aligned} \bar{Z}_+ &= Z_+ + f(\theta) \\ &= f(\theta) + \frac{1}{2ik} \sum_{lm} 4\pi Y^*_{lm}(\hat{\boldsymbol{\kappa}}) Y_{lm}(\hat{\mathbf{R}}). \end{aligned} \tag{2.13}$$

Also is possible to write the scattering amplitude in terms of the S-matrix,

$$\bar{Z}_+ = \frac{1}{2ik} \sum_{lm} 4\pi Y^*_{lm}(\hat{\boldsymbol{\kappa}}) Y_{lm}(\hat{\mathbf{R}}) S_l. \tag{2.14}$$

Setting the two forms of the scattering amplitude we get:

$$f(\theta) = \frac{1}{2ik} \sum_{lm} 4\pi Y^*_{lm}(\hat{\boldsymbol{\kappa}}) Y_{lm}(\hat{\mathbf{R}}) \left(S_l - 1 \right). \tag{2.15}$$

It is known the following property:

$$P_l(\cos\theta) = \frac{4\pi}{2l+1} \sum_{m} Y^*_{lm}(\hat{\boldsymbol{\kappa}}) Y_{lm}(\hat{\mathbf{R}}). \tag{2.16}$$

That is true if θ is defined as $\theta = cos^{-1}(\hat{\boldsymbol{\kappa}} \cdot \hat{\mathbf{R}})$. So, eq. 2.15 can be written as

$$f\left(\theta\right) = \frac{1}{2ik} \sum_{l} (2l+1) P_l(\cos\theta) \left(\mathbf{S}_l - 1 \right). \tag{2.17}$$

With the scattering amplitude we can find the elastic differential cross section,

$$\sigma(\theta) = \frac{\mathrm{d}\sigma}{\mathrm{d}\Omega} = \left| \frac{1}{2ik} \sum_l (2l+1) P_l(\cos\theta) \left(\mathbf{S}_l - 1\right) \right|^2 . \tag{2.18}$$

It is important to remember that to calculate the scattering amplitude, we purposely hide some indices. This index and quantum number are related to the angular momentum and projection of the angular momentum. We must sum over all the indices to find the elastic differential cross section. The cross section will be discussed for others reactions, such as transfer and fusion, in the following sections.

2.2 The S-Matrix

One important ingredient of scattering is the reflection coefficient. The S-matrix is a matrix related to the reflection coefficient between the initial and final state. It is possible to describe the S-matrix elements by the phase shift of the outgoing wave with the respect of the incoming wave due the effect of the potential, δ_L,

$$\mathbf{S}_L = e^{2i\delta_L}. \tag{2.19}$$

It is important to note that the $|\mathbf{S}_L|^2$ is the survival probability. If the potential is real, $|\mathbf{S}_L|^2 = 1$, and the phase shift is real. If the potential is complex, $|\mathbf{S}_L|^2 < 1$, and the phase shift is complex. Also, the phase shift can give us information about the potential. When the real part of the phase shift is positive, the potential is attractive, when negative, the potential is repulsive, and, for the phase shift equals zero, there is no potential.

Furthermore, one can write the δ_L as a sum of a Coulomb,$\sigma_L(\eta)$, and a Coulomb-distorted nuclear phase shift, δ_L^n. The S-matrix can be written as:

$$\mathbf{S}_L = e^{2i\sigma_L(\eta)} \mathbf{S}_L^N. \tag{2.20}$$

Using the follow relation one can rewrite the scattering amplitude,

$$\begin{aligned}
& e^{2i\delta_L} - 1 = \left(e^{2i\sigma_L(\eta)} - 1\right) + e^{2i\sigma_L(\eta)} \left(e^{2i\delta_L^n} - 1\right), \\
& \rightarrow f(\theta) = f_C(\theta) + f_n(\theta), \\
& \rightarrow f_C(\theta) = \frac{1}{2ik} \sum_L (2L+1) P_L(\cos\theta) \left(e^{2i\sigma_L(\eta)} - 1\right), \\
& \rightarrow f_n(\theta) = \frac{1}{2ik} \sum_L (2L+1) P_L(\cos\theta) e^{2i\sigma_L(\eta)} \left(\mathbf{S}_L^n - 1\right).
\end{aligned} \tag{2.21}$$

In this way, the cross section is,

$$\sigma(\theta) = |f(\theta)|^2 = |f_C(\theta) + f_n(\theta)|^2 \tag{2.22}$$

The contribution of the Coulomb scattering diverges for small angles, since

$$\sigma_{\mathrm{Ruth}}(\theta) = \frac{\eta^2}{4k^2 \sin\left(\theta/2\right)}, \tag{2.23}$$

it is commom define a observable that becomes unity at small angles:

$$\sigma(\theta)/\sigma_{\text{Ruth}}(\theta) = \frac{|f_C(\theta) + f_n(\theta)|^2}{|f_C(\theta)|^2} \tag{2.24}$$

This observable is one for small angles, because the particles scattered in this angle did not pass close to the nucleus and not suffer the action of the nuclear potential.

2.3 Optical Potential formalism

Although elastic scattering is expected to be the most important reaction in nuclear interaction, others channels can be relevant in some cases. Even when ones to estimate only the elastic cross section, the coupling with these other reaction channels can drastically change it. A large number of reactions: inelastic, fusion, transfer, and others, are difficult to take into account either by computational problems or lack of satisfactory theoretical models. These mechanisms created a headache for the nuclear physicist trying to describe the dynamics of nuclear scattering.

Consider a nuclear potential $U(\mathbf{r})$ describing the interaction between the projectile and the target. When these projectiles interact with the target, many channels can be accessed. If the model wave function considers the expansion in some of the basis states of the intrinsic Hamiltonian, an effective potential that considers the truncated channels is mandatory. In this way comes the analogy with refraction, when the waves pass from one medium to another. When refraction is treated realistically, the refraction index for this interaction treated with an effective potential $U(\mathbf{r})$ has to be a complex number. The real part of the index describes how the light is transmitted and the imaginary how it is absorbed by the medium. In this sense, the effective optical potential has to be complex. The real part of the potential deals with the scattering of the projectile. The second one is related with the absorption of flux.

The optical formalism can simplify the large number of reaction using a complex potential in the form:

$$U(\mathbf{r}) = V(\mathbf{r}) - iW(\mathbf{r}), \tag{2.25}$$

The $V(\mathbf{r})$ is the real part of the potential and $W(\mathbf{r})$ the imaginary part. In this way, the Hamiltonian is not Hermitian, that is, if the $W(\mathbf{r}) < 0$ that the potential absorbs flux. Inserting this potential in the Schrödinger equation, one can derive the continuity equation:

$$\nabla \cdot \mathbf{j} + \frac{\partial}{\partial t}\psi^*\psi = -\frac{2}{\hbar}W\psi^*\psi. \tag{2.26}$$

Above, $\mathbf{j}$ is the probability flux, and ψ is the wave function. Also, it is possible to see explicitly that $W(\mathbf{r}) < 0$ is taking away particles. Assuming that $|\psi|^2$ is constant in time, the number of absorbed particles can be calculated as:

$$N_a = \frac{2}{\hbar}\int W(\mathbf{r})|\psi(\mathbf{r})|^2\, d^3r = \frac{2}{\hbar}\langle\psi|\, W\, |\psi\rangle\,. \tag{2.27}$$

We can calculate the absorption cross section by dividing the number of absorbed particles by the incident flux,

$$\sigma_a = \frac{2}{\hbar\nu} \langle\psi| W |\psi\rangle , \tag{2.28}$$

where, $2/\hbar\nu = k/E$. This shows that this method has a good theoretical ground, although it is essential to remind that the optical model is concerned with effective interaction. In some cases only the elastic scattering is retained and effectively all the other channels is accounted by the optical potential. This one-channel calculation is usually recognized as optical model approach. When the inelastic channels are included, it is called the generalized optical model, and it is used in the Coupled channels calculations. Nevertheless, the nuclear potential's final form is unknown, so one must consider effective potentials to describe the reactions dynamics.

The Woods-Saxon form for the nuclear potential has been largely used in the literature for the real and imaginary parts. For the imaginary part, it is common to use a surface potential (the derivative of the Woods-Saxon potential) to consider direct reactions because they are concentrated at the surface. The Woods-Saxon potential can be written as:

$$V(r) = \frac{V_0}{1 + e^{r-R}/a}, \tag{2.29}$$

where V_0, R, and a stand for the depth, radius, and diffuseness of the potential, respectively. $R = r_0(A_p^{1/3} + A_t^{1/3})$, with r_0 is the reduced radius, and A_p and A_t are the mass number of the projectile and target. Although widely used in the literature, the Woods-Saxon potential has some ambiguities due to the six free parameters (three in either real and imaginary part of the potential) that must be adjusted to describe the cross section. A few attempts to relate its parameters to more fundamental quantities have been done. For protons and neutrons scattering on ions, Koning *et al.* [53] have proposed a global parametrization with a smooth dependence on energy of the depth and on the mass number for the geometrical parameters. Others models attempt to describe the energy dependence of the ion-ion potentials, and the São Paulo potential is one of them [54].

2.3.1 Folding potentials

One way to consider the microscopic structure of each nucleus is through a potential that considers the interaction between two nucleons of each nucleus. This can be realized if the interaction between the nucleons is known. If one of the interacting nuclei is considered structureless (considering it as a close core, this is a good approximation for a double-magic nucleus), this potential is known as the *single-folding* potential. If the structure of both nuclei is considered, the potential is called *double-folding*.

The idea of the double-folding potentials is based on the reaction between two nuclei at sufficiently high energies. In this high-energy regime, the nucleons are expected to act almost like they were free particles. So the interaction between the nucleus can be reduced to the free nucleon-nucleon interaction. In this arrangement, the real part of the optical potential to describe this reaction is approximately the averaged interaction, V_{nn}^{ij},

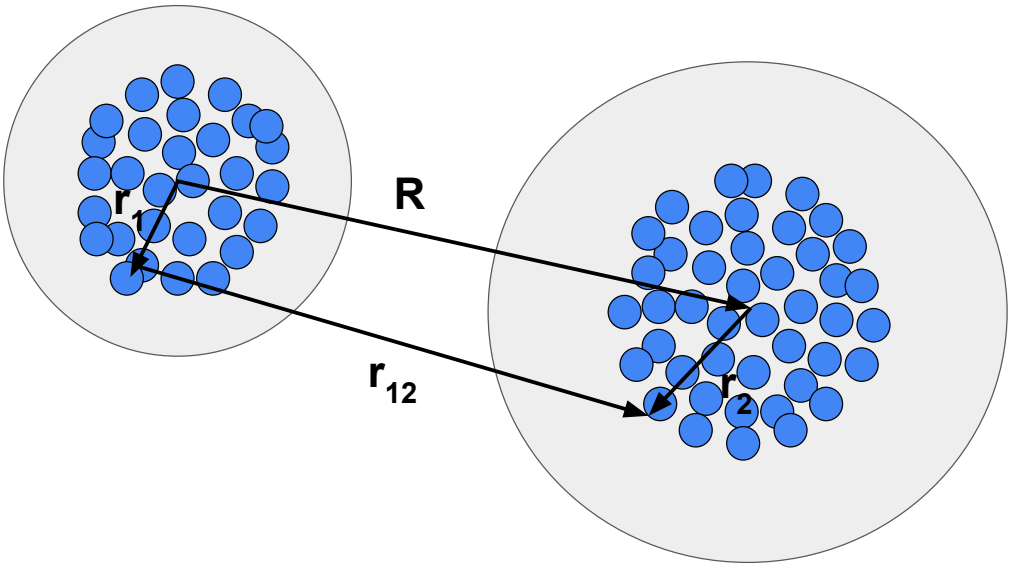

Figure 2.1: Representation of the nucleon-nucleon interaction between two nuclei.

over the distribution of nucleons in the two colliding nuclei:

$$V = \left\langle \psi \left| \sum_{ij} V_{nn}^{ij} \right| \psi \right\rangle , \tag{2.30}$$

where i and j are the label of each nucleon in the target and projectile, respectively. At low energies it is expected that the behavior of this interaction do not change drastically. Thus, it is expected that this form is a good approximation. In the local approximation the interaction can be writen as $V_{nn}^{ij} \rightarrow V_{nn}(r_{ij})$, this becomes

$$V(\mathbf{R}) = \int \int \rho_1(\mathbf{r_1})\rho_2(\mathbf{r_2}) V_{nn}(|\mathbf{R} - \mathbf{r_1} + \mathbf{r_2}|)\, d\mathbf{r_1}\, d\mathbf{r_2} \tag{2.31}$$

where $\rho_1(\mathbf{r_1})$ and $\rho_2(\mathbf{r_2})$ are the ground state density distribution of each nucleus. $\mathbf{r}_{12}$ is the relative distance vector between the two interacting nucleons. $\mathbf{R}$ is the distance between the center of mass of the two interact nuclei (see Fig. 2.1). Because the integration rounds on two variables, this potential is called double-folding potential. When the nucleus 1 is a single nucleon or is treated as a inert core, $\rho_1(\mathbf{r}_1) = \delta(\mathbf{r}_1)$, the potential is called single-folding and can be write as

$$V(\mathbf{R}) = \int \rho_2(\mathbf{r_2}) V_{nn}(|\mathbf{R} + \mathbf{r_2}|)\, d\mathbf{r_2}. \tag{2.32}$$

In the momentum space, the double-folding is a product of three Fourier transform, while the single-folding is a product of two. Depending on the chosen interaction, an analytic form can be found for this potentials. The complexity of the folding potential's final form depends on the density and the nucleon-nucleon interaction used.

2.3.2 São Paulo Potential

The São Paulo potential (SPP) is an effective *double-folded* potential that considers the Pauli nonlocality [54]. This potential was idealized firstly to describe the elastic

scattering of α-particles projectiles by several targets in a wide energies range. Later it was extend for heavier projectile. This potential has been widely used to describe heavy ion scattering, as it can be employed with a systematic that eliminates ambiguities [55].

The first step in conceiving this potential is to describe the nuclear densities. In the SPP systematic, the two-parameter Fermi(2pF) distribution is used to describe the density of protons, neutrons, nucleons, charge, and matter. The systematic parameters of 2pF distribution extracted from electron scattering experiments and Dirac-Hartree-Bogoliubov microscopic calculations shows a good result when used for the charge and matter densities, and has the form

$$\rho(r) = \frac{\rho_0}{1 + e^{\frac{r-R_0}{a}}}. \tag{2.33}$$

The ρ_0, a, and R_0 parameters can be found by the normalization condition

$$4\pi \int_0^\infty \rho(r) r^2 dr = X, \tag{2.34}$$

where X is the number of protons, neutrons, or nucleons. The systematic of the 2pF for matter and charge densities results in a good description of the densities when the nucleus is close to the stability line. However, it has been shown recently that the matter densities of neutron-rich nuclei (far from the stability line) do not follow SPP systematic. For these nuclei, Dirac-Hartree-Bogoliubov has been recently reported [56].

The main ingredient of this potential is the effective nucleon-nucleon interaction $V_{nn}(r_{12})$. In the SPP, the interaction is consistent with the Pauli nonlocality. The non-locality is implicity taken into account by some energy dependency, consistent with the dispersion relation, therefore $V_{nn}(r_{12}) \to V_{\rm LE}(r_{12}, E)$ (the LE comes from local-equivalent). It is expected that the effect of the Pauli nonlocality to be negligible for energies close to the barrier and vary smooth with the energy. In this way, a good approximation is

$$V_{\rm LE}(r, E) \approx V_{nn}(r) e^{-4\nu^2/c^2}, \tag{2.35}$$

where ν is the projectile's velocity and c is the light's speed. Moreover, the $V_{nn}(R)$ is some nucleon-nucleon interaction that not depends on energy. It is easy to see that the local equivalent interaction, eq. 2.35, smoothly depends on energy, and for energies close to the barrier, ν^2/c^2 tends to zero. Finally, the nucleon-nucleon interaction was found with a folding-type

$$V_{NN}(r) = \frac{2\pi V_0}{r} \int_0^\infty r_1 \rho_n(r_1) \left(\int_{|r-r_1|}^{r+r_1} r_2 \rho_n(r_2)\, dr_2 \right) dr_1. \tag{2.36}$$

The $V_0 = -456$Mev fm^3 and the $\rho_n(r)$ has the form

$$\rho_n(r) = \rho_0 e^{r/a_n}, \tag{2.37}$$

where ρ_0 and a_n are found by the same way than Eq. 2.34. The integration has analytical form,

$$V_{NN}(r) = \frac{V_0}{64\pi a_n^3} e^{-r/a_n} \left(1 + \frac{r}{a_n} + \frac{r^2}{3a_n^2} \right). \tag{2.38}$$

The *double-folding* São Paulo Potential (SPP) was used in most of this work. The real part of the potential can be found by the follow equation:

$$V(\mathbf{R}, E) = \int \rho_1(\mathbf{r_1})\rho_2(\mathbf{r_2})V_{nn}(v, |\mathbf{R} - \mathbf{r_1} + \mathbf{r_2}|)\; d\mathbf{r_1}\; d\mathbf{r_2}. \tag{2.39}$$

The $\rho_1(\mathbf{r_1})$ and $\rho_2(\mathbf{r_2})$ are the two-parameter Fermi distributions, $\frac{\rho_0}{1+\exp\left(\frac{r-R_0}{a}\right)}$, that describe the nucleon densities. The $V_{nn}(v, \mathbf{R} - \mathbf{r_1} + \mathbf{r_2})$ is the effective nucleon-nucleon interaction, that depends of the velocity, v and can be written as:

$$V_{nn}(v, r_{12}) = \frac{2\pi V_0}{r_{12}} e^{-4v^2/c^2} \int_0^\infty r'_1 \rho_m(r'_1) \int_{|r_{12}-r'_1|}^{r_{12}+r'_1} r'_2 \rho_m(r'_2)\; dr'_2\; dr'_1. \tag{2.40}$$

The matter density, ρ_m, in the SPP is taken as a Dirac's delta shape.

The SPP has been very often used to describe reactions involving heavy ions. In studying the energy dependence of the optical potential one-channel calculations are usually used, assuming that the imaginary part of the optical potential has the same form factor as the real part. Two strength coefficients are used in this one-channel calculation to describe the elastic scattering cross sections. The main objective is to study the energy dependence of the optical potential. In this way, the breakup threshold anomaly, instead of the usual threshold anomaly observed in reactions induced by tightly bound nuclei [57], was obtained in reactions induced by weakly-bound nuclei [58]. Also, the SPP is commonly used in the CC calculations when other reaction channels are included in the coupling scheme. If the relevant couplings to the elastic channel are included in the coupling scheme, the strength factor of the real part is $N_r = 1.0$. Also, a short range (acting inside the Coulomb barrier) imaginary potential to account for absorption to fusion is considered (W_0= 50 MeV $r_w = 1.06$ fm $a_w = 0.2$ fm). When only couplings with the most important channels are considered, the imaginary part is multiplied by $N_i = 0.60$ [59].

2.4 Transition probabilities

In inelastic reactions, the nucleus changes the internal energy, going from the initial state, with ε_i, to a final state, ε_f. Besides energy, usually, the final state's spin, I_f, is different from the initial, I_i. This implies that some angular momentum is transferred. This is given by the multipolarity of the reaction, λ, respecting the relationship:

$$|I_i - I_f| \leq \lambda \leq I_i + I_f. \tag{2.41}$$

In the energy regime discussed in this work, only odd multipoles can change the nuclear parity of the transitions, and the magnetic transitions are weaker than the electric. In these processes dominated by the Coulomb forces as the inelastic transitions, the electric transitions are stronger than magnetic. These electric transitions between the initial and final state can be written as:

$$B(E\lambda, I_i \to I_f) = \left|\langle I_f \| \hat{E} \| I_i \rangle\right|^2 \left(\frac{2\lambda + 1}{4\pi}\right) \tag{2.42}$$

The electric multipole operator for a three-body system assume the form:

$$\hat{E}_{\lambda\mu}(\mathbf{x}_k, \mathbf{y}_k) = \sqrt{\frac{4\pi}{2\lambda+1}} \sum_{q=1}^{3} Z_q e r_q^{\lambda} Y_{\lambda\mu}(\hat{r}_q). \tag{2.43}$$

It is possible to calculate the reduced transition probabilities, $B\left(I_a \rightarrow I_b,\ \lambda\right)$, by the form:

$$B\left(I_i \rightarrow I_f,\ \lambda\right) = \frac{2I_f+1}{2I_i+1} B(E\lambda). \tag{2.44}$$

Also, when the rotational model is used to calculate the transition between the initial and the final states, the reduced intrinsic matrix element within the rotational model, $M(E\lambda)$, is used. The $M(E\lambda)$ are given

$$M(E\lambda) = \sqrt{(2I_i+1)B\left(I_i \rightarrow I_f,\ \lambda\right)}. \tag{2.45}$$

Other important quantities are the deformation parameter, β_λ, and the deformation length in the rotational model, $DEF(\lambda)$. They can be calculated as,

$$\begin{aligned} \beta_\lambda &= \frac{4\pi}{3} \frac{Mn(E\lambda)}{Z\left(r_0 A^{1/3}\right)^{\lambda}}, \\ DEF(\lambda) &= \beta_\lambda \left(r_0 A^{1/3}\right), \end{aligned} \tag{2.46}$$

where matrix elements are

$$Mn(E\lambda) = \frac{\sqrt{B\left(I_i \rightarrow I_f,\ \lambda\right)}}{\langle I_i\ k\ \ \lambda\ 0 | I_f\ k\rangle} (-1)^{\left(I_f - I_i - |I_i - I_f|\right)/2}. \tag{2.47}$$

When electric transitions are considered, it is important to pay attention to the units. The units frequently used in the literature are the Weisskopf single particle units and the $e^2 b^\lambda$ units. They are related as,

$$B(E\lambda)_{e^2 b^\lambda} = \frac{(1.2)^{2\lambda}}{4\pi} \left(\frac{3}{\lambda+3}\right)^2 A^{2/3\lambda} B(E\lambda)_{W.u.}. \tag{2.48}$$

2.5 Coupled Channel and Coupled Reaction Channels

The coupled channel (CC) method is important for describing nuclear reactions involving low-energy ions. To describe the nuclear system using the CC method, we must solve a large number of coupled equations. These coupled equations are related to the number of eigenstates of the system. The number of eigenstates for a reaction is infinite. Because of that, it is impossible to account for all of them. For this reason, the total wave function must be truncated, retaining the most relevant states. With these selected states, it is possible to construct a model Hamiltonian for the nuclear reaction.

When only the elastic and inelastic channels are retained, the method is called CC. However, in many systems, others non-elastic channels are very important too, like the

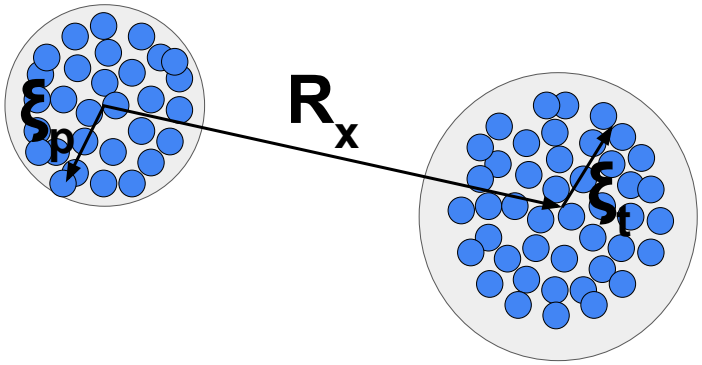

Figure 2.2: Representation of the coordinates of a nuclear reaction.

rearrangement reactions. The method is called coupled reaction channel (CRC) when it is possible to consider the transfer channels. Another essential type of reaction occurs when the projectile breaks. The Continuum discretized coupled channel was developed to handle these situations. In this section, we will discuss the CC and CRC method.

The first step is to write the wave function for the partition x,

$$\begin{aligned}\Psi^M_{xJ}(\mathbf{R}_x,\xi_p,\xi_t) = &\sum_{\substack{LI_pJ_pI_t\\M'\mu_pM_p\mu_t}} \phi^{x\ p}_{I_p\mu_p}(\xi_p)\phi^{x\ t}_{I_t\mu_t}(\xi_t) i^L Y^M_L(\mathbf{R}_x)\frac{1}{R_x}\psi^J_\alpha(R_x)\\ &\times (L\ M'\ \ I_p\ \mu_p|J_p\ M_p)\,(J_p\ M_p\ \ I_t\ \mu_t|J\ M)\,,\\ =&\sum_\alpha |\alpha\rangle\,\frac{\psi^J_\alpha(R_x)}{R_x}.\end{aligned} \tag{2.49}$$

The internal wave function of the projectile and target in channel α, are $\phi^{x\ p}_{I_p\mu_p}(\xi_p)$ and $\phi^{x\ t}_{I_t\mu_t}(\xi_t)$, respectively. The radial and intrinsic coordinates' representation can be seen in Fig. 2.2. α is not a quantum number but a set of them to represent the channel. The Schrödinger wave function for a reaction with total energy E and a Hamiltonian operator H

$$[H-E]\,\Psi^M_{xJ}=0. \tag{2.50}$$

The Hamiltonian can be written in terms of the intrinsic Hamiltonians of the projectile and target, kinetic energies, and a potential term:

$$H = H_{xp}(\xi_p) + H_{xt}(\xi_t) + T_x(R_x) + V_x(R_x,\xi_p,\xi_t). \tag{2.51}$$

The coupled equations can be found if we insert the eq. 2.49 in eq. 2.50 and multiply by the left $R_{x'}\,\langle\alpha'|$:

$$\begin{aligned}R_{x'}\,\langle\alpha'|\sum_\alpha [H-E]\,|\alpha\rangle\,\frac{\psi_\alpha(R_x)}{R_x}=0,\\ \sum_\alpha R_{x'}\,\langle\alpha'|\,H-E\,|\alpha\rangle\,\frac{\psi_\alpha(R_x)}{R_x}=0.\end{aligned} \tag{2.52}$$

This give a set of equations for each α' considered, the set of coupled channel equations. The matrix elements can be written as

$$\begin{aligned}\langle\alpha'|\, H - E\,|\alpha\rangle &= \langle\alpha'|\, H_{xp} + H_{xt} + T_x + V_x - E\,|\alpha\rangle \\ &= \langle\alpha'|\, \varepsilon_{xp} + \varepsilon_{xt} + T_{xL} + V_x - E\,|\alpha\rangle \\ &= \langle\alpha'|\, T_{xL} + V_x - E_\alpha\,|\alpha\rangle \\ &= \langle\alpha'|\, T_{x'L} + V_{x'} - E_{\alpha'}\,|\alpha\rangle\end{aligned} \tag{2.53}$$

This show that has two way to write the matrix elements, the prior, $\langle\alpha'|\, T_x + V_x - E_\alpha\,|\alpha\rangle$, and the post, $\langle\alpha'|\, T_{x'} + V_{x'} - E_{\alpha'}\,|\alpha\rangle$. Both representations give the same result when considering all terms of the coupled equations. Manipulating the radial term, we can get

$$\begin{aligned}R_{x'}\,\langle\alpha'|\, H - E\,|\alpha\rangle\,\frac{1}{R_x} &= R_{x'}\,\langle\alpha'|\, T_x + V_x - E_\alpha\,|\alpha\rangle\,\frac{1}{R_x}, \\ &= R_{x'}\,\langle\alpha'|\alpha\rangle\,\frac{1}{R_x}\,[T_{xL} - E_\alpha] + R_{x'}\,\langle\alpha'|\, V_x\,|\alpha\rangle\,\frac{1}{R_x}, \\ &= N_{\alpha\alpha'}\,[T_{xL}(R_x) - E_\alpha] + V^{\text{prior}}_{\alpha'\alpha},\end{aligned} \tag{2.54}$$

where T_{xL} is the radial kinetic energy operator plus the eigenvalues of the angular parts. Using the above manipulations, one can write the following coupled equation.

$$[T_{xL}(R_x) - E_\alpha]\,\psi_\alpha(R_x) + \sum_{\alpha'} V^{\text{prior}}_{\alpha\alpha'}\psi_{\alpha'}(R_{x'}) + \sum_{\alpha', x\neq x'} N_{\alpha\alpha'}\,[T_{x'L'} - E'_\alpha]\,\psi_{\alpha'}(R_{x'}) = 0. \tag{2.55}$$

The method is called Coupled Channel (CC) when the other reaction occurs inside of the same partition. Because of that, the non-orthogonality term vanishes, and we can rewrite it in the form:

$$\left[E_\alpha - T_{xL}(R_x) - V^{\text{prior}}_{\alpha\alpha}\right]\psi_\alpha(R_x) = \sum_{\alpha'\neq\alpha} V^{\text{prior}}_{\alpha\alpha'}\psi_{\alpha'}(R_x). \tag{2.56}$$

On the other hand, the coupled reaction channel system is obtained when nuclei can exchange nucleons or clusters, and different partitions become available. For convenience, we will call the set of quantum numbers of the final partition β (supposing that only two partitions are available). So, one can write in the prior representation

$$\begin{aligned}&\left[E_\alpha - T_{xL}(R_x) - V^{\text{prior}}_{\alpha\alpha}\right]\psi_\alpha(R_x) - \sum_{\alpha'\neq\alpha} V^{\text{prior}}_{\alpha\alpha'}\psi_{\alpha'}(R_x) \\ &\qquad = \sum_\beta \left(V^{\text{prior}}_{\alpha\beta} + N_{\alpha\beta}\,[T_{x'L'} - E_\beta]\right)\psi_\beta(R_{x'}),\end{aligned} \tag{2.57}$$

and in the post representation:

$$\begin{aligned}&\left[E_\beta - T_{x'L'}(R_{x'}) - V^{\text{post}}_{\beta\beta}\right]\psi_\beta(R_{x'}) - \sum_{\beta'\neq\beta} V^{\text{post}}_{\beta\beta'}\psi_{\beta'}(R_{x'}) \\ &\qquad = \sum_\alpha \left(V^{\text{post}}_{\beta\alpha} + [T_{xL} - E_\alpha]\,N_{\beta\alpha}\right)\psi_\alpha(R_x).\end{aligned} \tag{2.58}$$

The equations 2.57 and 2.58 form the set of coupled channels calling the coupled reaction channel (CRC) method. An important element in the transfer reactions is the non-orthogonality therm, that is, the overlap

$$N_{\beta\alpha} = \int d\xi' \phi_\beta(\xi', \mathbf{r}')\phi_\alpha(\xi') \equiv \langle \phi_\beta | \phi_\alpha \rangle \tag{2.59}$$

remember that the wave functions of different partitions are not orthogonal. Using the parentage decomposition, it can be written as

$$\langle \phi_\beta | \phi_\alpha \rangle = \mathcal{A}^{l\,j}_{\beta\alpha} \psi^{l\,j}_{\beta\alpha}(\mathbf{r}'), \tag{2.60}$$

where, $\mathcal{A}^{l\,j}_{\beta\alpha}$ are the spectroscopic amplitudes or $S^{l\,j}_{\beta\alpha} = |\mathcal{A}^{l\,j}_{\beta\alpha}|^2$ is the spectroscopic factors, and $\psi^{l\,j}_{\beta\alpha}(\mathbf{r}')$ are the single-particle wave functions describing the motion particle relative to the cores. The spectroscopic factor is the weight of the single particle wave function when it is described as $\alpha + b$ (where b is the transferred particle).

The coupled channels and coupled reaction channels method has been widely applied for a large range of reactions, from $n + \alpha$ scattering [60] up to reactions involving different projectiles and targets in a wide energy range.

2.6 Fusion Cross Section

In sec. 2.5, we handled nuclear reactions expanding the wave function in a set of intrinsic states of the system. However, the fusion process can not be handled this way because the formation and decay of the compound nucleus are very complex, involving many multi-step reactions until statistical equilibrium is reached in a very highly excited state. When weakly-bound nuclei are involved, specific fusion reaction mechanisms can occur [46].

The fusion reaction is a very important process. As it is impossible to include many steps in the interactions in CC calculations to reach the final fusion channel of the fused system, one recalls some approximations to derive the fusion cross section. The most commonly used is to introduce a short-range imaginary part into the interaction potential to warrant that all the flux inside the Coulomb barrier is absorbed.

The fusion cross section can be obtained from one-channel calculation. Using a short-range imaginary potential, we will obtain an absorption cross section that coincides, in this case, with the reaction and fusion cross section. This situation is depicted in Fig. 2.3. Nevertheless, this situation is not correct from the physical point of view, as the absorption is simulated to occur exclusively from the elastic channel. In fact, if other direct reaction channels are possible, they can also feedback on the fusion process.

As stated in previous chapters, the potential U is complex, where the imaginary part is an effective interaction that considers the channels that are not explicitly treated in the CC. In this way, the fusion cross section is calculated very similarly to the absorptive

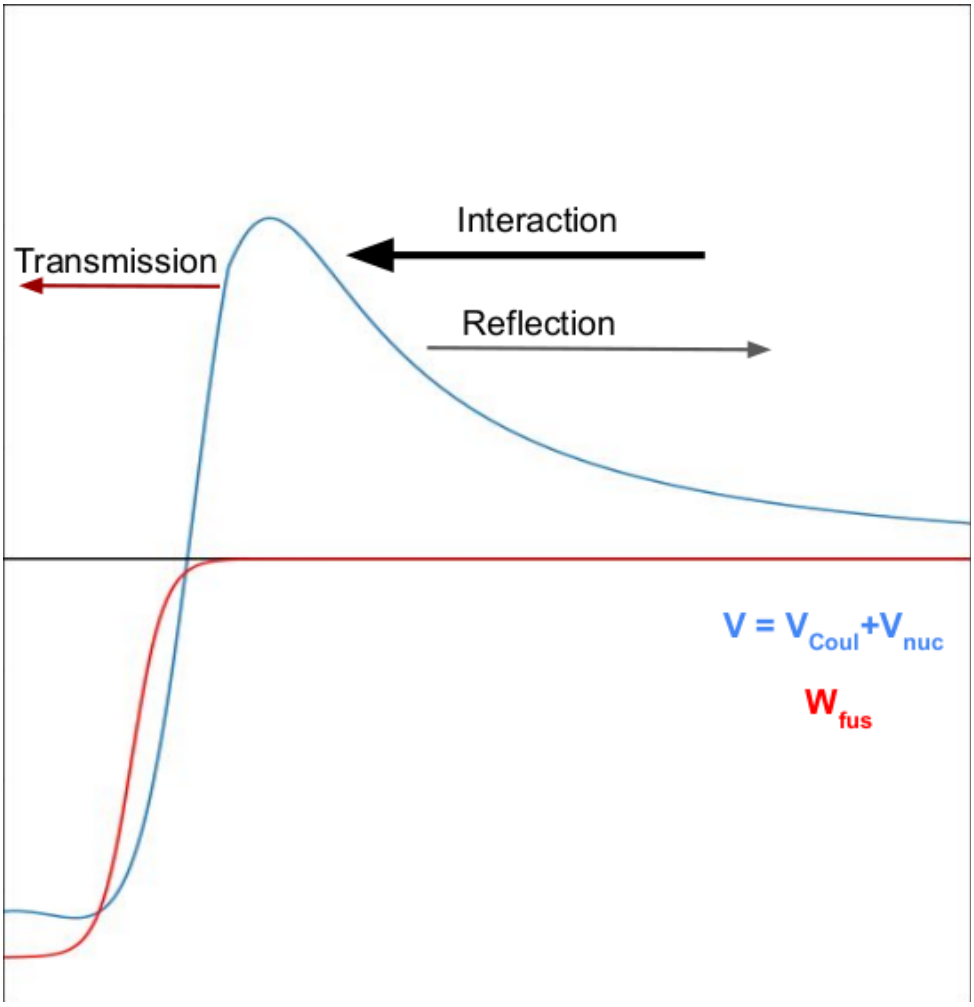

Figure 2.3: Scheme showing the expected behavior of the real and imaginary parts of the potential for the fusion. The blue and red curves are the real and imaginary potential, respectively. The arrows show the flux of the reaction.

cross section eq. 2.28, taking the form:

$$\sigma_{\mathrm{F}} = \frac{1}{|A|^2}\frac{k}{E}\sum_{\alpha\alpha'}\langle\alpha|\, W_{\mathrm{Fus}}\,|\alpha'\rangle\,, \tag{2.61}$$

where W_{Fus} is the part of the optical potential that accounts for fusion. Furthermore, there is an alternative form to calculate the fusion cross section,

$$\sigma_{\mathrm{F}} = \frac{\pi}{k^2}\sum_{l=0}(2l+1)P_l^F(E). \tag{2.62}$$

The $P_l^F(E)$ are the fusion transmission coefficients through the coulomb barrier. In Ref. [61] more details about the determination of these transmission coefficients can be found. These details are out of the scope of this work.

It was believed that the wave functions used to obtain the fusion cross section are calculated using the optical method [57]. In this sense, this means that the imaginary

part of the potential, W, go until the surface of the nuclear interaction, taking flux of the inelastic channels. And then, the fusion cross section is calculated by the eq. 2.61 with the short-range potential, $W_{\rm Fus}$, that accounts only for the fusion. However, new pieces of evidence show that this is not correct. As can be seen from Fig. 2.4, the red dashed line, is the cross section, $\sigma_{\rm F}^{\rm Opt}$, calculated with wave functions generated using the optical potential and then calculated with the internal potential. The internal potential (short-range) and the total optical potential (long-range) are illustrated in Fig. 2.5.

On the other hand, the black soline line in Fig. 2.4, show a fusion cross section $\sigma_{\rm F}^{\rm Int}$ where the wave functions are generated using only the short-range potential. Showing that when the optical potential is used part of the flux that should go to fusion vanish.

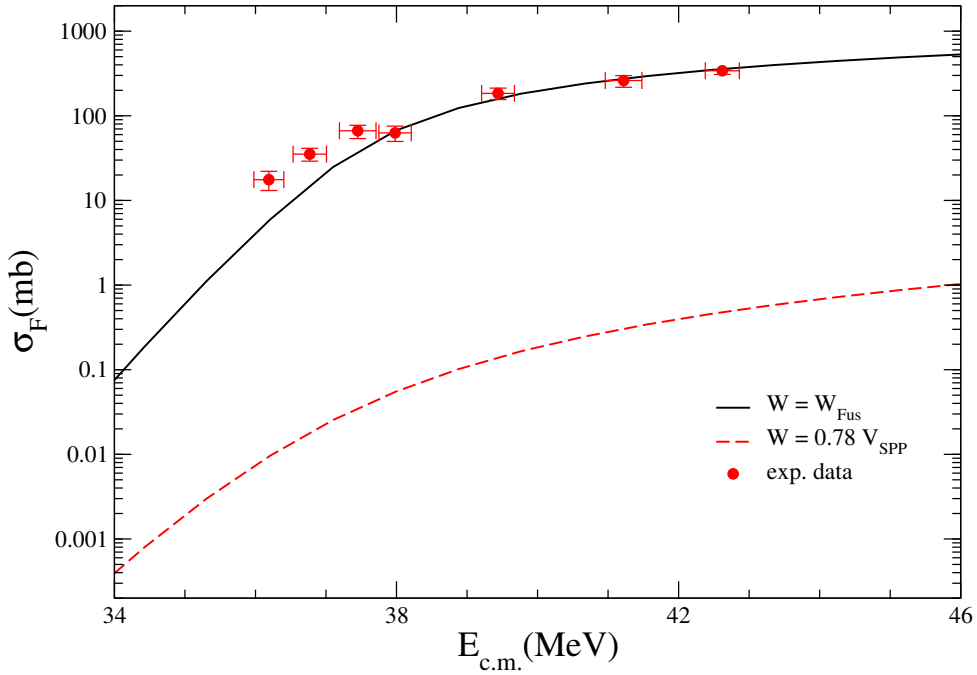

Figure 2.4: Comparison between the fusion cross section obtained using wave functions calculated with a long-range potential (SPP) and a short-range potential(W_{fus}) in the ^{47}K+^{28}Si system. The experimental cross section was taken from Ref. [1].

The suppression of the fusion cross section, when a long-range potential is used to generate the wave functions, is induced by not absorbing back flux from reactions that occur on the surface of the nucleus.mudar aquiThen if the short-range potential is used to derive the fusion cross section, one will absorb flux to fusion from the elastic scattering only. The absorption from nonelastic channels simulated by the long-range imaginary potential is disregarded in this case.

2.6.1 Fusion functions and the Universal Fusion Function

Comparing the experimental fusion data for the different systems might be interesting in some situations involving weakly bound projectiles. One way to do that is to measure the fusion using the same target. However, this is only possible sometimes. Another way is to make a normalization by removing the dependence on the size and

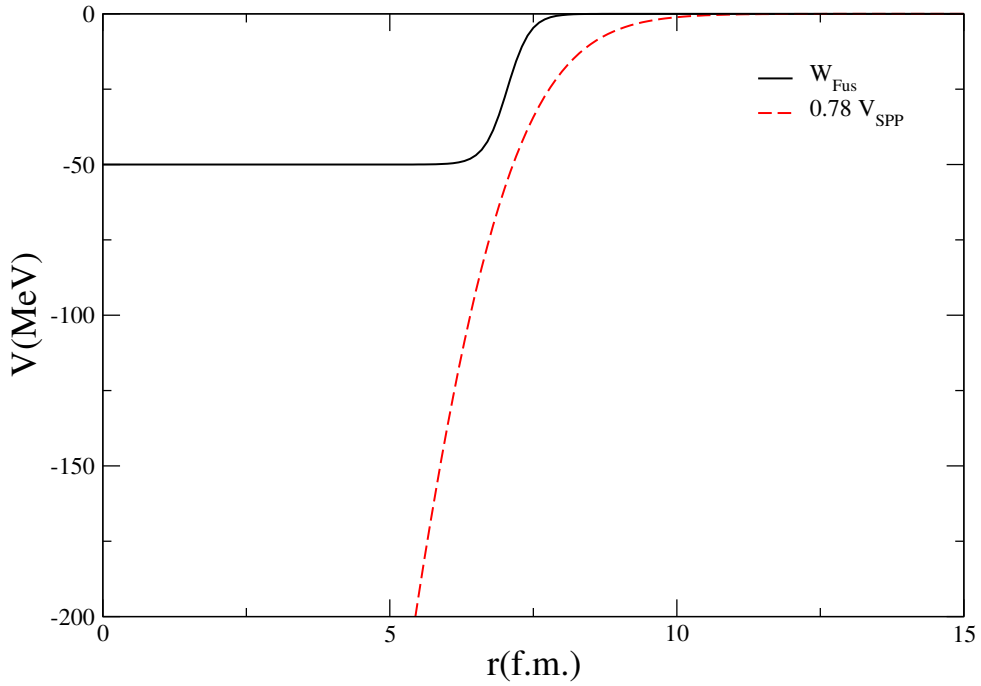

Figure 2.5: Comparison between the potentials used to generate the wave functions.

charge of the collision partners. Some reduction methods are frequently available [62–64]. These procedures have some limitations. With some of these limitations in mind, Ref. [65] defined the fusion function, F:

$$F(x) = \frac{2E}{\hbar\omega R_B^2}\sigma_F, \quad x = \frac{E - V_B}{\hbar\omega}, \tag{2.63}$$

where $\hbar\omega$ is the barrier curvature, R_B is the barrier radius, and V_B is the height of the barrier. The difference between this method for the others is that the fusion functions take into account the radius, height, and barrier curvature. The others do not take into account this last term. It is important to note that this parameter is directly related to the tunneling of the barrier, which has an important effect on the fusion.

Ref. [65] make it clear that Eq. 2.63 is motivated by Wong's formula for fusion cross section [62],

$$\sigma_F^W = R_B^2 \frac{\hbar\omega}{2E} \ln\left[1 + e^{\frac{2\pi(E-V_B)}{\hbar\omega}}\right]. \tag{2.64}$$

If it is possible to use Wong's formula in the reaction, $F(x)$ becomes:

$$F_0(x) = \ln\left[1 + e^{2\pi x}\right]. \tag{2.65}$$

The $F_0(x)$ is the universal fusion function (UFF), that does not depend on the system. So, the experimental data for different systems can be compared to it. If the fusion function of some experimental data deviates from the UFF, this must be due to the coupling with some channels. The strength of the deviation can give information about the intensity of the couplings. However, as pointed out by Canto *et al.* in Refs. [65, 66], the UFF method has shortcomings. The effect of the breakup process on fusion is not evidenced in

this procedure because the effect of bound channel couplings can be very strong. Wong's formula is inaccurate in describing light systems where the approximation by a parabola is not good for describing the Coulomb barrier. Because of that, Canto *et al.* [65] introduce the renormalized fusion function:

$$\bar{F}_{\rm exp}(x) = F_{\rm exp}(x)\frac{\sigma_F^W}{\sigma_{CC}}, \tag{2.66}$$

where $F_{\rm exp}$ is the experimental fusion function and σ_{CC} is the fusion cross section obtained by the coupled channels method. This method allows for isolating the effect of the coupling with the breakup channels. The deviation of the renormalized fusion function of the UFF must come from the channels left out in the couple channel calculations.

Beyond the comparison between the different systems, this method allows us to distinguish the effect of channel coupling on fusion. Furthermore, when using the UFF method, if the more important couplings with the bound states are accounted for in CC calculations, the experimental results converge to the UFF. However, due to the effect of the breakup on the stable and unstable weakly bound projectiles on heavy targets, a suppression of about 30% in the fusion function above the barrier and a small enhancement below it was found [65].

Chapter 3
Continuum-Discretized Coupled Channels methods

Dealing with weakly bound nuclei, the CC or CRC methods may describe the reaction channels poorly. Other observables may not be well described even when the optical potential is adjusted (considering only the standard values for the potential parameters) to fit the elastic cross section. As the internal energy of the nucleus is higher than the binding energy, the continuum is excited, and eigenvalues are not discreet anymore. This implies the necessity to deal with the wave functions in the continuum. They do not belong to the Hilbert space.

Firstly, some reaction channels can occur when involving a weakly bound nucleus. Fig. 3.1 represents some possibilities for fusion and other reaction mechanisms triggered by breakup for a weakly-bound projectile that breaks into two fragments. Direct complete fusion (DCF) is when the projectile fuses completely with the target before it breaks. Another possibility is that the projectile breaks, and all the fragments fuse with the target. This is called sequential complete fusion (SCF). This scenery is experimentally indistinguishable from the DCF. So, experimentally DCF+SCF=CF is measured. When only one of the fragments fuses with the target, the process is known as incomplete fusion (ICF). If all the fragments fly away from the target after the breakup, the process is called elastic breakup (or inelastic breakup if the target or the projectile's core is excited).

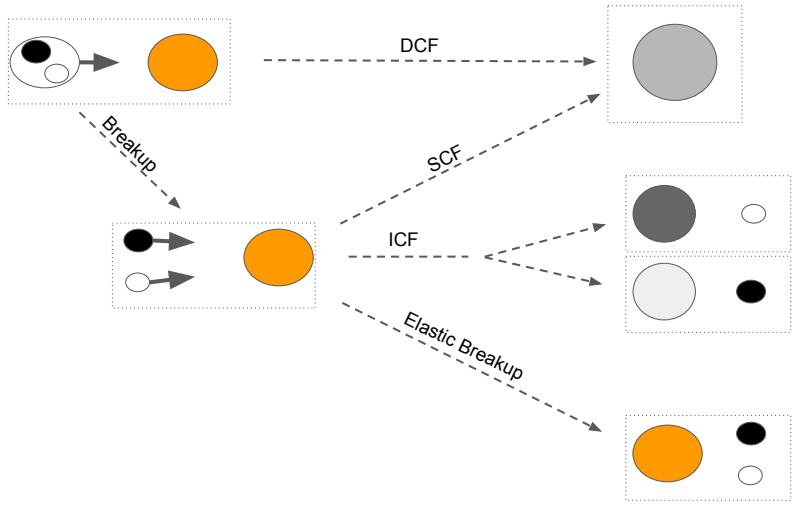

Figure 3.1: Scheme of the possibility for the breakup process considering the weakly bound nuclei fragments in two particles.

When the projectile breaks into two fragments, the reaction can be described as

a three-body problem considering the core, the target, and the valence particle. Yet, in some cases, the projectile breaks in more than two fragments, as in the case of the ^{6}He with a Borromean structure breaking in ^{4}He and two neutrons. The simplest case is called an elastic breakup when the breakup of the projectile will leave the target in its ground state. Nevertheless, as Fig. 3.1 shows, it is possible to occur other reactions. In some experiments, measuring the inclusive reaction and the inelastic breakup is possible.

Several attempts have been made to deal with weakly bound systems. Each of the attempts has its advantages and disadvantages. In this work, the bin method is used. The continuum is discretized considering fixed intervals, bins, of κ-values in the continuum space.

3.1 Three-body Formalism, Jacobi and hyperspherical coordinates.

The Jacobi coordinates can be used to treat a three-body problem. One of three Jacobi coordinates possibilities is depicted in Fig. 3.2.

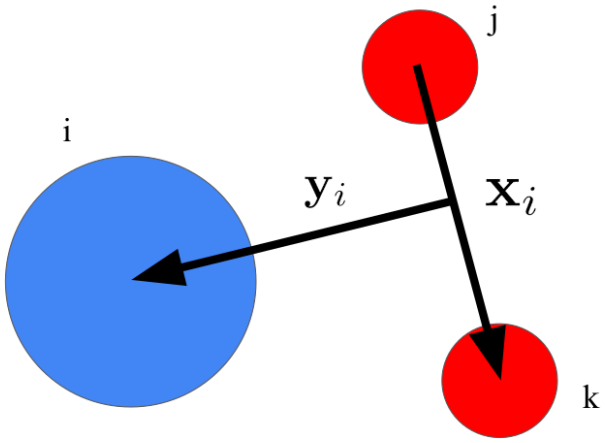

Figure 3.2: Representation of the Jacobi coordinates.

$$\begin{aligned} \vec{x}_i &= (\vec{r}_j - \vec{r}_k)\sqrt{\frac{a_{x_i}}{m}}, \\ \vec{y}_i &= \left(\vec{r}_i - \frac{m_j\vec{r}_j + m_k\vec{r}_k}{M_T + m_i}\right)\sqrt{\frac{a_{y_i}}{m}}, \end{aligned} \tag{3.1}$$

a_{x_i} and a_{y_i} are normalization mass, and m is an arbitrary normalization mass.

$$\begin{aligned} a_{x_i} &= \frac{m_j m_k}{M_T - m_i}, \\ a_{x_i} &= \frac{m_i(M_T - m_i)}{M_T}. \end{aligned} \tag{3.2}$$

Above, $M_T = (m_i + m_j + m_k)$ is the total system mass. The Jacobi sets obey the rules of even permutations. In this way, the position of the three-body system can be completely

determined by the Jacobi sets, and the center of mass coordinate $\vec{R} = \frac{m_i\vec{r}_i+m_j\vec{r}_j+m_k\vec{r}_k}{M_T}$. The position of each particle is given by:

$$\begin{aligned}
\vec{r}_i &= \vec{R} + \frac{m_j+m_k}{M_T}\sqrt{\frac{m}{a_{y_i}}}\vec{y}_i \\
\vec{r}_j &= \vec{R} - \frac{m_i}{M_T}\sqrt{\frac{m}{a_{y_i}}}\vec{y}_i + \frac{m_k}{m_j+m_k}\sqrt{\frac{m}{a_{x_i}}}\vec{x}_i \\
\vec{r}_k &= \vec{R} - \frac{m_i}{M_T}\sqrt{\frac{m}{a_{y_i}}}\vec{y}_i - \frac{m_k}{m_j+m_k}\sqrt{\frac{m}{a_{x_i}}}\vec{x}_i
\end{aligned} \tag{3.3}$$

The Jacobi sets can be connected using the following relations:

$$\begin{aligned}
x_k &= -\cos(\phi_{ki})\ \vec{x}_i + \sin(\phi_{ki})\ \vec{y}_i, \\
y_k &= -\sin(\phi_{ki})\ \vec{x}_i - \cos(\phi_{ki})\ \vec{y}_i,
\end{aligned} \tag{3.4}$$

where,

$$\tan(\phi_{ki}) = (-1)^P\sqrt{\frac{m_jM_T}{M_T-m_j}}, \tag{3.5}$$

the term $(-1)^P$ is due the even permutation of the Jacobi sets. Besides, The set of hyperspherical coordinates $(\rho, \alpha_i, \hat{x}_i, \hat{y}_i)$ can be define from the Jacobi coordinates:

$$\begin{aligned}
\rho^2 = x_i^2 + y_i^2, \qquad \tan(\alpha_i) = \frac{x_i}{y_i}, \ \text{ or} \\
x_i = \rho\sin(\alpha_i), \qquad y_i = \rho\cos(\alpha_i).
\end{aligned} \tag{3.6}$$

The hyperangle relation between different sets is:

$$\tan\alpha_j = \frac{\cos\phi_{ij}\ \sin\alpha_i - \sin\phi_{ij}\ \cos\alpha_i}{\sin\phi_{ij}\ \sin\alpha_i + \cos\phi_{ij}\ \cos\alpha_i} \tag{3.7}$$

The hyperangle in the Jacobi set is defined in the range, $0 < \alpha_i < \pi/2$. The angular dependence, $\Omega \equiv (\alpha_i, \hat{x}_i, \hat{y}_i)$ with the hyperradius represents the full set of hyperspherical coordinates. With these definitions the volume element is given by:

$$d^3\vec{x}_i d^3\vec{y}_i = \rho^5(sin\alpha_i)^2(cos\alpha_i)^2 d\rho\ d\alpha_i\ d\hat{x}_i\ d\hat{y}_i = \rho^5 d\rho\ d\Omega_i. \tag{3.8}$$

3.2 Binning method

The three-body continuum discretized coupled channels using binning method has been successfully applied to some reactions involving light and heavy ions [42, 47–49, 67]. It is natural to try to extend the technique to the four-body CDCC. The theoretical formulation is quite similar to the three-body with the difference that the internal wave functions to be split into bins are now three-body wave functions.

The *continuum binning* method truncates the energy or momentum space and divides it into intervals with specific properties. For that, we consider the reduction of the Jacobi set. For the three-body CDCC, considering the following equation,

$$[H_{3\text{b}} - E]\Psi^{(1)}(\mathbf{r}, \mathbf{R}) = 0, \tag{3.9}$$

where H_{3b} is the three-body Hamiltonian and the label (1) corresponds to the bound state. The coordinate $\mathbf{r}$ corresponds to the distance between the core and valence particles of the projectile and $\mathbf{R}$ to the distance between the projectile center of mass and the target. In this case the $\Psi^{(1)}(\rho, \alpha)$ behaves asymptotically as,

$$\Psi^{(1)} \to \sum_i \phi_i(\mathbf{r})\psi_i(\mathbf{R}) + \text{breakup}, \quad \mathbf{R} \to \infty, \tag{3.10}$$

where $\phi_i(\mathbf{r})$ is the internal wave function of the core plus the valence particle and the $\psi_i(\mathbf{R})$ is some of an incident plane wave and the outgoing spherical wave. In the case of Borromean nuclei, the internal wave functions have a three-body character. Using the hyperspherical harmonics expansion basis, it is possible to write the bin wave function as

$$\phi^{\text{bin}}_{nj\mu}(\mathbf{x}, \mathbf{y}) = \sum_\beta R^{\text{bin}}_{n\beta j}(\rho) \left[\Gamma^{l_x l_y}_{Kl}(\Omega) \otimes \chi_{S_x}\right]_{j\mu}, \tag{3.11}$$

where β is the abbreviation of the set of the quantum numbers $\{(l_x, l_y)l, (S_j, S_k)S_x\}j; I$, $R^{\text{bin}}_{n\beta j}(\rho)$ are the hyper-radial wave functions, and the term $\left[\Gamma^{l_x l_y}_{Kl}(\Omega) \otimes \chi_{S_x}\right]_{j\mu}$ is the angular components of the expansion. The associated orbital angular momenta $l = l_x + l_y$ and the total spin S_x are associated with coordinates $\mathbf{x}$. Therefore, fixing the spin of the third particle, one can define their spin, I, and total angular momentum is $j = l + S_x + I$ with projection μ. Another important quantum number to be defined is the hyper-angular-momentum, $K = 2n + l$, where $n = 0, 1, 2, ...$

It is important to note that, as the wave functions are eigenvectors of the Hamiltonian and the continuum spectrum is populated, one has a continuum of the three-body wave functions. The coupled channel method requires a discretized and finite number of channels. Because of that, it is important to discretize the continuum and to truncate the maximum energy or angular momentum $\kappa = \sqrt{\frac{2\mu_T \varepsilon}{\hbar}}$.

The binning method considers that the eigenstates of the internal Hamiltonian can be obtained for some intervals $[\kappa_n, \kappa_{n+1}]$. The wave function for each bin (wave packet) is obtained as a superposition of scattering wave functions. For this reason, one can divide the total interval $[0, \kappa_f]$ in smaller intervals, $[0, \kappa_1]$,$[\kappa_1, \kappa_2]$,...,$[\kappa_{n-1}, \kappa_n]$. Using this method, it is possible to transform the continuum into a continuum discretized space. With this in mind, the associated hyper-radial wave functions is

$$R^{\text{bin}}_{n\beta j}(\rho) \equiv R^{\text{bin}}_{[\kappa_1,\kappa_2]\beta'\beta j}(\rho) = \frac{2}{\sqrt{\pi N_{\beta' j}}} \int_{\kappa_1}^{\kappa_2} d\kappa \; e^{-i\delta_{\beta' j}(\kappa)} f_{\beta' j}(\kappa) R_{\beta\beta' j}(\kappa, \rho), \tag{3.12}$$

where $f_{\beta' j}(\kappa)$ is a weight function normalized by the factor $N_{\beta' j}$. The $R_{\beta\beta' j}(\kappa, \rho)$ are the hyper-radial wave functions with scattering phase shift $\delta_{\beta' j}(\kappa)$. The β and β' are the outgoing and incoming channels, respectively. n is the bin label. For each β, β', and j, there is one bin wave function. The bin wave functions eq. 3.12 are orthogonal to the bound states and to each others if they does not overlap in the energy space. The energy of each bin is defined as the energy of the middle of the interval considered. A representation of the continuum space equally spaced in energy is shown in Fig. 3.3. The bound states are represented by two discrete states and the unbound states are represented by lighter

colors bins. The total number of bins is usually large. This implies a quick increase in the computational time. Some assumptions have to be made to overcome this issue. One of them is to truncate the number of basis states by choosing a more relevant set to describe the physical process under research.

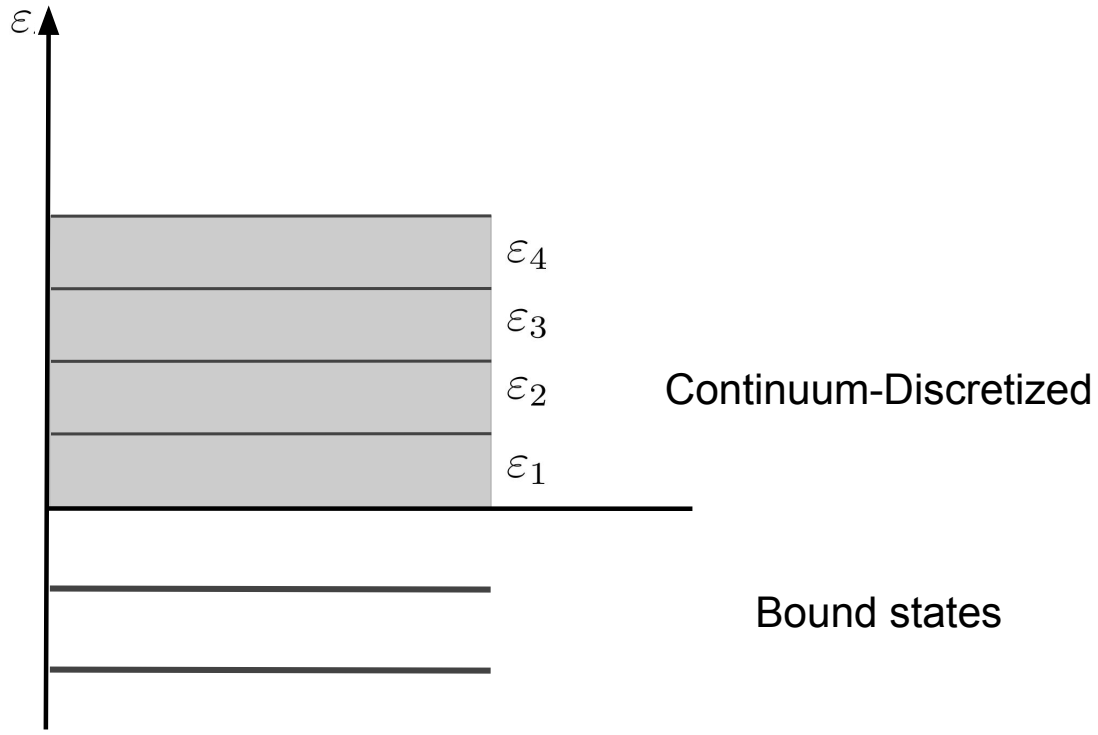

Figure 3.3: Representation of the energy space of a weakly bound nucleus. The bins represented are discretized in the energy space.

Using the eigenchannels (ECs) of the three-body S-matrix [68], it is possible to determine if the chosen set of states (the truncated basis) considered the most relevant contributions to describe the scattering observables. The ECs are found by diagonalizing the S-matrix in the outgoing channel, α, for each j and κ. The ECs eigenvalues and eigenphases are $\exp[2i\delta_{\gamma j}(\kappa)]$ and $\delta_{\gamma j}(\kappa)$, respectively, where γ is the label of the eigenchannel. The largest are phase shifts, the stronger the couplings in the reaction. In this way, the phase shift magnitude can be used to order the eigenchannels and truncate the basis. The number of eigenphases considered, n_{ec}, should be tested upon convergence.

As described in section 2.5, the channel wave function is the product of the intrinsic wave function of the projectile and the projectile and target wave function

$$\Psi_{JM}(\mathbf{R},\rho,\Omega) = \sum_{nj\mu LM_L} \psi^{\text{bin}}_{nj\mu}(\rho,\Omega)\langle LM_L j\mu|JM\rangle i^L Y_{LM_L}(\hat{R})\frac{1}{R}f^J_{Lnj}(R). \tag{3.13}$$

Above, $J = L + j$ is the total angular momentum, L - the orbital angular momentum of the projectile-target relative motion, and $\mathbf{R}$- the coordinate from the target to the center of mass of the projectile. It is important to note that we are not considering the internal

structure of the target. Besides that, the $f^J_{Lnj}(R)$ are the scattering radial function that satisfies the following system of equations:

$$\left[-\frac{\hbar^2}{2\mu_r}\left(\frac{d^2}{dR^2}-\frac{L(L+1)}{R^2}\right)+\varepsilon_{nj}-E\right]f^J_{Lnj}(R)+\sum_{L'n'j'}i^{L'-L}V^J_{Lnj,L'n'j'}(R)f^{J'}_{L'n'j'}(R)=0, \tag{3.14}$$

and the form-factors in the previous expression are defined as,

$$V^J_{Lnj,L'n'j'}(R)=\langle Lnj\ JM|V_{\mathrm{p\,t}}(\mathbf{r}_1,\mathbf{r}_2,\mathbf{r}_3)|L'n'j'\ JM\rangle, \tag{3.15}$$

where the ket $|Lnj\ JM\rangle$ denotes the projectile wave function in the bin basis, $\psi^{j\mu}_{n\,\mathrm{bins}}(\rho,\Omega)$. The form-factors are calculated assuming that the interaction can be represented by two-body interaction of each projectile fragment with the target.

Chapter 4
Reactions in the ^{9}Be + ^{197}Au system

The ^{9}Be nucleus can be described using various cluster configurations, d + ^{7}Li, ^{3}H + ^{6}Li,^{3}He + ^{6}He, n+ ^{8}Be, and α +$\alpha + n$ systems. The more frequently used cluster configurations in the literature in reaction or structure calculations are illustrated in Fig. 4.1. The reactions involving this weakly bound nucleus have been largely studied in the literature [5–7, 25, 26]. The Borromean structure α+$\alpha + n$ is quite similar to the structure of the ^{6}He and ^{11}Li but with larger binding energy. Unlike ^{6,7}Li, whose predominant cluster structures are $\alpha + d$ and $\alpha + t$, the case for ^{9}Be is unclear [69–72].

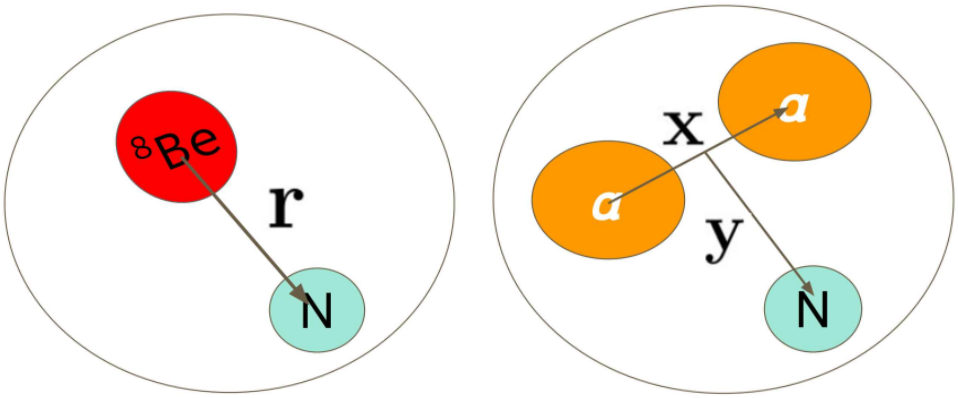

Figure 4.1: Representation of two cluster models to the ^{9}Be

Due to the cluster structure of the ^{9}Be, two reaction mechanisms are more likely: i) breakup of the ^{8}Be with a half-life of 7×10^{-17}s produced by one-neutron transfer, and ii) breakup through ^{9}Be $\rightarrow \alpha + \alpha + n$ or ^{9}Be $\rightarrow$ ^{5}He+α with a half-life of the order of 10^{-21}s. The ground state has total angular momentum $j^{\pi} = 3/2^{-}$ and a binding energy of 1.5736 MeV when considering the structure α+α+n. Several resonances can be listed. Some of then has the angular momenta $j^{\pi} = 1/2^{+}, 5/2^{-}, 1/2^{-}, 5/2^{+}, 3/2^{+}$ [73]. Several researchers process can be found in the literature investigating this resonances and many others with the objective to determine there positions and widths [74, 75].

The ^{9}Be + ^{197}Au reactions were recently studied by Gollan *et al.* [2, 76], Li *et al.* [7], and Kaushik *et al.* [3]. The author's Li *et al.* and Kaushik *et al.* reported a fusion cross section, and Gollan *et al.*, besides the fusion cross section, reported elastic and one-neutron (pickup and stripping) cross section. In this section, this reactions will be analyzed using different reactions methods as discussed above.

4.1 Analyse of elastic and inelastic channel

The description of the elastic and inelastic cross section in a nuclear reaction is some times difficult due to the strong dependence on the optical potential. A good description of these observables indicates that the correct potential was considered. The Woods-Saxon potential is largely used in the literature to describe the elastic cross section for many systems. However, this potential has many free parameters that need to be adjusted. Different values for the potential parameters can generate the same result in the cross section, and this effect is called ambiguities of the potential. The são Paulo Potential systematic can be used to overcome the necessity of adjusting free parameters, as presented in the subsection 2.3.2. This work used the SPP systematic in the CC and CRC calculations to describe the reactions.

The CC calculations was performed using the FRESCO code [77], considering the ground state of ^{9}Be and six states of the ^{197}Au, as one can see in Fig. 4.2. The SPP was used in the real and imaginary parts of the potential, as indicated by the systematic, the imaginary part of the potential is multiplied by a strength factor, $U = V_{SPP}\,(1 + iN_i)$. As couplings with excited states of the target where considered, $N_i = 0.60$ was used for the imaginary part. This strength factor accounts for the bound and continuum channels not explicitly considered. Another critical issue in the reaction are the collective states of the target, the transition probabilities, defined in Sec. 2.4, that play an important role in the description of the cross section of these states. The $B(E\lambda)$ where taken from Ref. [78].

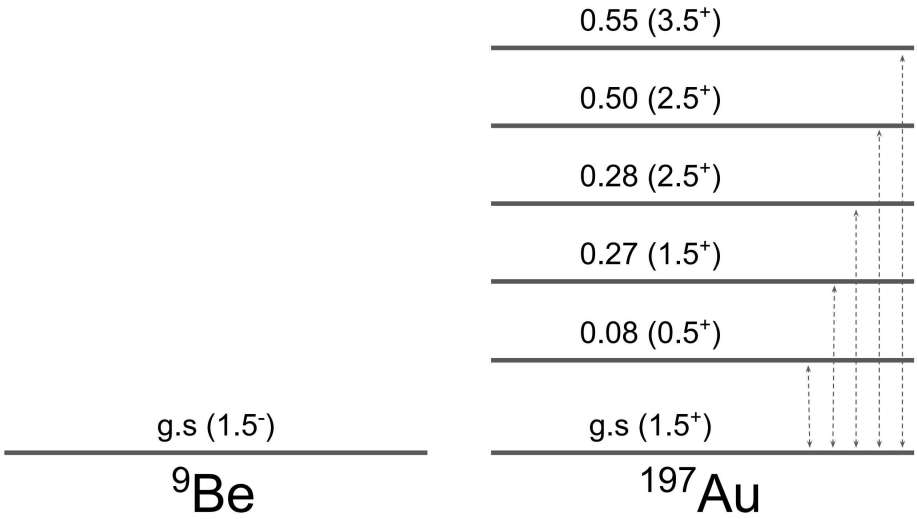

Figure 4.2: States scheme for the ^{9}Be + ^{197}Au System.

The results of CC calculations for the elastic scattering angular distributions are compared in Figs. 4.3, 4.4, and 4.5 with the measured experimental data. These experimental data were measured in the Tandar Laboratory of Buenos Aires by our collaborators. In general, a good agreement with the experimental data is observed.

Fig. 4.3 shows a good agreement between the experimental data and the theoret-

ical calculations, showing that the SPP systematic is a good choice to describe well the elastic cross section of this system at this energy regime. At energies very close to the Coulomb barrier, the theoretical predictions slightly overestimate the experimental data at backward angles. This can be seen for energies 37 MeV and 38 MeV, from Fig. 4.4. For these energies, maybe the approximation to simulate other reaction channels not explicitly included in the coupling scheme by strength coefficient is not proper. The agreement with the experimental data is very good for energies above the Coulomb barrier, as shown in Fig. 4.5.

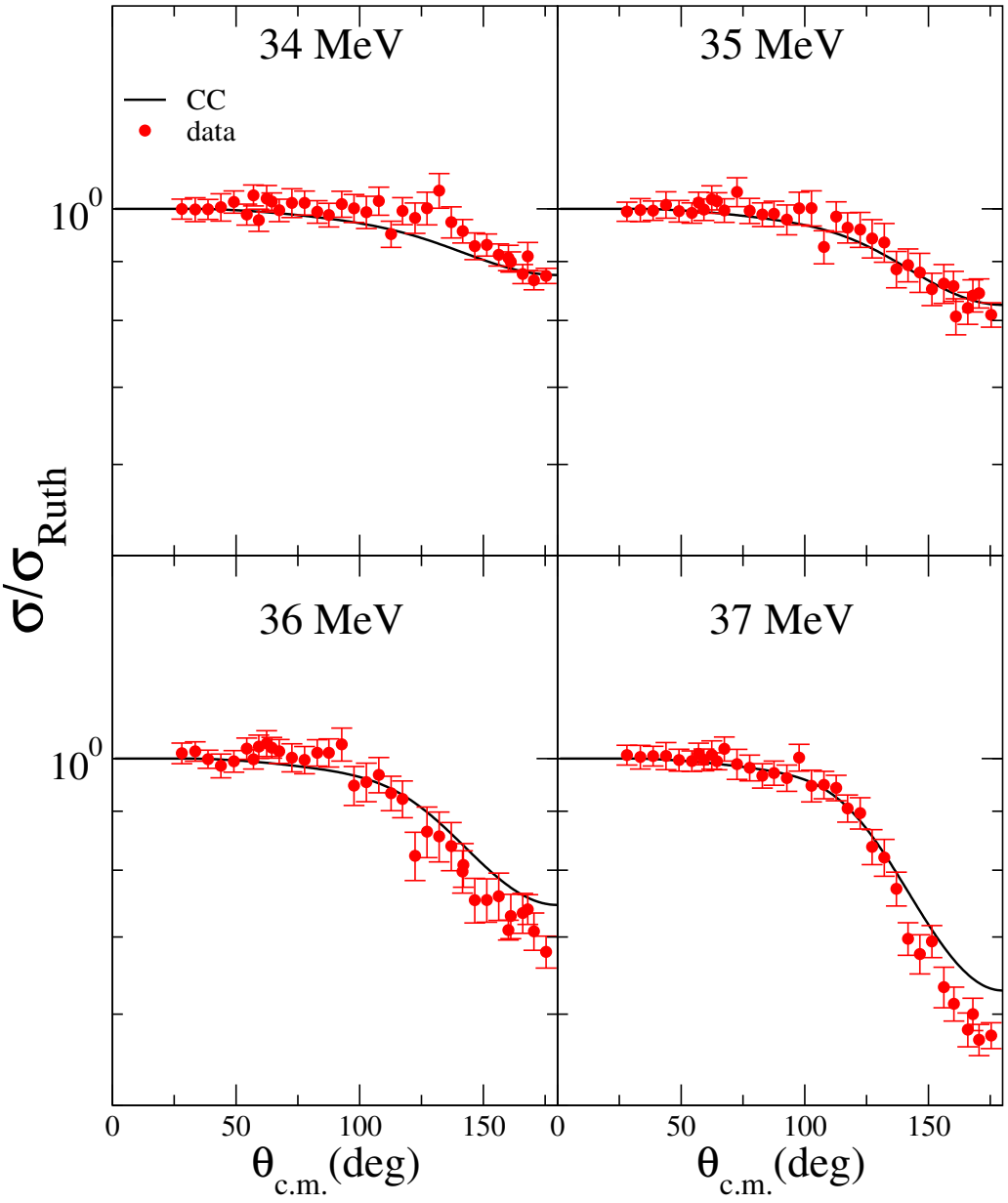

Figure 4.3: Comparison between the experimental data and the theoretical CC calculations for the elastic scattering cross sections in the energy range from 34 up to 37 MeV.

Another important observable derived from the coupled channel calculations is the inelastic cross sections. In the Ref. [76], theoretical results using Woods-Saxons potential for both real and imaginary parts, are compared with the experimental data for two

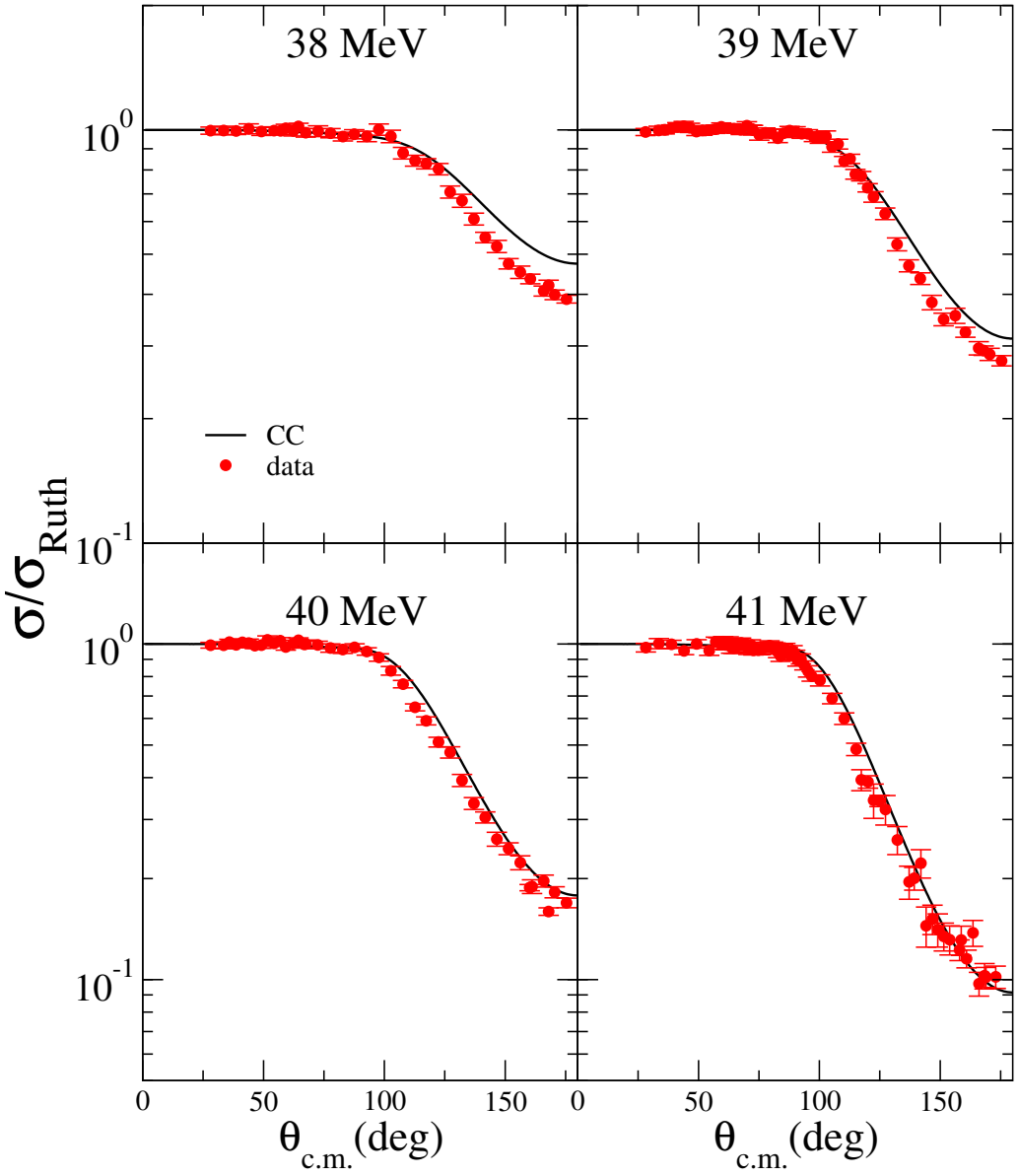

Figure 4.4: Comparison between the experimental data and the theoretical CC calculations for the elastic scattering cross sections in the energy range from 38 up to 41 MeV.

inelastic channels $5/2^+$ state at 279.0 keV and $7/2^+$ state ate 547.5 keV. In this work, will be redone this analysis using the SPP systematic. Fig. 4.6 shows that our calculation reasonably describes the $7/2^+$ state at 547.5 keV. In Ref. [76], it was stated that the experimental data for the $5/2^+$ state at 279.0 keV is contaminated by $3/2^+$ state at 270.0 keV. However, in the theoretical description, this state was not included. As seen from Fig. 4.7, the inclusion of the state at 270.0 keV considerable affects the cross section. Figs. 4.3-4.7 show that the coupled channel results using the SPP systematic satisfactory describe the elastic and inelastic reactions of ^{9}Be+^{197}Au at energy below and above Coulomb barrier.

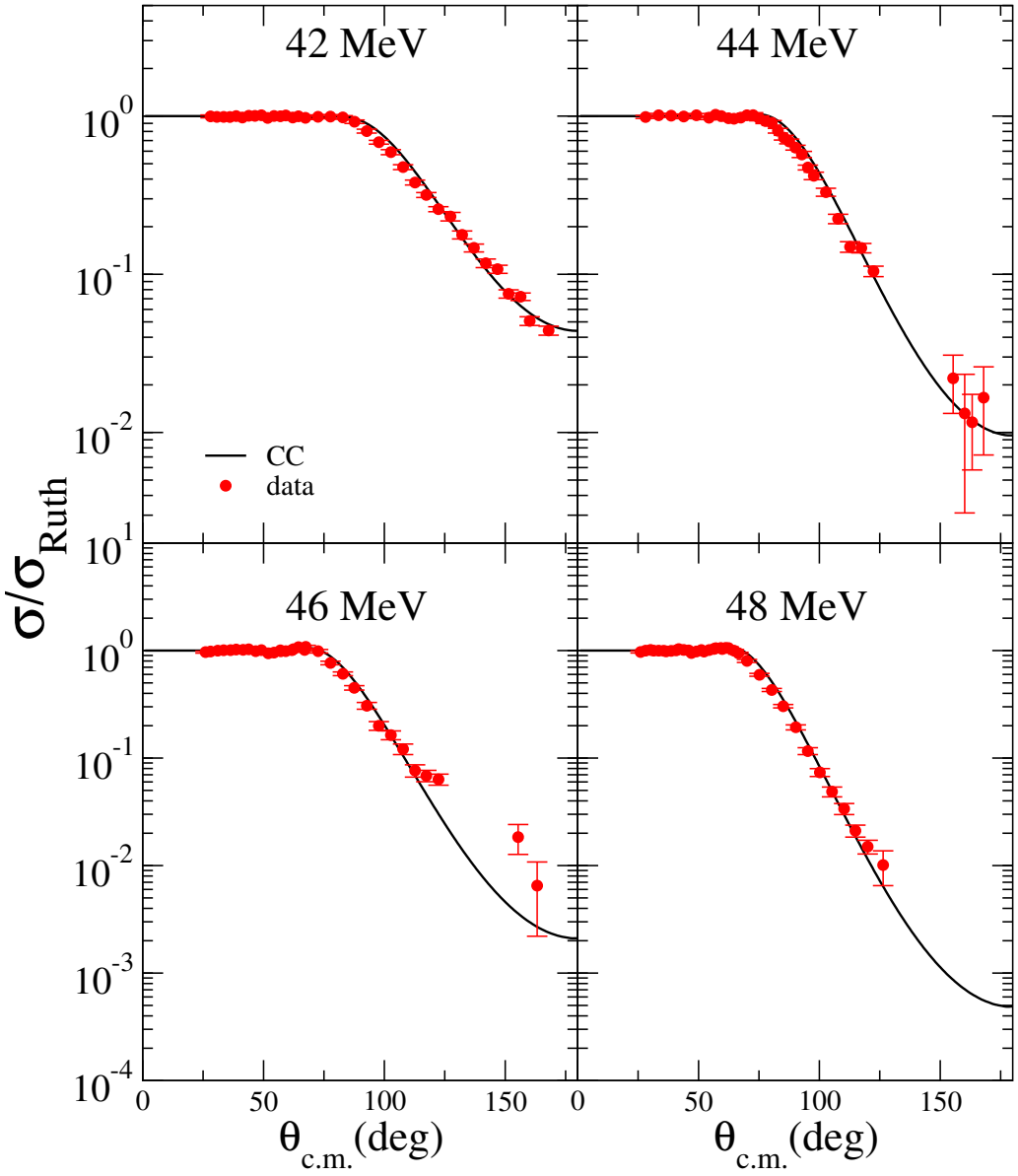

Figure 4.5: Comparison between the experimental data and the theoretical CC calculations for the elastic scattering cross sections in the energy range from 42 up to 48 MeV.

4.2 One-neutron stripping reaction

Another observable measured in this experiment was the one-neutron stripping cross section. This channel was indirectly measured of the evaporation product of the residual nuclei. The coupled reaction channel method was used to calculate the transfer cross sections. The entrance partition is same one in the coupled channel calculations in the previous subsection. The same interactions between the target and the projectile well considered. In the outgoing partition, the SPP was used. However, as we did not explicitly considered the couplings between the states in the final partition, the strength coefficient of the imaginary part was set equal to 0.78 [79]. To generate the single-particle wave functions, the Woods-Saxons form factors were used. The reduced radii was set 1.25 fm and the diffuseness 0.65 fm. The FRESCO code automatically adjusted the depth of the potential to fit the experimental one-neutron separation energy.

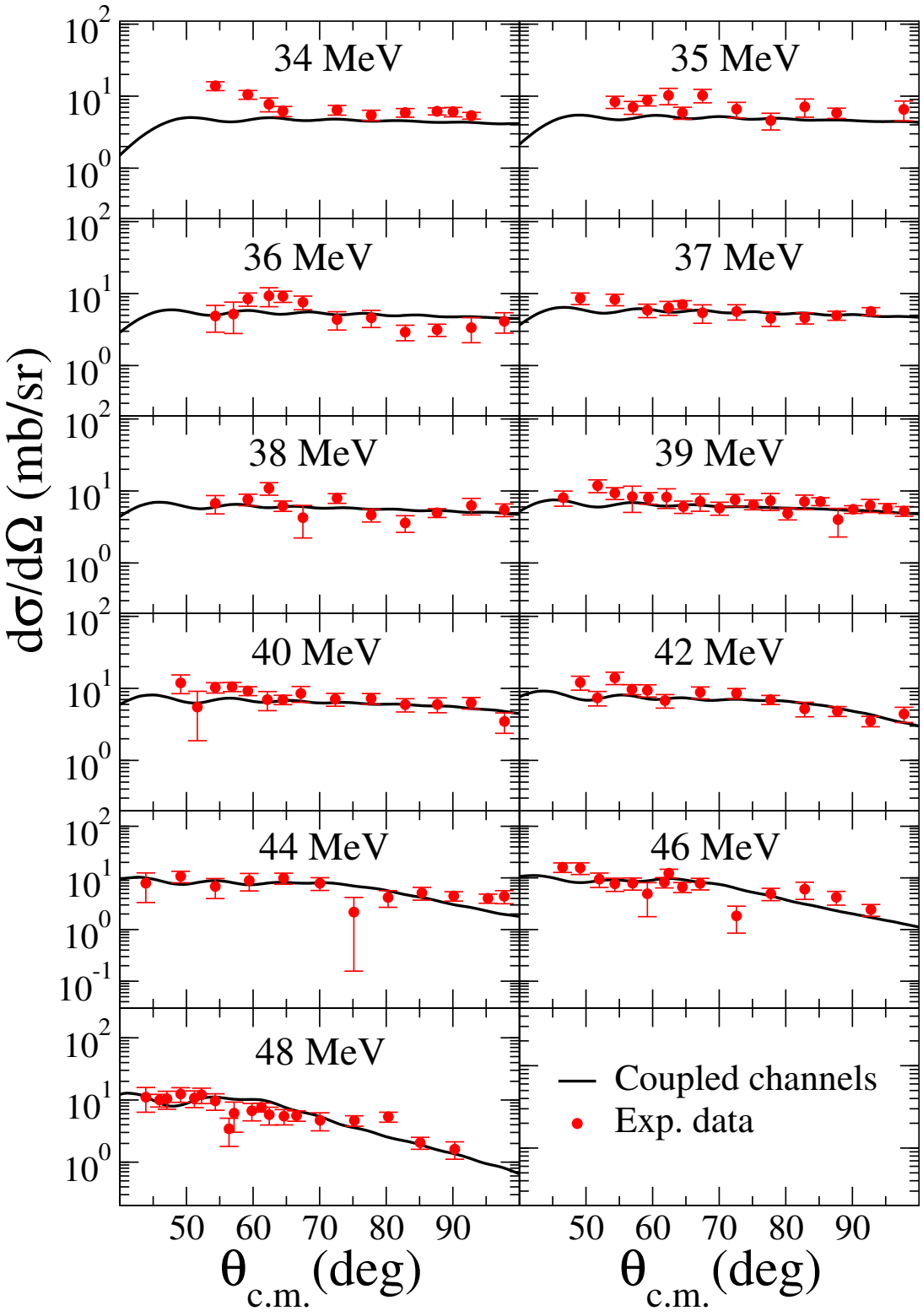

Figure 4.6: Comparison between the experimental data with the theoretical inelastic calculations for the (547.5 keV, $7/2^+$) state.

Another important ingredient to calculate the transfer cross section is the spectroscopic amplitudes defined in Eq. 2.60. For the projectile overlap, $\langle {}^{9}\mathrm{Be}|{}^{8}\mathrm{Be}\rangle$, they were taken from Ref. [80]. Several tests were performed using the NuShellX code [81] to derive the spectroscopic amplitudes for the $\langle {}^{197}\mathrm{Au}|{}^{198}\mathrm{Au}\rangle$ target overlaps. However, the struc-

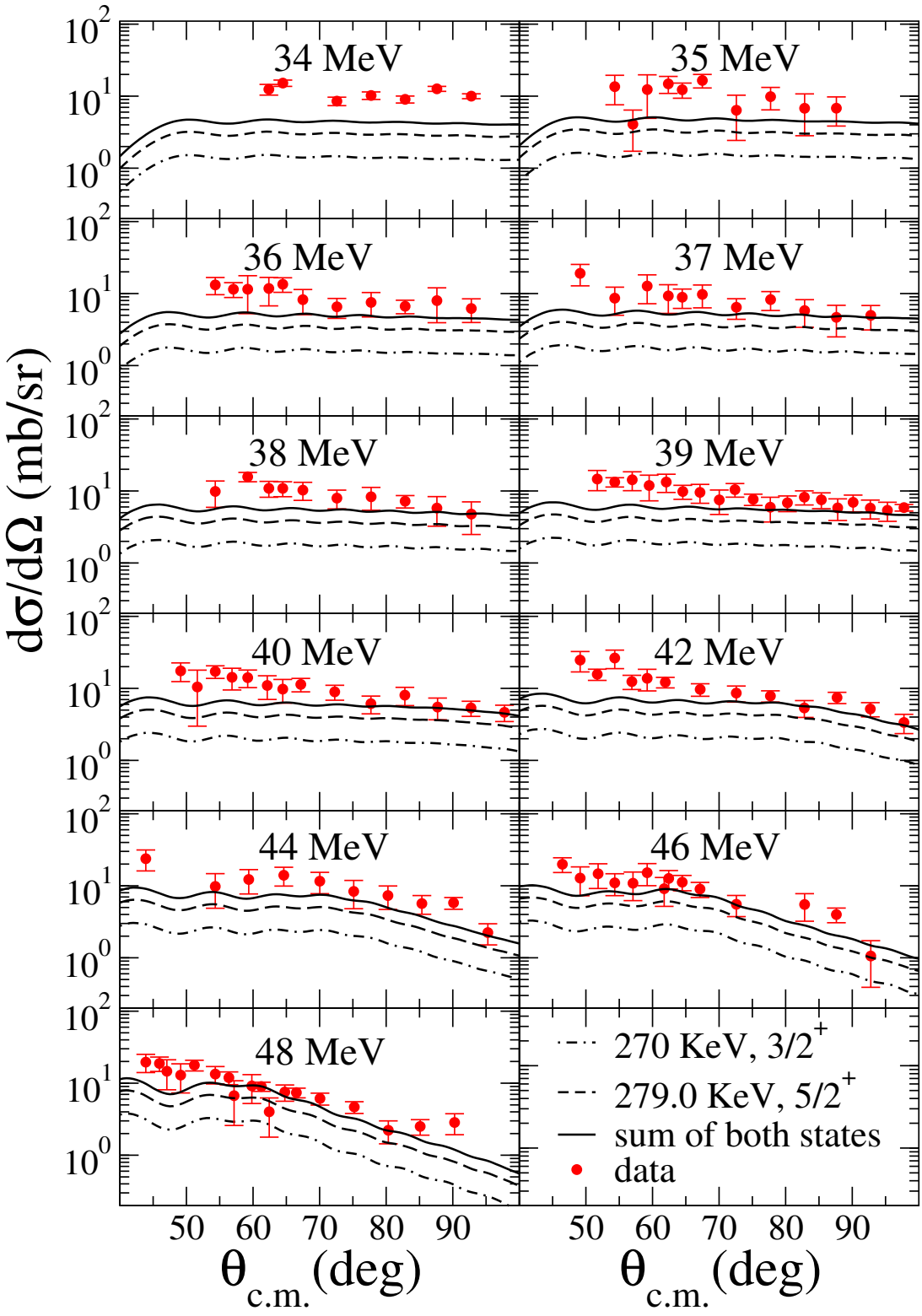

Figure 4.7: Comparison between the experimental data with the theoretical inelastic calculations. The dashed lines represent the cross section of 279.0 keV $(5/2^+)$ and the dash-dotted line represents the 270.0 kev $(3/2^+)$ states of ^{197}Au.

ture calculations were very time-consuming and resulted in an unsatisfactory description of the internal structure of the target and residual nucleus. Because of that, the spectroscopic amplitude was set to 1.0. While the $\mathcal{A}^{lj}_{\beta\alpha}$ can assume values bigger than 1.0,

generally these values are smaller than that. Therefore using $\mathcal{A}^{l\,j}_{\beta\alpha} = 1.0$ we expected to overestimate the transfer cross section. For the target, all the states up to 703 KeV will take into account, as seen in the coupling scheme of Fig. 4.8.

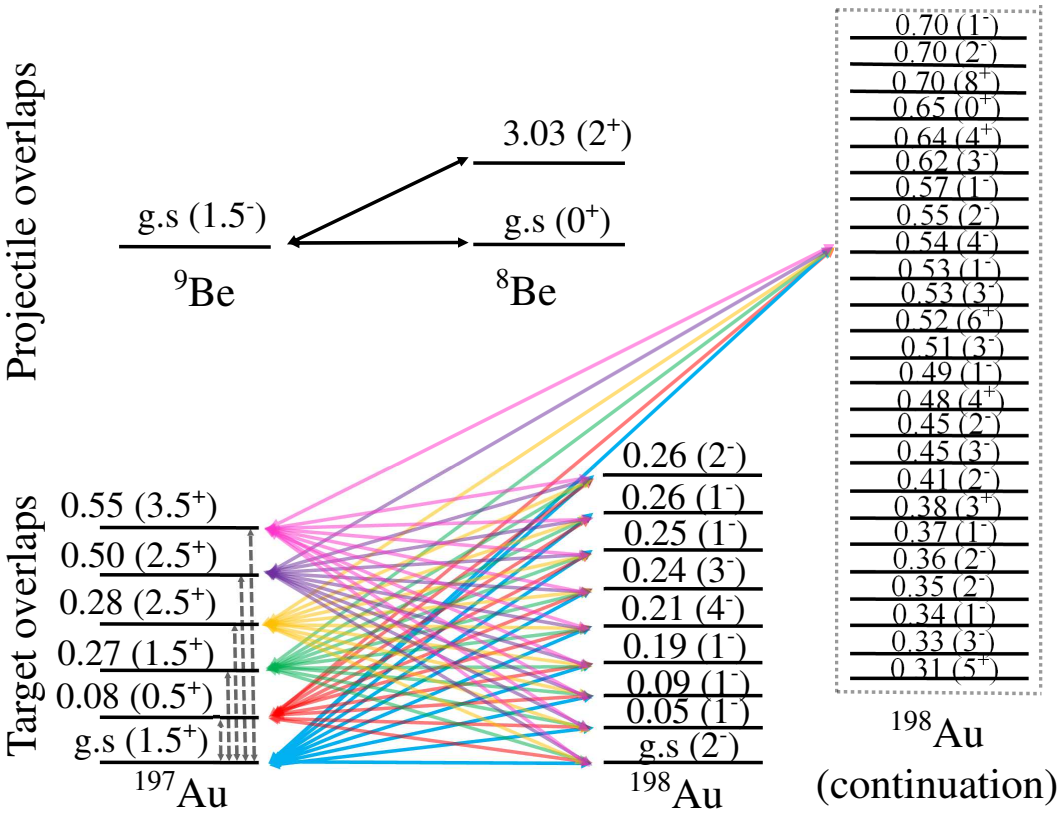

Figure 4.8: Coupling scheme of the projectile and target overlaps used in the one-neutron pickup reaction calculations, taken from Ref. [2].

As can be seen from Fig. 4.9, for energies above 32 MeV, the calculated transfer reaction cross section describes quite well the experimental data. Nevertheless, it was expected that the theoretical calculation might overestimate the experimental data because of the assumed values for the spectroscopic amplitudes. This underestimation can occur because the ^{198}Au has many states even we include only the states up to 1 MeV. Still, it has many others up to 2 MeV, as the level densities increase exponentially with the energy. This is a typical situation for heavy ions. In this reaction, all the states have a small contribution. So, it is possible to note that even when it is considered only the most important states (the ones that have more contribution on the cross section) the cross section became smaller. Because of that, the higher states significantly impact the final value for the cross section. Even if the contribution of each state is small, the density of the states is high at higher energies.

Nevertheless, looking at Fig. 4.9 a significant underprediction of the experimental data is observed at energies below 32 MeV. It is important to note that the ^{9}Be is a weakly bound nucleus. Considering the experimental setup, one cannot distinguish if the

neutron was directly transferred from the projectile or it was absorbed by the target after the projectile was broken. So, was experimentally is reported as a one-neutron stripping reaction might be contaminated by the breakup mechanism which is the most relevant reaction channel at very low energies.

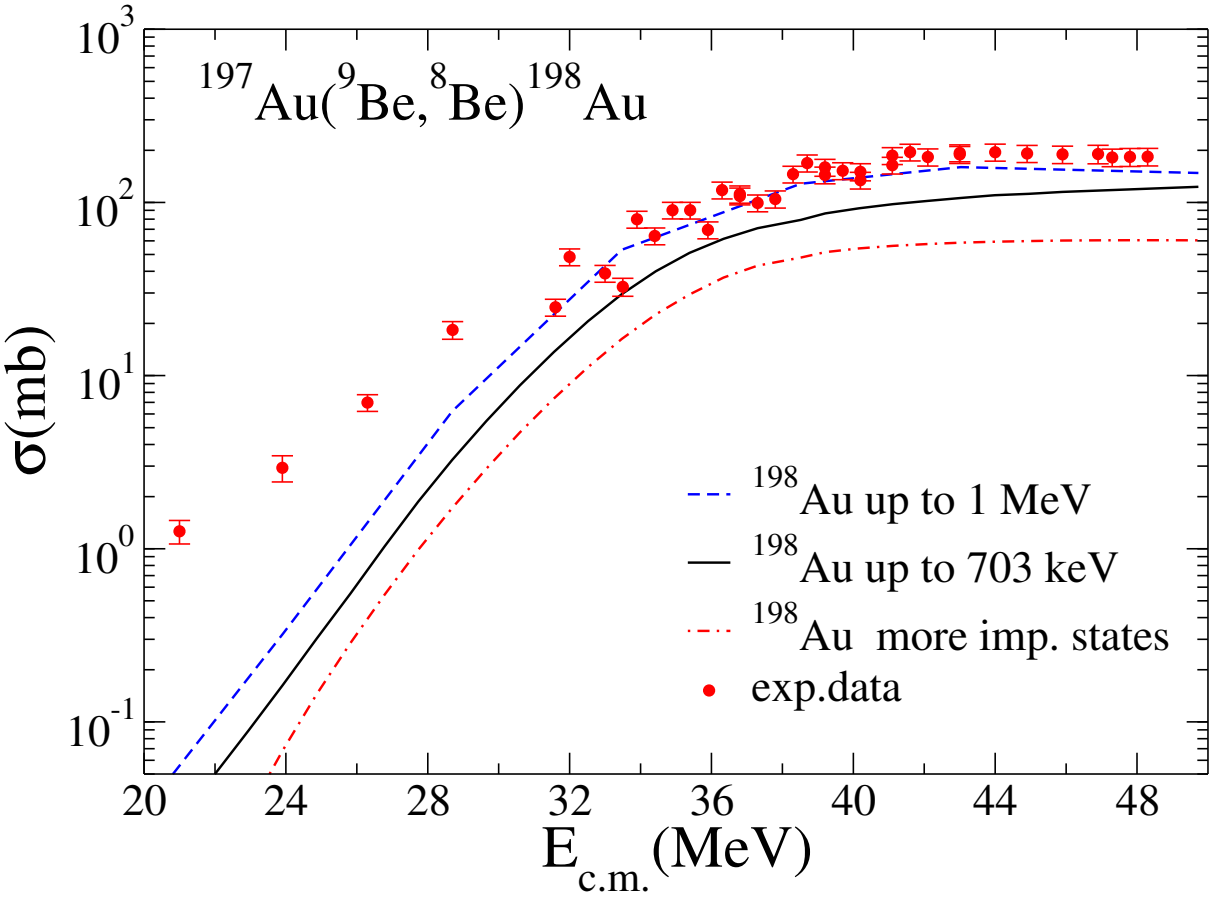

Figure 4.9: Comparison between the experimental data with the theoretical one-neutron transfer cross section.

Another important question is the couplings' contribution to the first resonant state of the ^{8}Be. In other transfer reaction, the contribution of these couplings between the excited states of the final nucleus is negligible for the total cross section. However, in this reaction, the most important contribution to the transfer cross sections arises from these couplings, *i.e.*, the coupling between the first resonant state of the ^{8}Be with the states of the gold. In Ref. [80], the inclusion of the couplings with this state, in the sequential transfer ^{9}Be(^{7}Be,^{9}Be)^{7}Be, has shown not to be important.

Therefore, the description of the experimental data for higher energies considering only the transfer reaction is satisfactory. Although our theoretical description of the reaction is approximated because of the lack of microscopic spectroscopic amplitudes for the target overlaps, it is satisfactory for energies above 32 MeV. Still, the experimental data is more than one order of magnitude above the theoretical calculations for the low energies (below 32 MeV). It is possible that the one neutron transfer can not give a good explanation for that. One explanation for this enhancement in low energies can be incomplete fusion. A preliminary calculation of Professor *Antonio Moro*, from Seville

university, using the Ichimura, Austern, Vincent model corroborates this ICF idea [82].

4.3 One-neutron pickup reaction

The one-neutron pickup cross section was also measured in the experiment. From the theoretical point of view, the calculations to describe the one-neutron pickup and stripping are very similar. The entrance partition is the same as the CC calculations, and the Woods-Saxon form factors follow the same procedure as the stripping calculation. For the $\langle^{197}\mathrm{Au}|^{196}\mathrm{Au}\rangle$, we have the same issue as for the $\langle^{197}\mathrm{Au}|^{198}\mathrm{Au}\rangle$ case, therefore for the same reasons, we assume that $\mathcal{A}^{l\,j}_{\beta\alpha} = 1.0$.

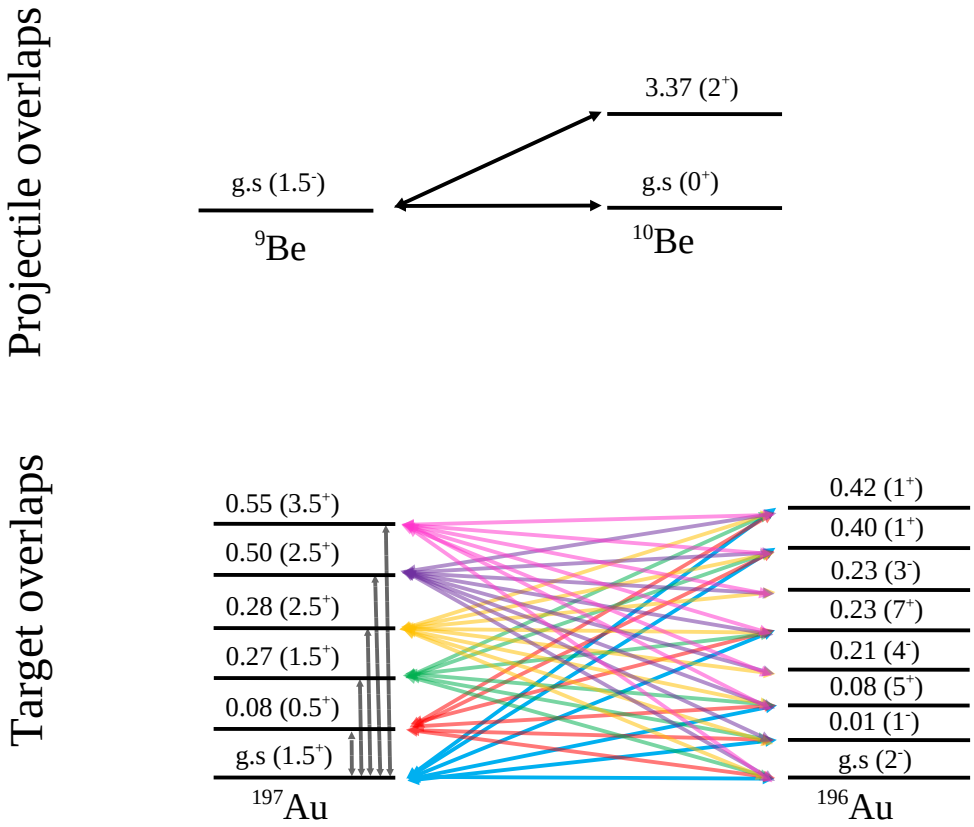

Figure 4.10: Coupling scheme of the projectile and target overlaps used in the one-neutron pickup reaction calculations, taken from Ref. [2].

For the $\langle^{9}\mathrm{Be}|^{10}\mathrm{Be}\rangle$ case, the spectroscopic amplitude was derived by performing shell-model calculations with the NuShellX code [81]. To calculate the overlaps, the *psdpn* model and the effective interaction *psdmod* were used [83]. In this model, we consider the ^{9}Be as ^{4}He closed core with the $1p_{1/2}$, $1p_{3/2}$, $1d_{3/2}$, $1d_{5/2}$, and $2s_{1/2}$ orbitals as the valence space for the nucleons. Table 4.1 shows the spectroscopic amplitudes obtained. It is important to point out that to validate our structure calculations, we compare the theoretical results with the experimental values for the energy, spin, and parity of each state. We consider a good description of spectra if the energy, spin, and parity of the initial and final nucleus states are close to that reported in the literature. If the shell calculations

fulfill these constraints, we can confidently use these spectroscopic amplitudes to obtain the theoretical cross section of the reaction. The coupling scheme for the target and the projectile overlaps are shown in Fig. 4.10.

Table 4.1: Spectroscopic amplitudes used in the CRC calculations for one-neutron pickup reaction calculation.

Initial state	j	Final State	Spect. Amp.
$^{9}\mathrm{Be}_{\mathrm{g.s}}(3/2^{-})$	$(1p_{1/2})$	$^{10}\mathrm{Be}_{\mathrm{g.s}}(0^{+})$	-1.582
$^{9}\mathrm{Be}_{\mathrm{g.s}}(3/2^{-})$	$(1p_{1/2})$	$^{10}\mathrm{Be}_{3.368}(2^{+})$	-0.159

From Fig. 4.11 it is possible to note that the theoretical cross section agrees reasonably well with the experimental data. The couplings between the g.s. of the ^{10}Be and the first excited state of residual ^{196}Au at the 0.01 MeV has the greatest contribution to the total pickup cross section. However, the importance of each state's contribution varies with the bombarding energy. The coupling with the $^{196}\mathrm{Au}_{0.08\mathrm{MeV}}(5^{+})$ state became very relevant above the Coulomb barrier. The coupling with the first-excited state of the residual projectile does not have a significant contribution for the pickup cross section. The contribution is less than 2 orders of magnitude of the total cross section. Indeed, the experimental cross section is slightly different from the theoretical curves. This over-prediction might be originated by the lack of spectroscopic amplitudes for the target overlaps. As mentioned above, due to computational limits, they are not calculated.

These results suggest that our methodology for the treatment of one-neutron transfer in this system has a good agreement with the experimental data. This corroborates the discussion of the last section 4.2, where we believe that the experimental data contain mechanisms other than transfer.

4.4 Fusion

Also, a fusion cross section was reported in the Ref. [2]. Chapter 2 explains the theoretical treatment of the fusion cross section. As this process is strongly affected by the breakup channel, it is very interesting to investigate the importance of this channel in the fusion cross section. One way to do it is to compare the experimental data with the theoretical calculations. The CC channels calculations to estimate the fusion cross section is very similar to the one performed in section 4.1 except for the imaginary part of the potential, which was set as a Woods-Saxson with depth: $W = -50$ MeV, reduced radius: $r_w = 1.06$ fm, and, diffuseness $a_w = 0.2$ fm. Using this procedure, theoretically, it is possible to estimate the fusion cross section without the breakup channel effect. Furthermore, it is important to compare these results with other systems. The fusion function method explained in subsection 2.6.1 will be used for that. To use this reduction procedure, a reliable potential is mandatory. As usual, the São Paulo potential will be used for this purpose. The energy and the experimental cross sections have to be reduced according to the expressions 2.63 and 2.66, using results of CC calculations and compared with the UFF to disentangle the effect of the channels left out in the CC calculations (break up + transfer channels). The barrier parameters from the SPP used to reduce the experimental data for the systems compared in the present work, as well as some information on the

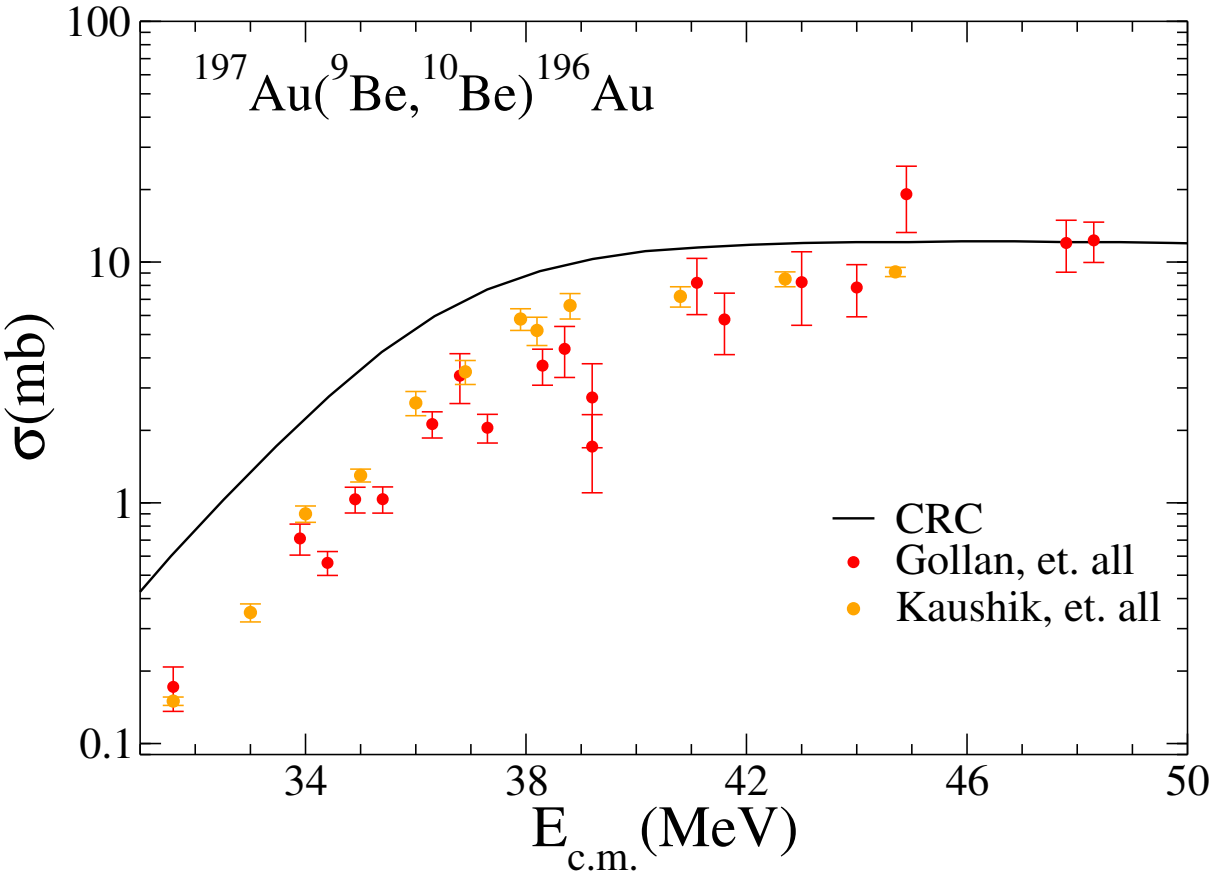

Figure 4.11: Comparison between the experimental data with the theoretical one-neutron pickup calculations, the experimental data as taken from Refs. [2, 3].

	R_B(fm)	V_B(MeV)	$\hbar\omega$ (MeV)
^{9}Be + ^{197}Au	11.35	37.50	4.44
^{9}Be + ^{208}Pb	11.50	38.50	4.42
^{9}Be + ^{209}Bi	11.50	38.96	4.46
^{9}Be + ^{144}Sm	10.07	31.10	4.20

Table 4.2: Barrier parameters for the systems studied.

channels used in the CC calculations, are given in Tab. 4.2.

In Figs. 4.12 and 4.13, the complete and total fusion cross sections for some heavy systems with ^{9}Be as a projectile are compared. It is important to note that as the x is defined, the Coulomb barrier corresponds to $x = 0$, and the cross section values below the barrier are much smaller than the above. For these reasons, the linear scale is used to study the fusion functions above the Coulomb barrier and the logarithmic below it. From Fig.4.12, an enhancement of the CF experimental data at energies below the barrier and the hindrance above it is observed. This behavior is compatible with the expected for the UFF systematic [46].

From Fig. 4.13, it is observed that the TF of the ^{9}Be+^{197}Au system has an unexpected behavior, a hindrance at energies above the barrier. This behavior also appears in the ^{9}Be+^{186}W system. As this hindrance only appears in some cases, the necessity

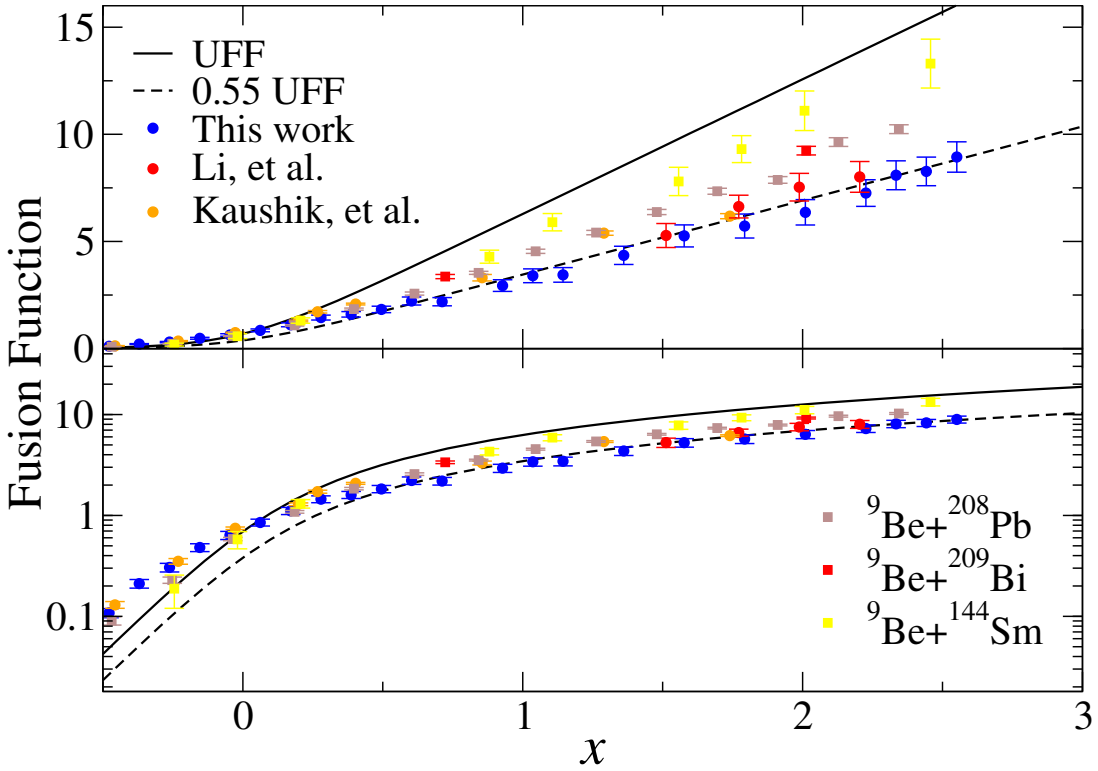

Figure 4.12: Comparison between the UFF and renormalized fusion function for total fusion (CF). The systems are composed by the ^{9}Be projectile on different targets: ^{186}W [4], ^{144}Sm [5], ^{208}Pb [6], ^{197}Au from [7], [3] and this work.

of more experimental data to elucidate the contradiction among different data sets is mandatory. The rest of the systems included in Fig. 4.13 show a typical enhancement at energies below the Coulomb barrier and no effect at above it for the TF observed in other reactions involving other weakly bound projectiles and different targets [46].

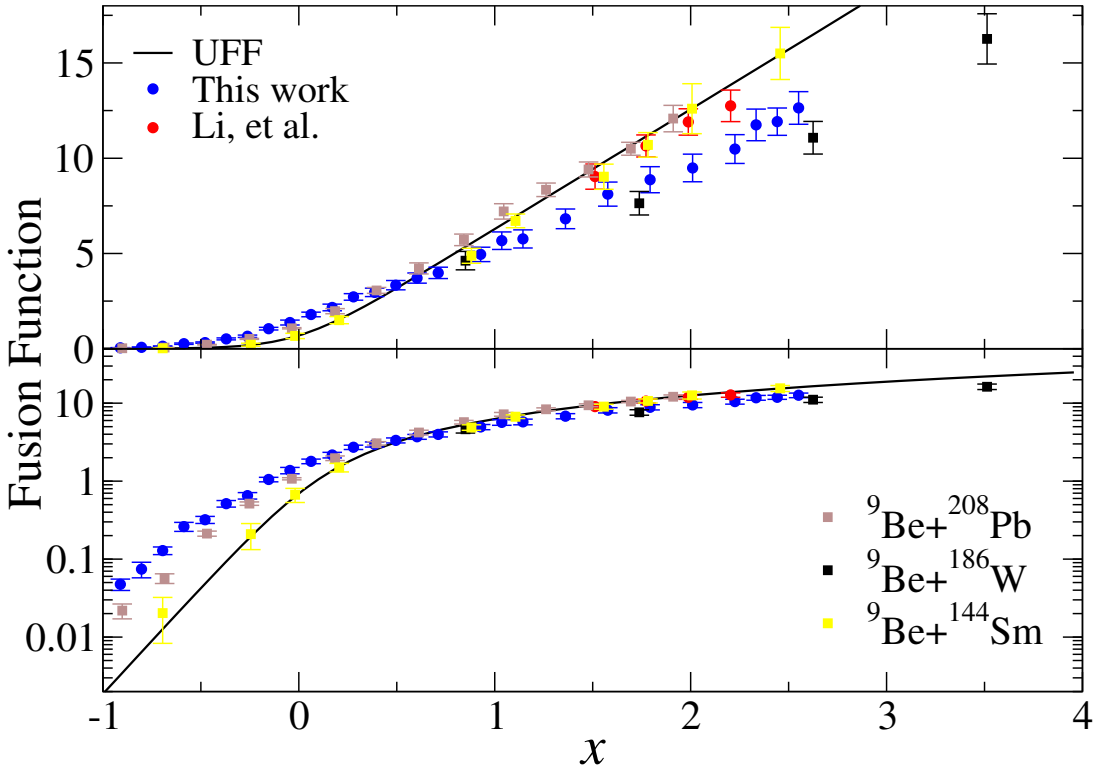

Figure 4.13: (Comparison between the UFF and renormalized fusion function for total fusion (TF). The systems are composed by the ^{9}Be projectile on different targets: ^{186}W [4], ^{144}Sm [5], ^{208}Pb [6], ^{197}Au from [7] and this work.

Chapter 5
Fusion process in neutron-rich mid-mass nuclei

An interesting process in nuclear reactions is fusion. When two strongly-interacting quantum systems merge, they lose their identity and assume a new one. Although the many-body correlations are key to understanding their intrinsic and collective nature, their impact on fusion is not yet fully understood. The influence of an unpaired neutron has been observed in the average fusion cross-section of neutron-rich carbon, and oxygen ions on carbon target [84, 85]. Yet it is important to observe the unpaired neutron in mid-mass and heavy nuclei. These neutron-rich nuclei with extended density distributions exhibit larger fusion cross-sections. The cross-section can be additionally increased by intrinsic and collective excitation. At small excitation, a coupled channel approach has successfully described the fusion of nuclei, as described in section 2.6. Despite the success of the coupled channel method, one might expect additional neutron dynamics to emerge for neutron-rich nuclei with loosely bound valence neutrons. Such dynamics can be theoretically probed through time-dependent approaches such as time-dependent Hartree-Fock [86] or density functional theory [87].

The simplest approach for calculating the fusion cross-section involves double folding the density distribution, assuming that the initial density distributions are frozen [88, 89]. The density distribution is not restricted to a one-body description but can include two-body or higher correlations allowing the nuclear structure to influence the fusion cross-section. Whether nuclear structure affects the fusion cross-section depends on whether they persist at the saddle point.

In the present work, we examine the fusion of the neutron-rich nuclei at the N=20, and N=28 closed shells as well as open-shell nuclei by studying the fusion of ^{39,41,45,47}K,^{36,44}Ar $+^{16}$O [56] and ^{39,41,45,47}K,^{36,44}Ar$+^{28}$Si [1]. The double closed-shell for ^{16}O provided a well-bound nucleus as the target enabling a systematic measurement of the impact of the projectile's shell structure on the fusion cross-section. The simplest description of fusion is through the interaction of the density distributions of the two interacting nuclei. If the interaction between the nuclei is non-adiabatic (i.e., described by the sudden approximation), it is sufficient to consider the ground-state density distributions. In the case of adiabatic collisions, collective modes in the colliding nuclei can be excited and need to be considered. Including these modes in a coupled channel (CC) formalism increases the fusion cross-section at energies near and below the Coulomb barrier [90–92]. To investigate whether the observed fusion excitation functions can be described by the interaction of the ground state density distributions of the projectile and target nuclei, the São Paulo model was used. The São Paulo potential was briefly described in Sub section.2.3.2. It is important to remember that the São Paulo potential (SPP) is the potential associated with matter densities described by a two-parameter

Fermi-Dirac(2pF) distribution with radius $R_0 = (1.31A^{1/3} - 0.81)$ fm and matter diffuseness $a = 0.56$ fm. This systematic was derived from the available experimental data for the charge distributions extracted from electron scattering and Dirac-Hartree Bogoliubov (DHB) calculations for many nuclei. As such, it provides a general description in which structural effects have been averaged over. Such potential has been used in many CC calculations, and their results successfully compare with experimental data [7, 46, 93, 94, 94].

Presented in Figs. 5.1 and 5.2 (dashed lines) are the predicted density distributions for the K and Ar isotopes, using the São Paulo potential systematic for matter densities, two-parameter Fermi (2pF) distribution. All these distributions have a smooth Fermi-Dirac shape with a central density of ≈0.16 nucleons/fm^3. These smooth distributions reflect, in essence, the one-body mean-field nature of the nuclei considered and do not manifest nuclear structure associated with two-body correlations.

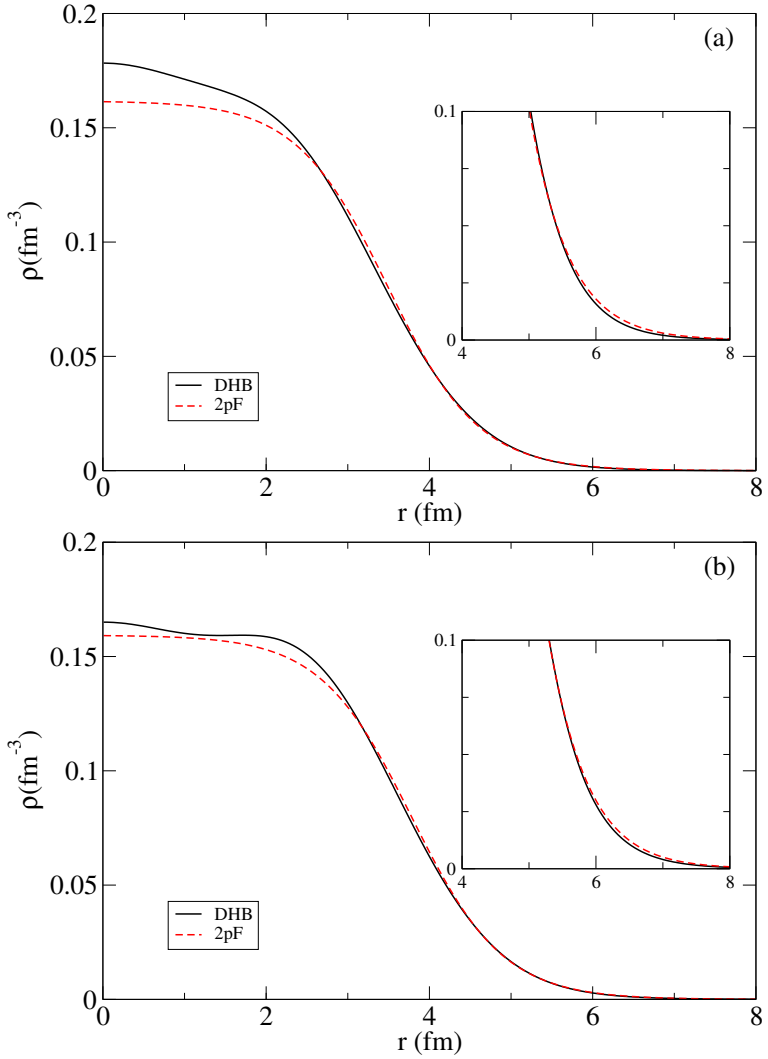

Figure 5.1: Comparison of the matter density distributions for the (a) ^{36}Ar, and (b) ^{44}Ar isotopes given by the systematics that is typically used within the São-Paulo fusion model (2pF) with the density distributions predicted by Dirac Hartree Bogoliubov (DHB) calculations. Shown in the insets are the tails of the matter distributions.

To calculate more accurate matter density distributions, which include two-body correlations, Dirac-Hartree-Bogoliubov (DHB) calculations [95] were performed and available in the new version of the SPP called Regina [96]. The details of these mean-field calculations using an axially-symmetric self-consistent approximation are reported in Ref. [96]. The resulting matter distributions are shown in Figs. 5.1 and 5.2 as the solid lines. Evident in the DHB matter distributions is a double-humped structure, a manifestation of the shell structure. For ^{39}K, the dominant peak is located at lower values of R. With increasing neutron number, the density of this inner peak decreases until at ^{47}K, the outer peak is the dominant peak in density. A similar trend is observed between ^{36}Ar and ^{44}Ar, although the inner peak is larger for these nuclei. As the fusion of two nuclei is typically viewed as sensitive to the tails of the matter distribution, an expanded view of this region is shown in the insets of Figs. 5.1 and 5.2. Notably, the tails of the matter distributions are quite similar, although the DHB distributions are *slightly* less extended than the systematics.

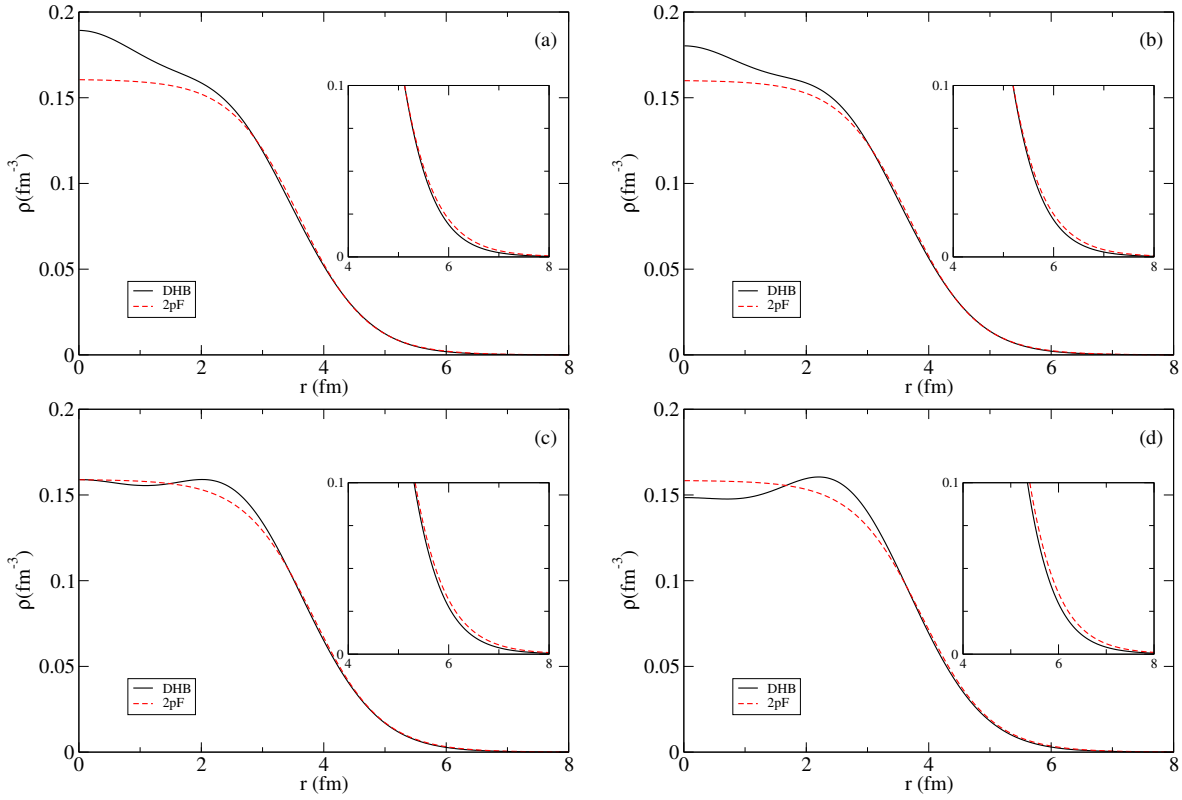

Figure 5.2: Comparison of the matter density distributions for the (a) ^{39}K, (b) ^{41}K, (c) ^{45}K, and (d) ^{47}K isotopes given by the systematics that is typically used within the São-Paulo fusion model (2pF) with the density distributions predicted by Dirac Hartree Bogoliubov (DHB) calculations. Shown in the insets are the tails of the matter distributions.

Displayed in Figs. 5.3 and 5.4 are the proton and neutron density distributions predicted by the DHB model. One observes that adding neutrons to ^{39}K influences the neutron and significantly impacts the proton density distribution. As the peak in neutron density situated at large R increases in magnitude, the proton peak at large R also increases in magnitude. As the total number of protons is constant, this increase is correlated with a decrease in the value of the central proton density. This outward displacement

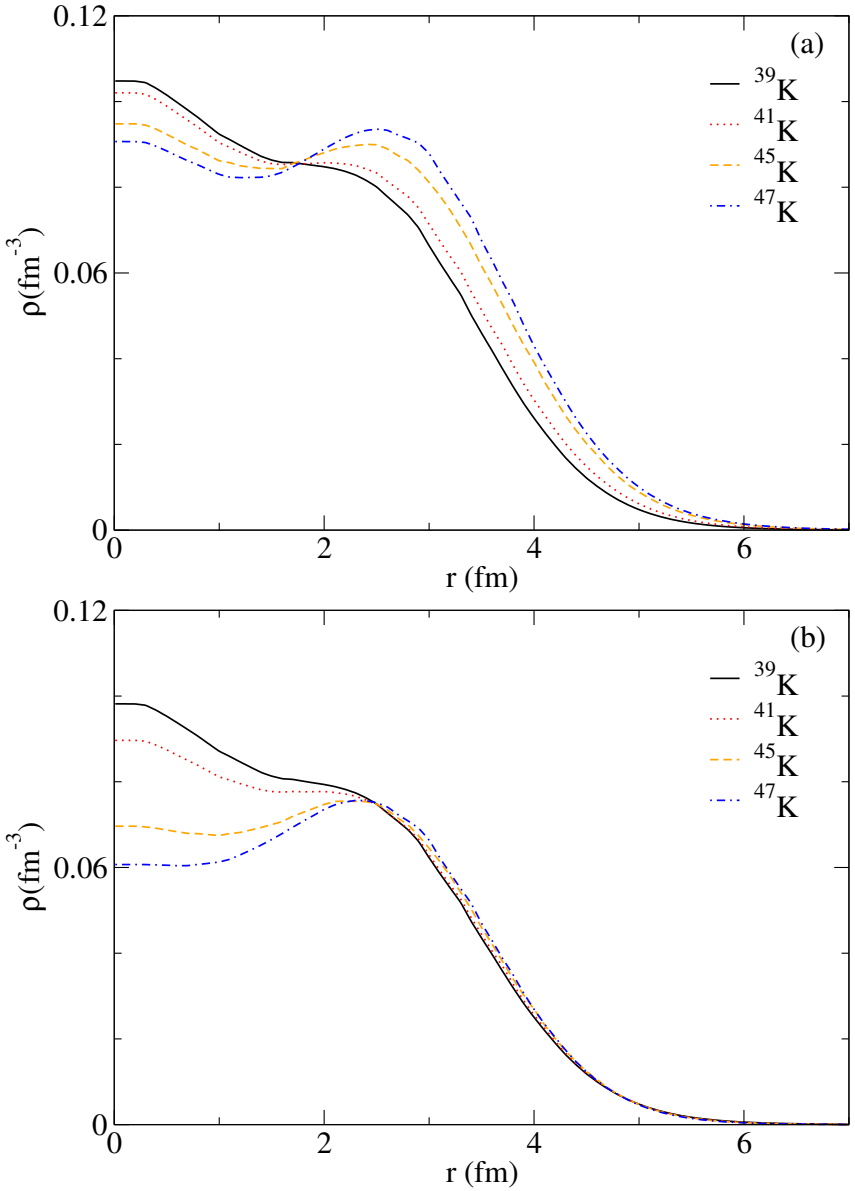

Figure 5.3: Density distributions of neutrons (a) and protons (b) for K isotopes predicted by the DHB calculations.

of the proton density by additional neutrons can be thought of as the resistance of nuclei to the polarization of the ground state. This behavior has previously been noted in relativistic mean field calculations for neutron-rich oxygen isotopes and reflects the n-p interaction via the strong force [56]. Close examination of this outward pull of the valence neutrons on the core (N$\leq$20) neutrons as compared to the core protons reveals that the protons experience a larger outward pull. Due to the Pauli exclusion principle, this difference can be interpreted as repulsion between the valence neutrons and the core neutrons. Similar behavior is also observed for the argonium isotopes.

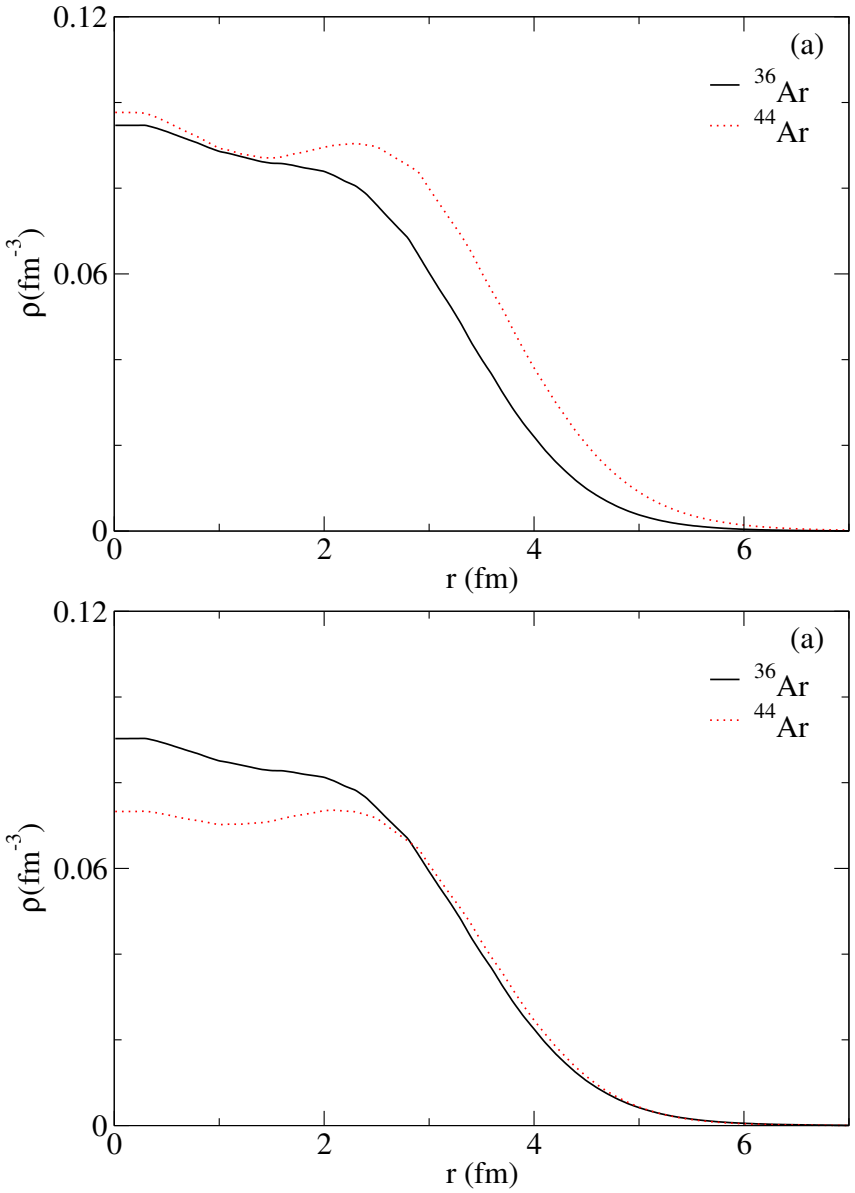

Figure 5.4: Density distributions of neutrons (a) and protons (b) for Ar isotopes predicted by the DHB calculations.

5.1 Reactions with ^{16}O target

Using the DHB matter distributions for the projectile and ^{16}O target nuclei, the São Paulo Potential was generated and used to calculate the fusion cross-section. The theoretical predictions from one-channel calculations, using a short-range Woods-Saxson imaginary potential, are compared with the experimental data in Figs. [5.5-5.10]. In addition to the cross-sections resulting from the DHB matter densities (solid lines), the cross sections associated with the systematics densities are also shown (dashed lines). In all cases, the use of the DHB densities results in a significant reduction of the fusion cross-section as compared to the systematics. This reduction is apparent over the entire energy interval considered. As the tail of the density distribution is essentially the same for both the DHB and systematics, one can conclude that the change in the cross-section is due to the difference in the interior part of the density distribution.

A comparison of the theoretical predictions with the experimental excitation functions is revealing. For the open neutron shell isotopes ^{41,45}K, the theoretical model with the DHB densities provides a reasonable prediction of the excitation function, particularly for the lower energies. However, in the case of the closed neutron shell ^{47}K, particularly for ^{39}K, the model overpredicts the measured cross-sections. This overprediction for the case of the closed-shell nuclei might suggest that the ground-state configurations at the saddle point that result in fusion are more compact than the ground-state DHB calculations indicate. Alternatively, it might signal that higher-order correlations not present in the DHB calculations are more important for these neutron closed-shell nuclei. In the case of the ^{36,44}Ar nuclei, the agreement is intermediate between the open-shell and closed-shell K isotopes.

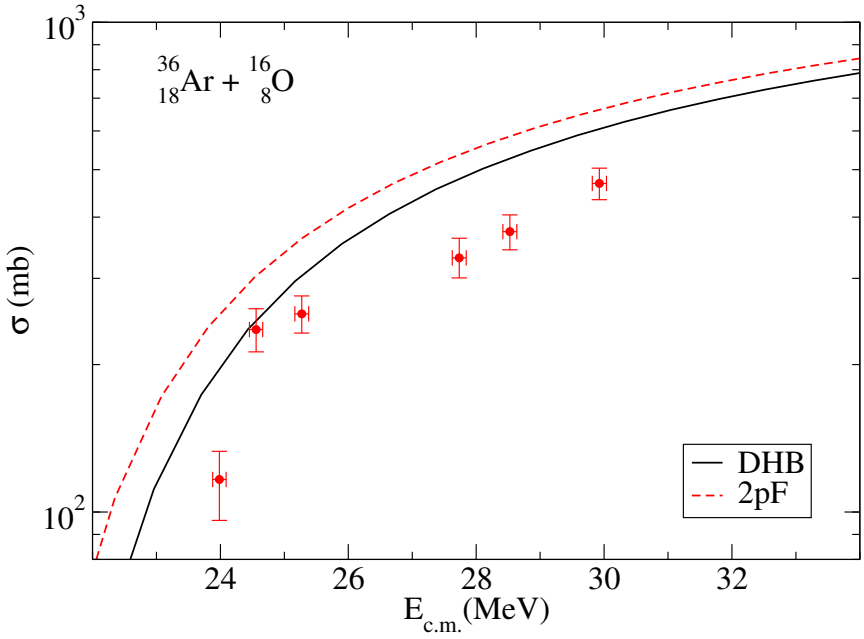

Figure 5.5: Comparison of the experimental cross-sections with the predictions of the São Paulo model using DHB densities and densities from systematics.

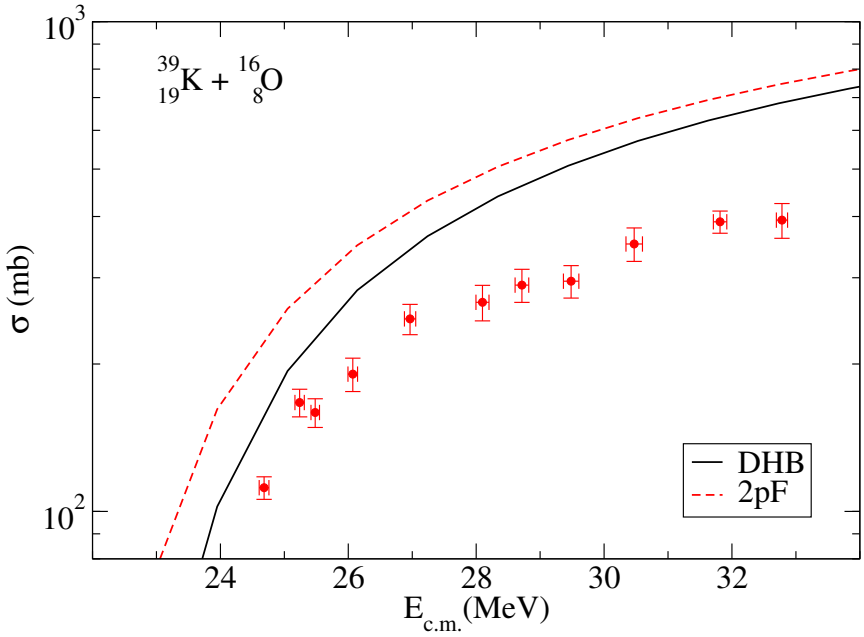

Figure 5.6: Comparison of the experimental cross-sections with the predictions of the São Paulo model using DHB densities and densities from systematics.

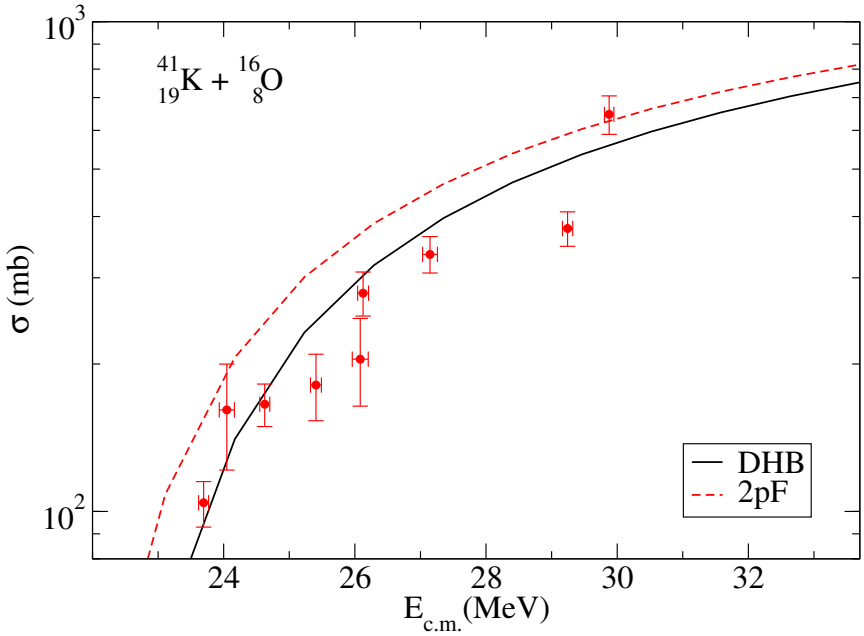

Figure 5.7: Comparison of the experimental cross-sections with the predictions of the São Paulo model using DHB densities and densities from systematics.

The fact that the fusion cross section derived using the São-Paulo with DHB densities is also significant. Coupling to low-lying collective modes acts to increase the fusion cross-section. Given that the ground state calculation already overpredicts the measured cross-section, the excitation of low-lying collective modes can be ruled out. The largest discrepancy is observed for the closed neutron shells at N=20 and N=28. Presumably, these closed-shell nuclei are the least likely to undergo collective excitations. The persistence of shell effects at the saddle point also indicates that, as expected, the intrinsic

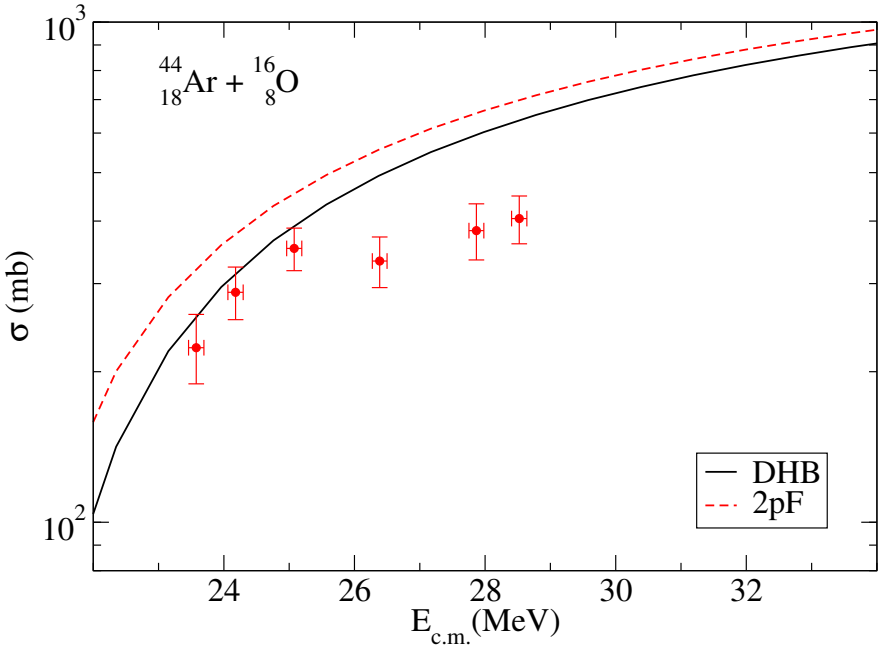

Figure 5.8: Comparison of the experimental cross-sections with the predictions of the São Paulo model using DHB densities and densities from systematics.

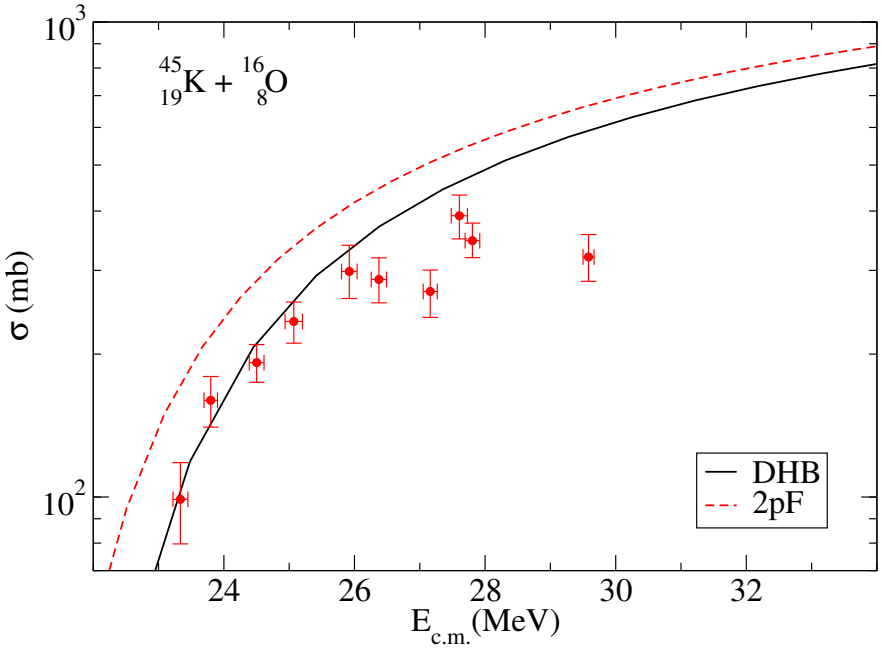

Figure 5.9: Comparison of the experimental cross-sections with the predictions of the São Paulo model using DHB densities and densities from systematics.

excitation of the saddle configuration is not large, as any significant excitation would overwhelm the shell effects.

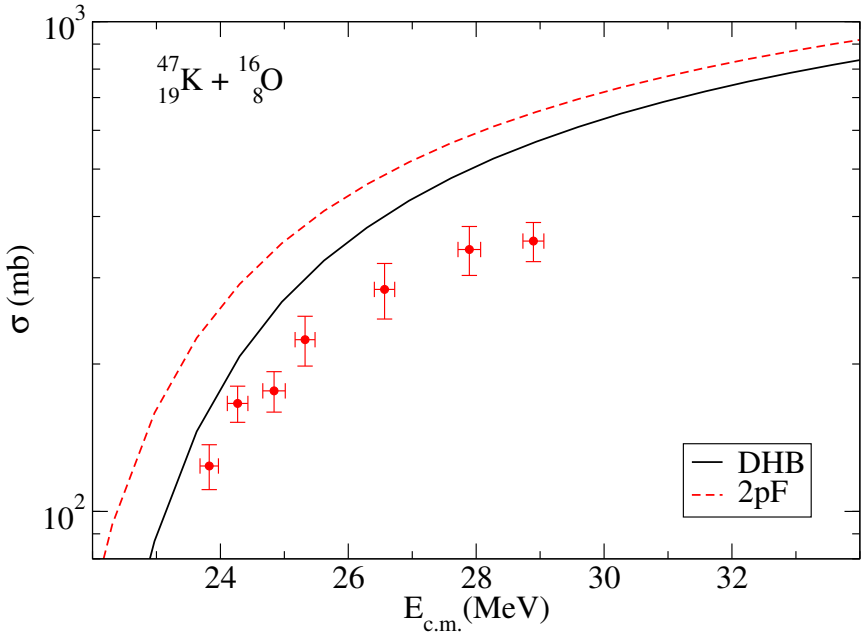

Figure 5.10: Comparison of the experimental cross-sections with the predictions of the São Paulo model using DHB densities and densities from systematics.

5.2 Reaction with ^{28}Si target

The SPP was generated to calculate the fusion cross section using the ground-state DHB matter distributions for the projectile and ^{28}Si target nuclei. The theoretical predictions, represented by the solid black lines, are compared with the experimental data in Figs. [5.11-5.16]. Comparison of this one-channel (DHB-OC) theoretical predictions with the experimental excitation functions is revealing. Compared with the 2pF-OC curves (red dashed lines), the result is similar to those for ^{16}O target. However, in this case, the theory distances from the data. For the closed neutron shell isotopes ^{39,47}K (see Figs. 5.12 and 5.16), the DHB-OC calculations provide a reasonable prediction of the excitation function over the entire energy interval measured although the model calculations lie slightly below the experimental data, particularly in the sub-barrier regime. In the case of the open neutron shell ^{41}K (Fig.5.13), ^{45}K (Fig.5.15), and ^{36}Ar (Fig.5.11), the model dramatically underpredicts the measured cross sections, particularly at sub-barrier energies. This underprediction for the case of the open-shell nuclei suggests that the ground-state configurations alone are insufficient in describing the measured cross sections. In the case of ^{44}Ar, (Fig.5.14) insufficient data exists at low energy to draw a definitive conclusion.

As coupling to low-lying collective modes increases the fusion cross section at energy below the barrier, we have performed CC calculations to investigate how much the presence of low-lying states increases the fusion cross section. The 1.779 MeV, 2^+ and 4.618 MeV, 4^+ first states of the target were considered. The coupling to the low-lying projectiles states does not considerably affect the fusion cross section. To account for the couplings between the low-lying states, the transition probabilities were taken from Ref. [97].

The results of the CC calculations are shown in Figs. [5.11-5.16] as blue point

Table 5.1: Q values (in MeV) for one- and two-neutron transfer.

Q	^{39}K	^{41}K	^{45}K	^{45}K
1n	-4.604	-1.621	-0.432	0.105
2n	-6.068	1.187	2.899	3.843

dashed lines. In the case of the closed-shell nuclei, ^{39}K and ^{47}K, the inclusion of the excitations considered provides a good description of the fusion cross section. However, in the case of the open-shell nuclei, the experimental data are significantly enhanced relative to the CC calculations, including low-lying excitations. It is particularly interesting to note that the magnitude of the enhancement is much larger than the increase due to the inclusion of inelastic excitation in the CC calculations. This enhancement suggests that transfer might occur before fusion.

Neutron transfer before fusion is often proposed as responsible for an enhancement in the fusion cross section [90, 98, 99]. For a system with zero Q-value for two neutron transfers, ^{60}Ni+^{58}Ni, inelastic excitations dominate, and neutron transfer plays a negligible role [100]. When one of the colliding nuclei is neutron-rich relative to its collision partner, as in the case of ^{44}Ca+^{96}Zr, positive Q-values might be possible, and the sub-barrier fusion is enhanced when compared with the ^{40}Ca+^{90}Zr reaction [101–104]. It is important to state that the Q-value is one of the ingredients to observe the fusion enhancement below the barrier. The other ingredient is the deformation of the nuclei after the nucleon(s) is(are) transferred. If the deformation of the residual nuclei is higher than the initials, the barrier is lowered, and the fusion is enhanced.

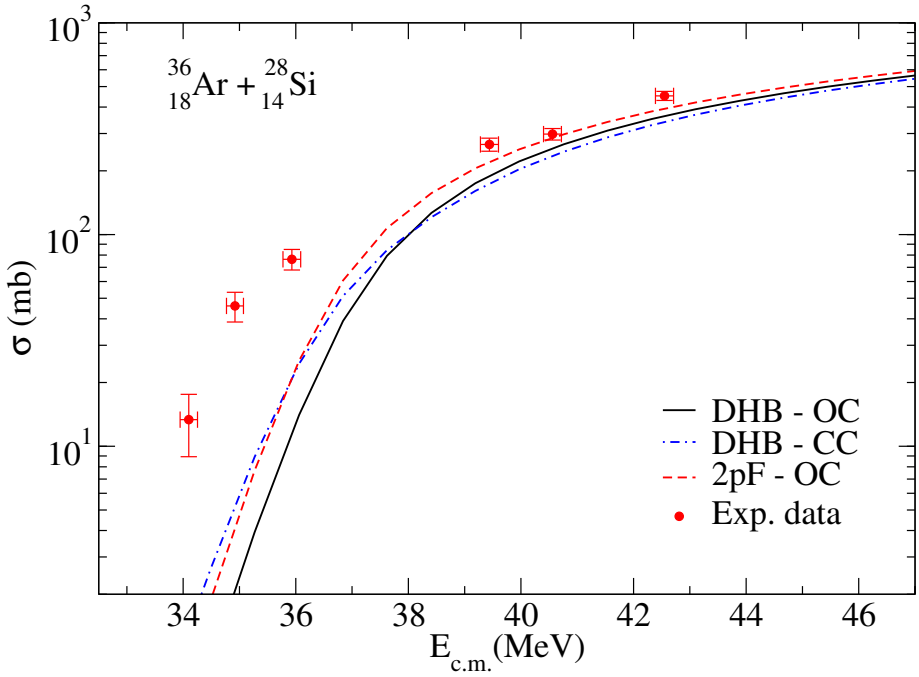

Figure 5.11: Comparison of the experimental cross-sections with the predictions of the São Paulo model using DHB densities for one channel and coupled channel as well as densities from systematics for ^{36}Ar projectile.

The relevant Q-values for the reactions studied in this work are presented in Table 5.1. Except for ^{39}K, the Q-value for two-neutron transfer in the other K isotopes is positive. Transfer of one neutron from ^{39}K to ^{28}Si is -4.604 MeV, while from ^{47}K is slightly positive (+0.1 MeV). Nonetheless, the fusion excitation function for neutron transfer for the open-shell cases ^{41,45}K lies between that of ^{39}K and ^{47}K. Yet, the fusion excitation functions of the open-shell cases differ from those of the closed shell. The observed behavior of the experimental fusion excitation functions cannot be understood simply by considering the Q-value for neutron transfer.

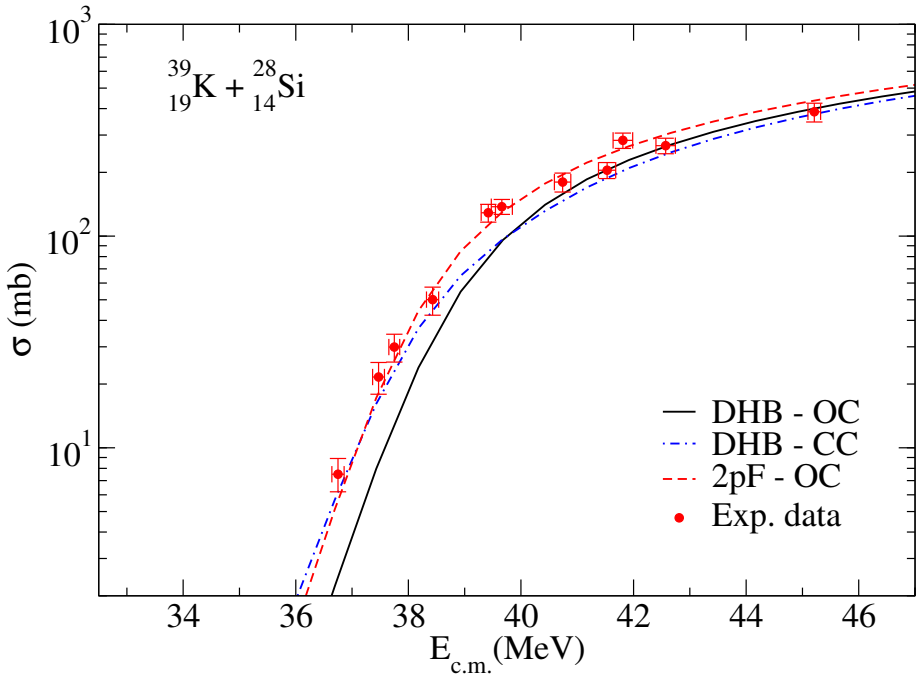

Figure 5.12: Comparison of the experimental cross-sections with the predictions of the São Paulo model using DHB densities for one channel and coupled channel as well as densities from systematics for ^{39}K projectile.

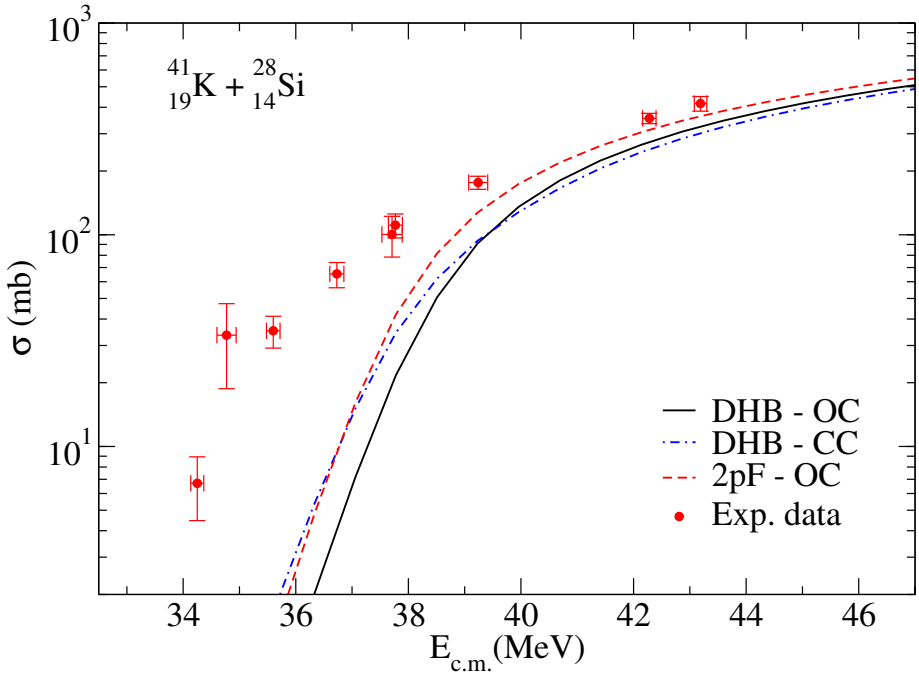

Figure 5.13: Comparison of the experimental cross-sections with the predictions of the São Paulo model using DHB densities for one channel and coupled channel as well as densities from systematics for ^{41}K projectile.

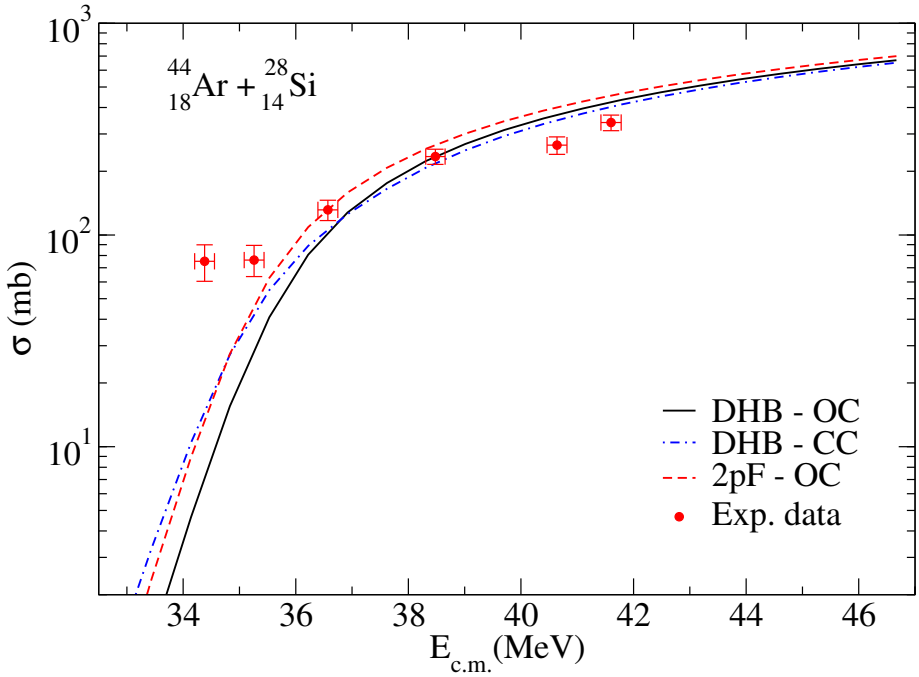

Figure 5.14: Comparison of the experimental cross-sections with the predictions of the São Paulo model using DHB densities for one channel and coupled channel as well as densities from systematics for ^{44}Ar projectile.

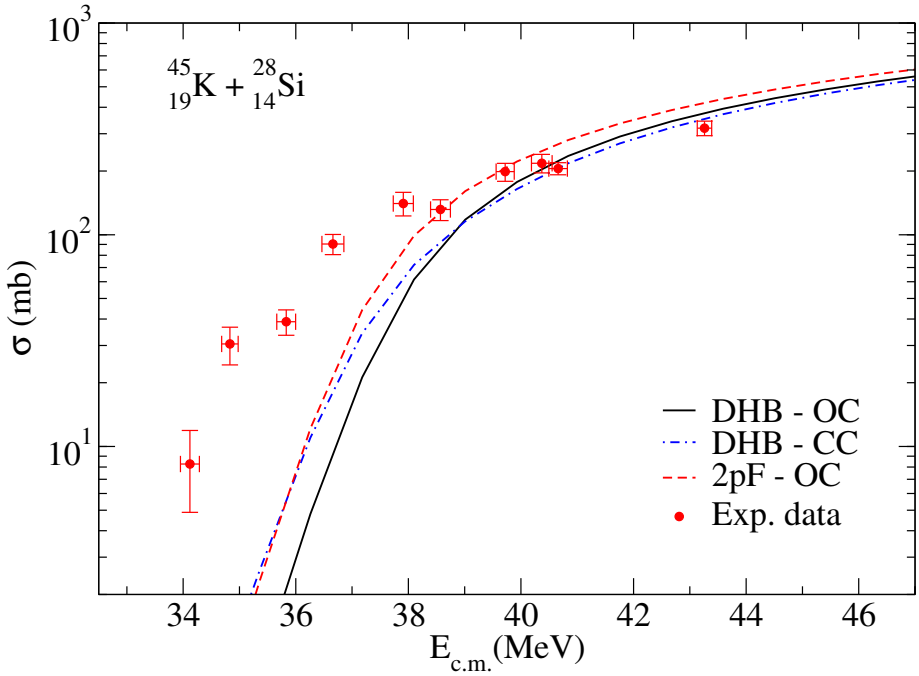

Figure 5.15: Comparison of the experimental cross-sections with the predictions of the São Paulo model using DHB densities for one channel and coupled channel as well as densities from systematics for ^{45}K projectile.

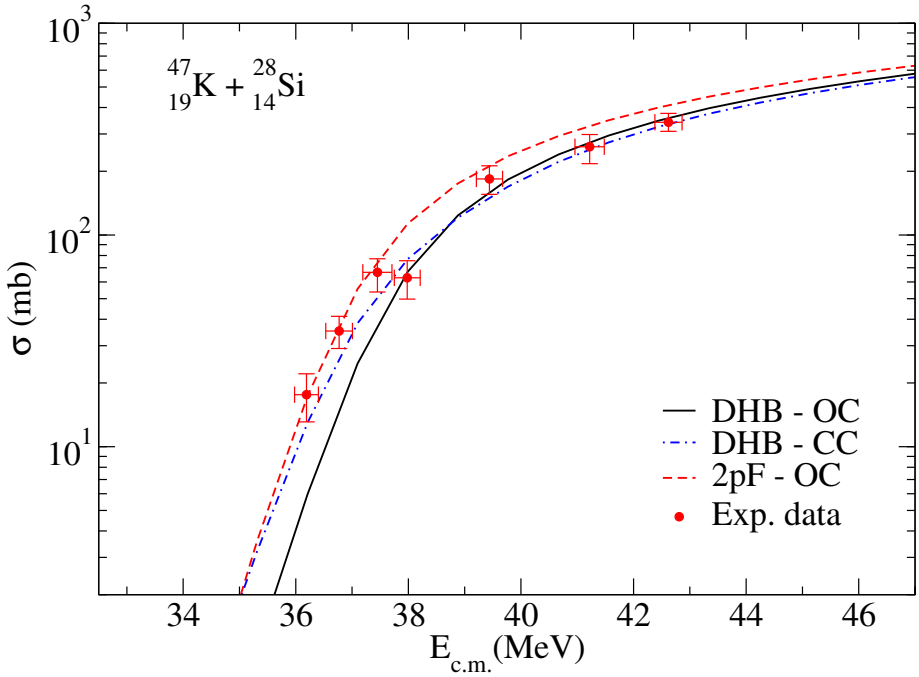

Figure 5.16: Comparison of the experimental cross-sections with the predictions of the São Paulo model using DHB densities for one channel and coupled channel as well as densities from systematics for ^{47}K projectile.

Chapter 6
Four-body treatment of ^{6}He projectile in reactions with heavy targets

Due to the effect of the breakup channel on the nuclear reactions, interactions involving weakly-bound, exotic and stable, and radioactive nuclei such as ^{6,8}He [20, 21, 105, 106], ^{6,7,8,11}Li [6,22,23,107], ^{7,9}Be [5–7,24–26,80,107], ^{8}B [27,34,107–110], and ^{17}F [67,111] have been investigated extensively in the last years. The fusion cross section, non-capture direct breakup, inelastic and transfer channels, and total reaction are examples of reaction channels that could be sensible to the breakup [46, 94, 112–115]. Some methods are developed to study these types of reactions. One of them is the Universal Fusion Function method that accounts for static effects to study the dynamic effect of the breakup channels on fusion cross sections for different systems [65, 66]. Another very successful method to study the breakup mechanism is the continuum-discretized coupled channel (CDCC) theoretical approach that explicitly considers the breakup channel. The CDCC method has been extensively used for three-body reactions (two-body projectile plus a target), mainly applying the binning method [18, 19] to discretize the continuum energy of the projectile. This method was successfully used in some systems with a two-body weakly-bound structure [28–38]. However, some nuclei present a Borromean structure composed of a three-body bound system in which any subsystem of two fragments is unbound. In these cases, the three-body CDCC formalism has been applied considering simplified schemes such as the dineutron model [47, 48, 116–118].

An appropriate description of Borromean nuclei needs a three-body description for the projectile, applying the four-body CDCC formalism. The reactions induced by the Borromean nucleus ^{6}He have been extensively described by four-body CDCC calculations [40–42, 119–122]. The reason is that the projectile is composed of a ^{4}He core and two valence neutrons. The three-body CDCC method has also been used to describe ^{6}He reactions, considering the ^{4}He core and a di-neutron [47, 48]. Some unphysical results can be derived from this approach. The transition probabilities are larger than the experimental values, the root mean square radius is overestimated, and the enhancement of the dipole couplings to the continuum is obtained. Nevertheless, it was possible to find a good agreement with the experimental data for the elastic cross-section within the three-body CDCC approach by increasing artificially the binding energy of the two-neutron to the core [120]. This takes into account, effectively, the interaction between two neutrons and provides the correct root-means-square radius to the nucleus. Nonetheless, to have a more accurate and realistic treatment for the interaction of a three body-projectile with a target, a more realistic theoretical model is mandatory.

The four-body CDCC formalism was first developed using the pseudo-state method [39–41, 122–124]. However, for reactions on heavy targets and at energies around the Coulomb barrier, convergence problems appear, and a more precise description of the low

continuum spectrum is mandatory. To solve this issue the four-body CDCC formalism using the binning procedure for three-body projectiles was presented in Ref. [42]. This procedure used the hyperspherical coordinates, making necessary the truncation in the number of hyperspherical momentum K, that will determine the maximum relative orbital angular momenta, between the fragments, included in the calculation. The convergence with respect to the maximum hypermomentum must be studied since it can generate inaccurate results for some observables. This chapter attempts to obtain some observables using four-body CDCC calculations and compare them with available experimental data. Although, it is necessary to address the inaccuracies that might appear by truncating the size of the hyper-momentum space considered in the four-body CDCC calculations.

6.1 Three-body description of ^{6}He

In this work, we model the ^{6}He projectile as a three-body system comprising an inert alpha particle plus two valence neutrons. This system has a single bound state with respect to the $\alpha + n + n$ threshold, with a binding energy of $\varepsilon_{\rm b} = 0.973$ MeV and total angular momentum $J^\pi = 0^+$. It is also known experimentally the existence of a narrow resonance with total angular momentum $J^\pi = 2^+$ at 1.797 MeV over the ground state, with a width of 0.113 MeV [125]. Two-body interactions from Refs. [126] plus an effective three-body force, depending on the hyperradius, are included to reproduce the ^{6}He structure. The three-body force is introduced to reproduce the experimental energies for the ground and resonant states. The matter radius, $r_{\rm matter}$, and the resonant width are also reproduced. The fit of the three-body potential parameters needs to be performed for each value of the maximum hyper-momentum used, $K_{\rm max}$, as we can see from Table 6.1. The three-body potential has the form

$$V_{\rm 3b}(r) = \frac{s_{\rm 3b}}{1 + (r/r_{\rm 3b})^{a_{\rm 3b}}}, \tag{6.1}$$

where $S_{\rm 3b}$ is the strength of the interaction, $r_{\rm 3b}$ is the radius where the potential has half depth, and $a_{\rm 3b}$ is connected to the speed that the potential goes to zero at the infinity. We set $a_{\rm 3b} = 3.00$ in this work. The three-body potential parameters are usually fitted to describe the experimental binding energy and root-mean-square (RMS) matter radius of the ^{6}He nucleus. In our case, the calculated binding energy is 0.953 MeV (0.975 MeV), and the RMS matter radius is 2.46 fm (2.48 $\pm$ 0.03 fm), assuming an α-particle RMS radius of 1.47 fm (1.47 fm). In parenthesis are reported the experimental values taken from Ref. [127]. One observes quite good agreement among them. The calculations were performed using FACE [128] plus STURMXX [129] codes.

$\mathbf{K_{max}}$	**8**	**10**	**12**	**14**	**16**	**18**
$s_{\rm 3b}$(MeV)	-3.050	-3.700	-4.290	-6.557	-6.363	-6.197
$r_{\rm 3b}$(fm)	5.00	4.00	3.50	2.70	2.70	2.71
$\varepsilon_{\rm b}$(MeV)	0.953	0.953	0.953	0.953	0.953	0.953
$r_{\rm matter}$(fm)	2.463	2.464	2.466	2.449	2.466	2.471

Table 6.1: Adjusted parameters for each $K_{\rm max}$.

First, we will study the convergence of the structure observables with respect to the maximum hypermomentum. One important structure observable is the transition

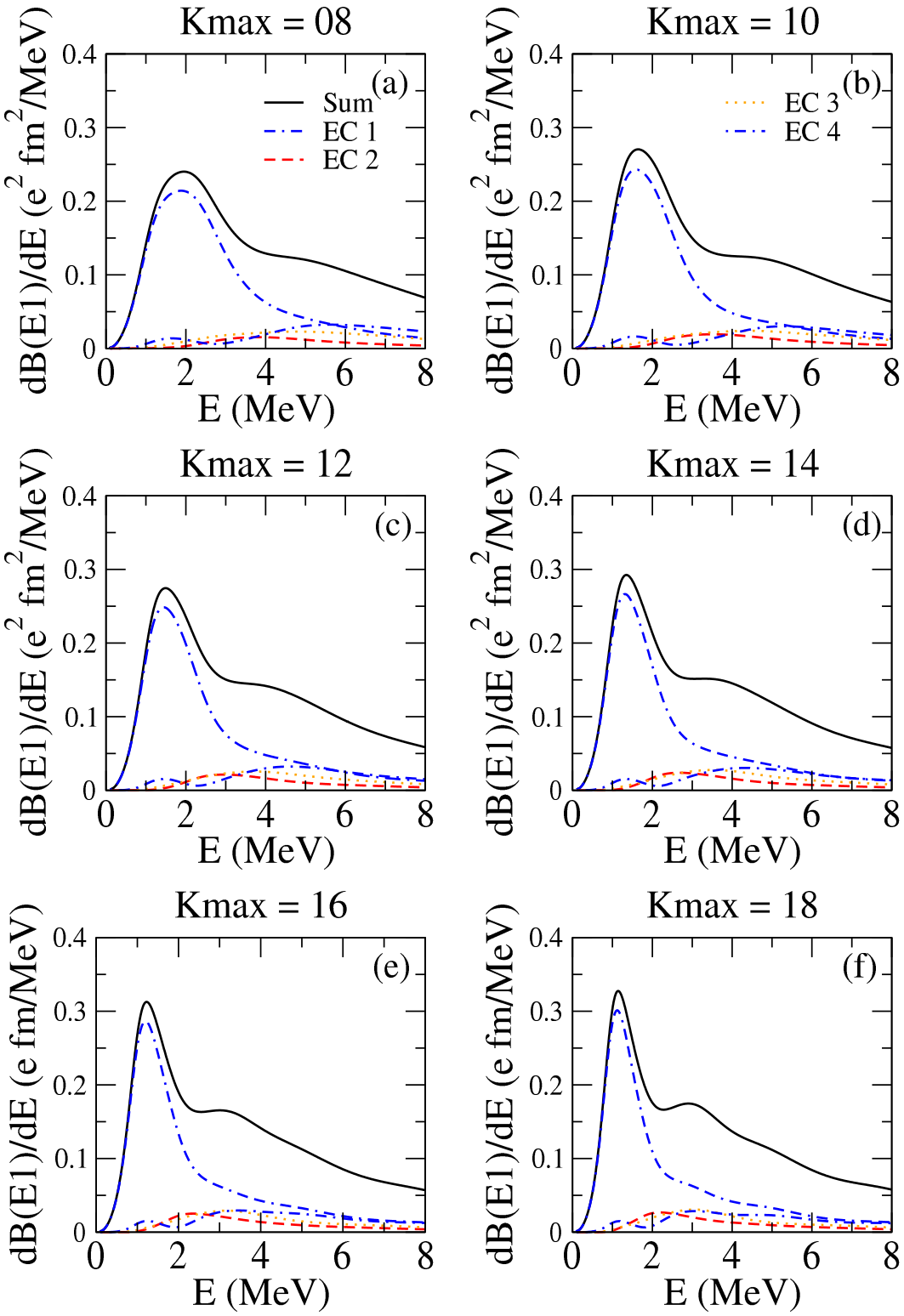

Figure 6.1: B(E1) distribution for each $K_{\max}$, for the first few $J^{\pi} = 1^{-}$. The black solid line is the sum of all eigenchannel (EC). The ECs that most contribute to the dipole response are enumerated from 1 to 4 using different lines.

probabilities, $B(E\lambda)$, given in detail in subsection. 2.4. In this way, Figs. 6.1 and 6.2 show, respectively, the energy distributions for the electric transition probabilities $B(E1)$ and $B(E2)$ for some values of $K_{\max}$, versus the excitation energy above the breakup

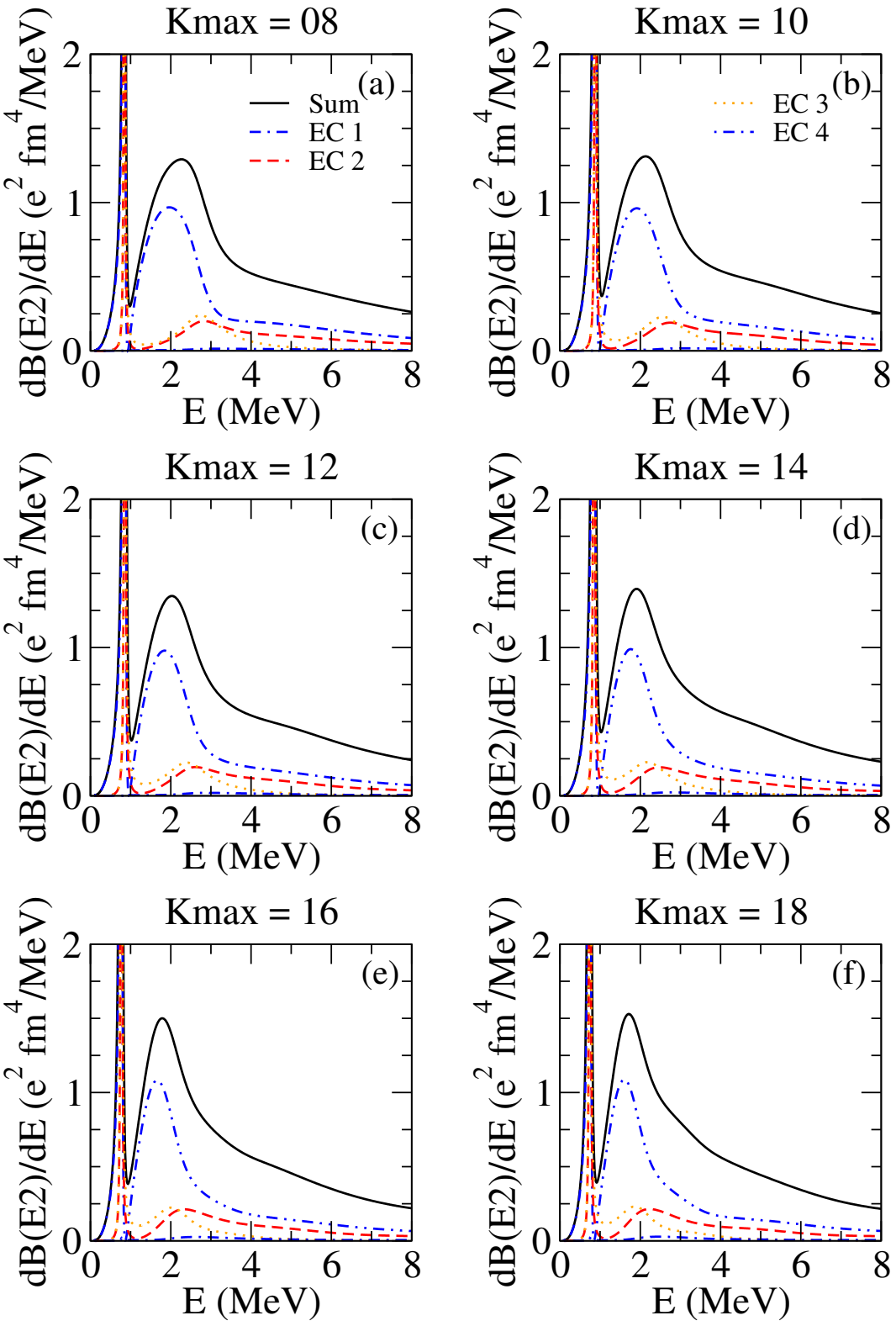

Figure 6.2: B(E2) distribution for each $K_{\max}$, for the first few $J^{\pi} = 2^{+}$. The black solid line is the sum of all eigenchannel (EC). The EC that most contribute to the quadrupole response are enumerated from 1 to 4 using different lines

threshold. It is noticed that the transition probabilities vary when $K_{\max}$ is increased. The difference is about 800 keV between the position of the $B(E1)$ peaks for $K_{\max} = 8$ and

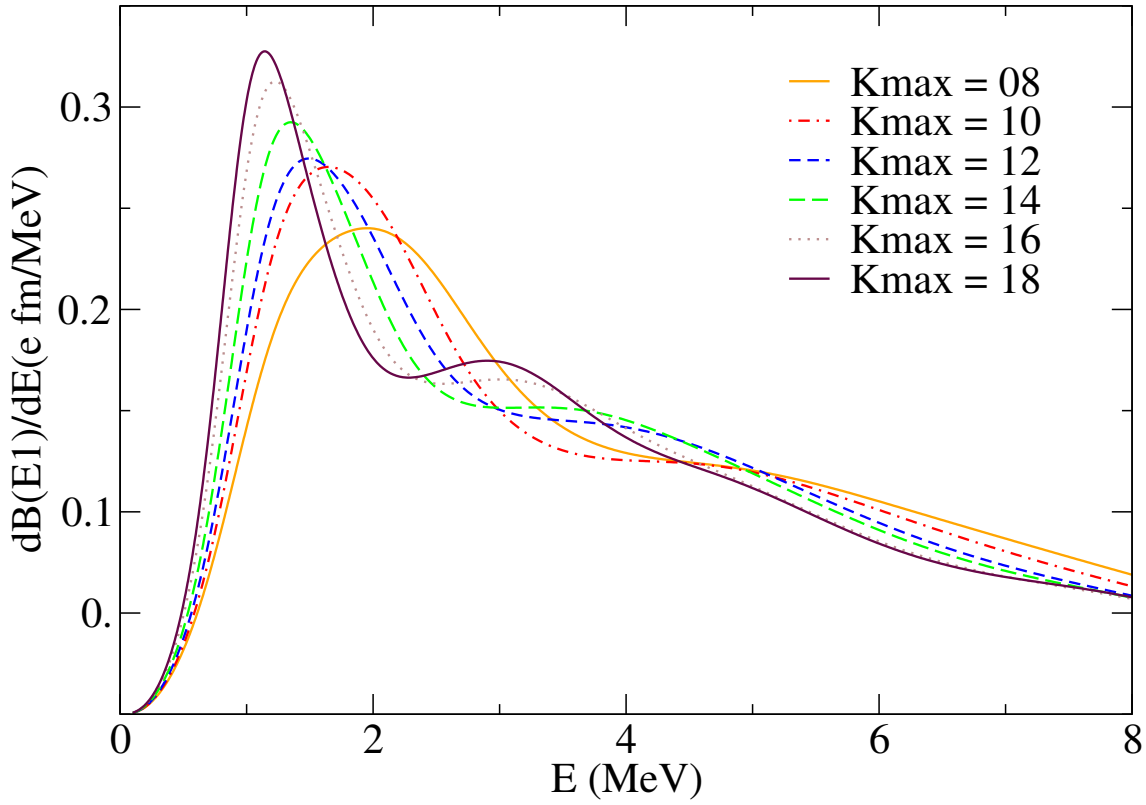

Figure 6.3: $J^\pi = 1^-$ B(E1) distribution for each $K_{\max}$.

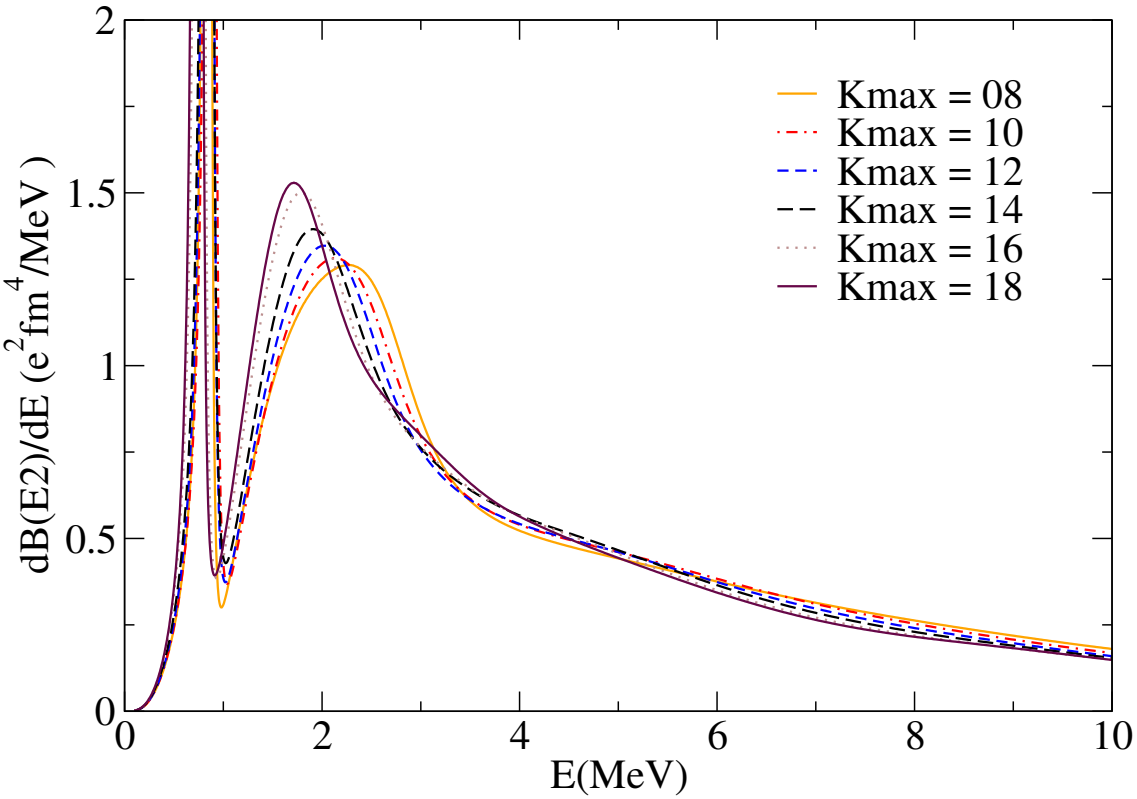

Figure 6.4: $J^\pi = 2^+$ B(E2) distribution for each $K_{\max}$.

$K_{\max} = 18$ (see Fig. 6.1). We would like to remark that the comparison to $K_{\max} = 8$

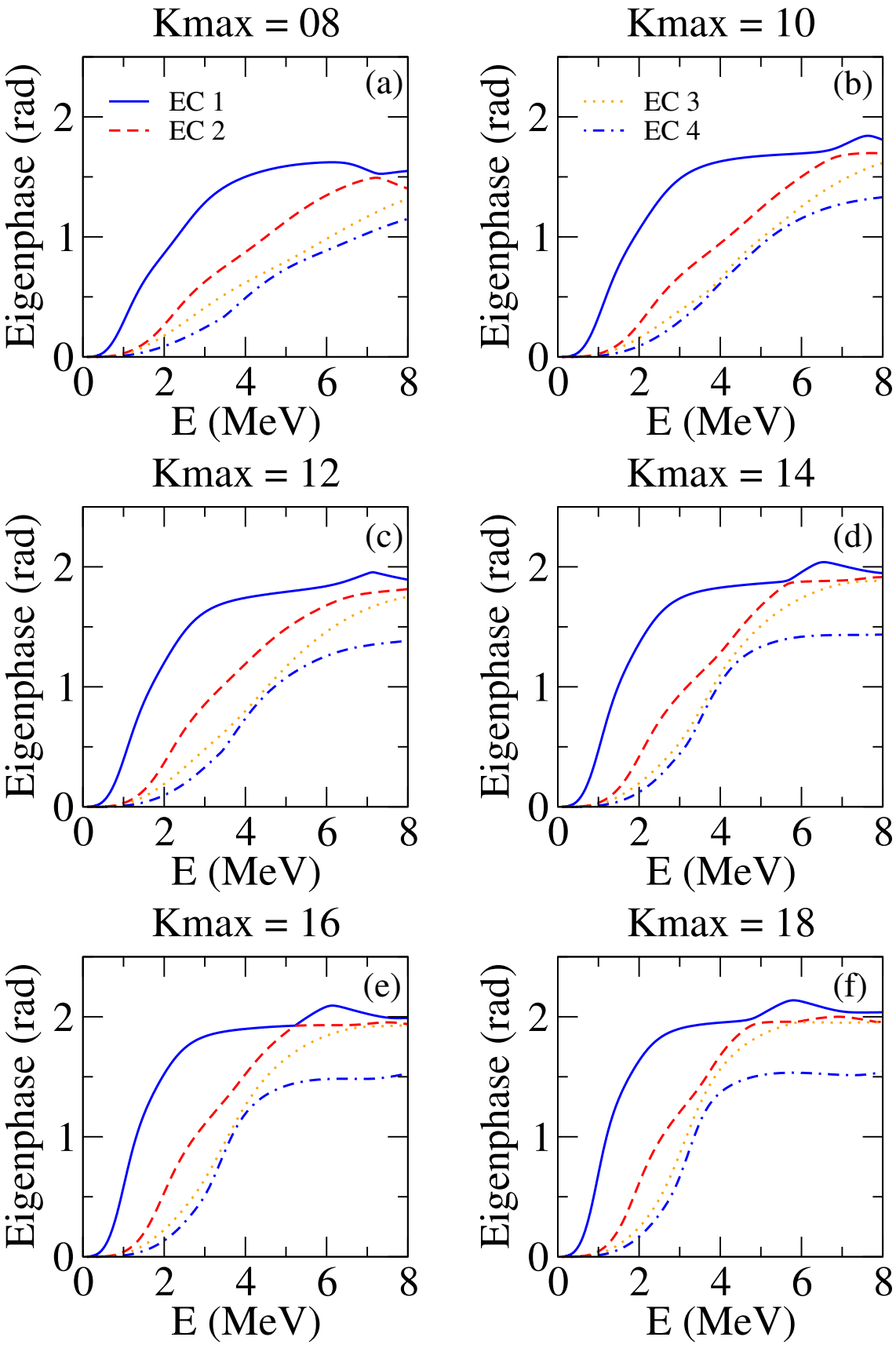

Figure 6.5: Eigenphase shift for each $K_{\max}$, for the first few $J^{\pi} = 1^{-}$.

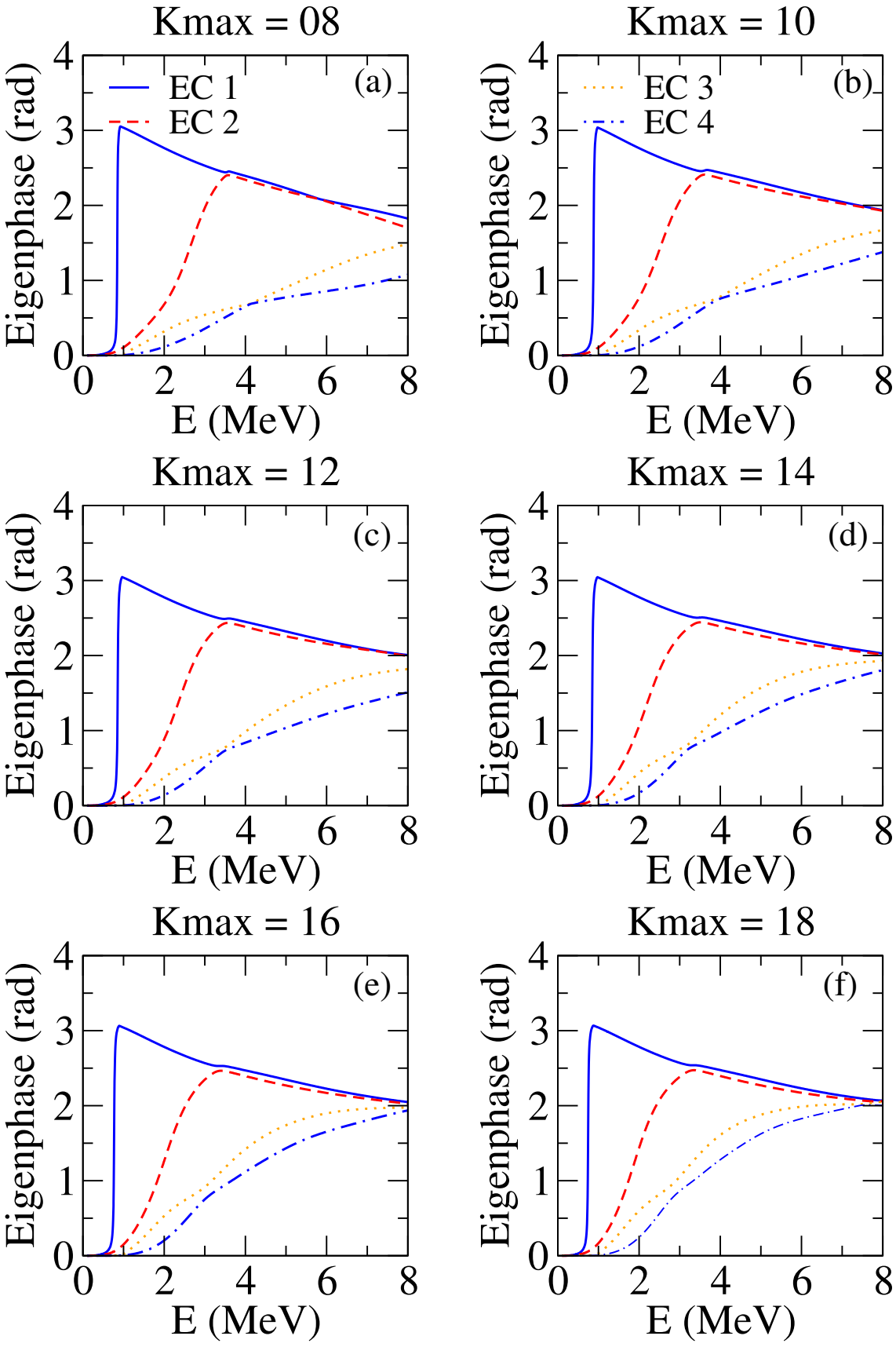

Figure 6.6: Eigenphase shift distribution for each $K_{\max}$, for the first few $J^{\pi} = 2^{+}$.

is because it was the maximum value needed to describe the elastic scattering angular distributions for the ^{6}He + ^{208}Pb reaction in Ref. [42]. However, the variation of peak positions is not very significant for two adjacent values of $K_{\max}$. The $B(E2)$ probability also depends on the hyper momentum value (see Fig. 6.2). The difference between the peak positions is about 500 keV in the same interval of $K_{\max}$ considered. Of course, the position of the 2^+ resonance remains in the right place. In both cases, it is observed that the mentioned peaks become narrower, and higher and are shifted to lower energies as the $K_{\max}$ was increased. This is better observed in Figs. 6.3 and 6.4, where dipole and quadrupole transition probabilities are shown in the same plot for different values of $K_{\max}$ considered. Although this shows that the convergence of the transition probabilities was not achieved, in Ref. [41], it was argued that $K_{\max} = 8$ is enough to guarantee the convergence of the scattering observables. In fact, in that paper, the authors studied the elastic scattering angular distribution. As shown below, $K_{\max} = 8$ was enough to guarantee the convergence of this observable. The eigenphases for the 1^- and 2^+ states are shown in Figs. 6.5 and 6.6, respectively. It is observed that the eigenphases vary slowly in the range of the maximum hyper-momentum analyzed. The eigenphases are converged for the 2^+ states (see Fig. 6.6). On the other hand, there is not a clear convergence for the 1^- states (see Fig. 6.5). This is additional evidence that the total convergence was not achieved at $K_{\max} = 8$. Comparing Figs 6.5 to 6.1 and 6.6 to 6.2, one can confirm, as expected, that the larger is the phase shift, the bigger the B(Eλ).

6.1.1 ^{6}He+^{208}Pb

We start by studying the ^{6}He+^{208}Pb system. To disentangle the impact of the maximum hypermomentum considered on the scattering observables, the Fresco code [130] was used to solve the set of coupled equations (Eq. 3.14). Like in Ref. [42], the solution includes J = 150$\hbar$ partial waves, assuming they reach the asymptotic form at the radius $R_{\text{match}} = 200$ fm, for 22 MeV ^{6}He projectiles impinging on ^{208}Pb. The number of bins was 12 for $J^\pi = 0^+$, 15 for $J^\pi = 1^-$, and 12 for $J^\pi = 2^+$ states. Bins with angular momentum larger than $2\hbar$ gave a very small effect on the observables of the present reaction. The bins were calculated in the energy range of $0 \leq \varepsilon \leq 8$ MeV equaly spaced in momentum. The interaction potential was expanded in multipoles up to $Q_{\max} = 2$.

It is also essential to analyze the convergence of cross sections for the observables concerning the maximum hyper-momentum. In Fig. 6.7, the convergence of the breakup angular distributions upon $K_{\max}$ is studied. The major differences among the theoretical angular distributions are observed at the peak around 40 degrees, where the cross section for $K_{\max} = 18$ is about 40% larger than for $K_{\max} = 8$. The convergence was not achieved in this peak, which should be dominated by the Coulomb breakup, even for $K_{\max} = 18$.

Another important quantity that deserves special attention is the partial breakup cross section. Fig. 6.8 shows that the $K_{\max} = 10, 12$,14, 16 and 18 partial cross sections. As expected, one observes a similar behavior obtained for the breakup angular distribution. The effect of the maximum hypermomentum on the partial breakup cross section is more relevant at the maximum near $J = 16\hbar$.

The elastic angular distributions and the total reaction cross section are two observables that can be determined with confidence in CDCC calculations. In Fig 6.9, the

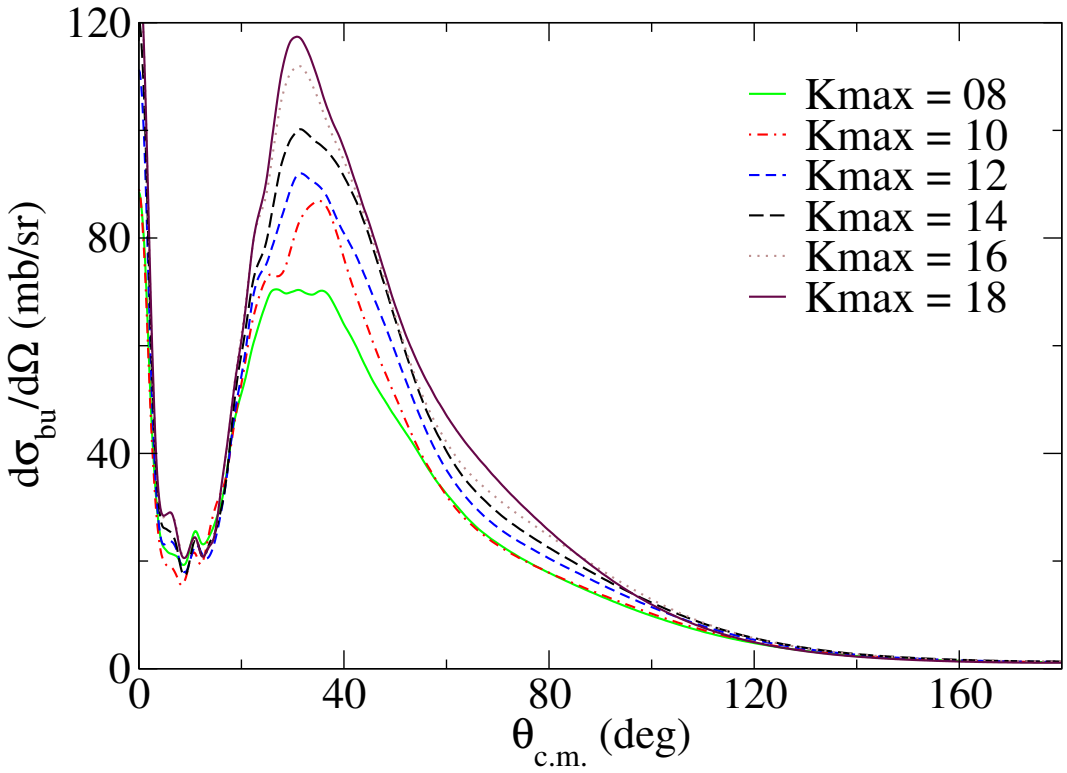

Figure 6.7: Breakup differential cross section for the ^{6}He + ^{208}Pb reaction at 22 MeV.

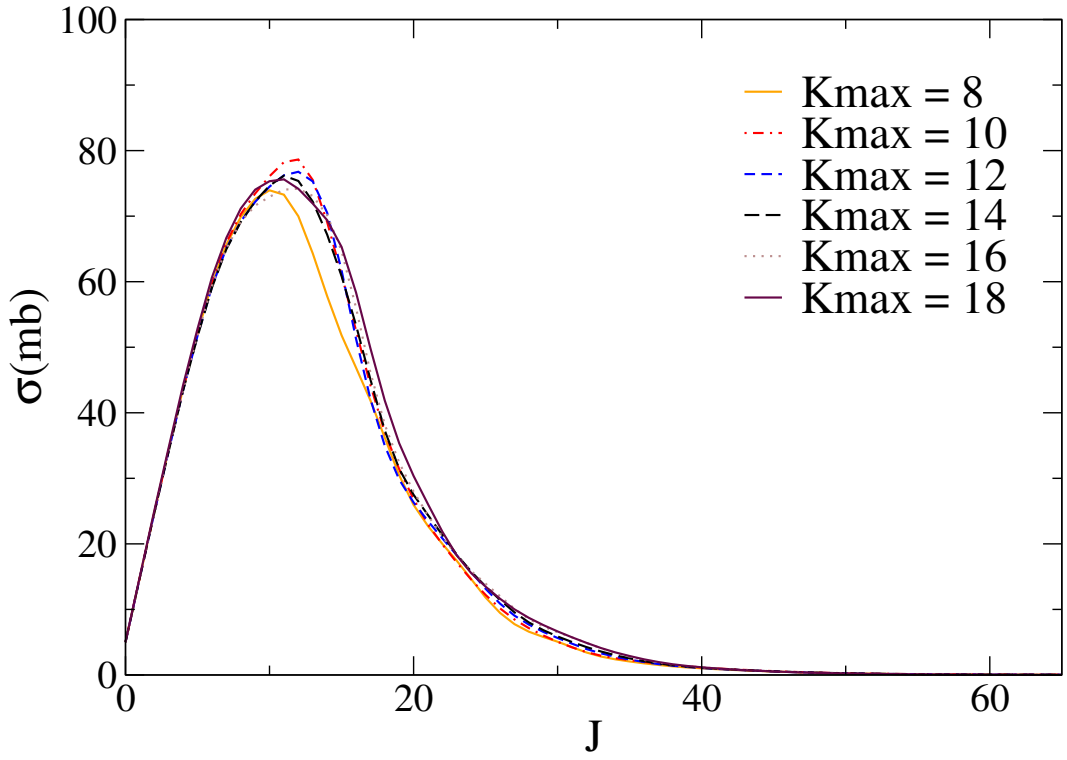

Figure 6.8: Partial breakup cross section for the ^{6}He + ^{208}Pb reaction at 22 MeV.

derived elastic cross section for all $K_{\max}$ studied are shown. One observed very similar angular distributions and good agreement with the experimental data taken from Ref. [8]. This confirms the results of Ref. [42] about the convergence of this observable for $K_{\max} = 8$.

The study of convergence performed in this section allows considering the $K_{\max} = 8$ sufficient to determine the elastic scattering, although it be questionable for the breakup cross sections. Maybe for transition probabilities B(Eλ), a slightly higher $K_{\max}$ would be necessary. Nevertheless, this is out of our computational capacity. Also, the experimental B(Eλ)s are usually determined with no very high precision, especially for reactions involving radioactive beams.

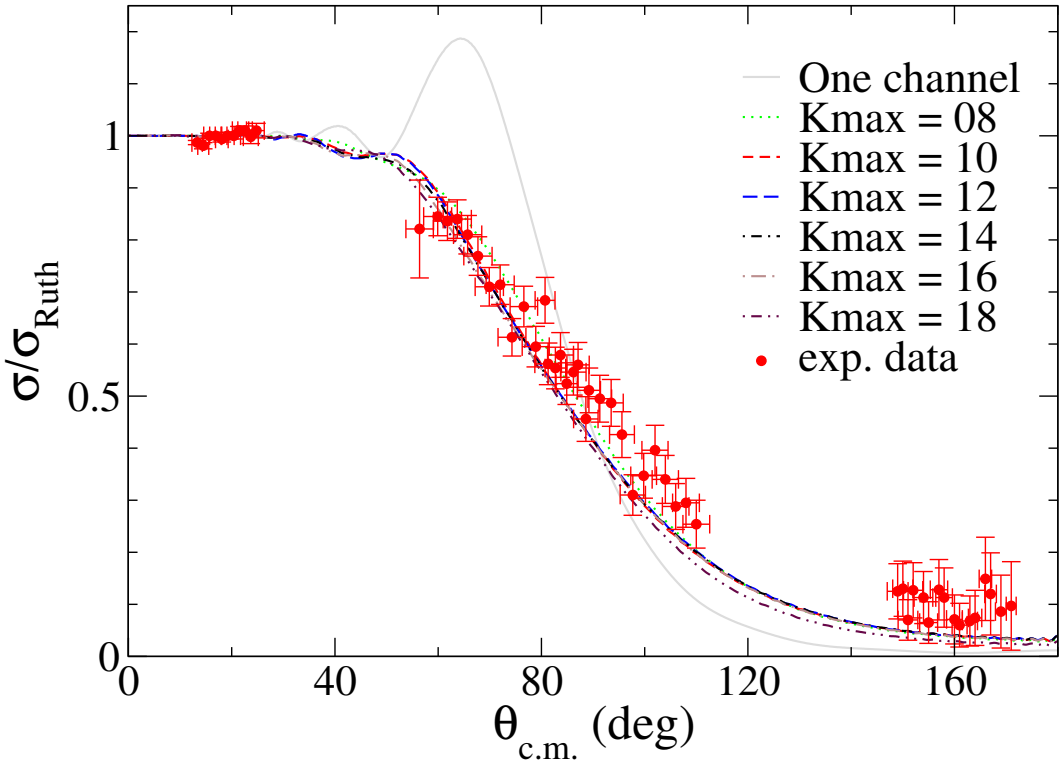

Figure 6.9: Elastic differential cross section for the ^{6}He + ^{208}Pb reaction at 22 MeV. The experimental data are taken from Ref. [8]

6.1.2 ^{6}He+^{197}Au

To better support our study about the convergence of CDCC calculations performed for the ^{6}He + ^{208}Pb system in the previous subsection, we repeat the same procedure for the ^{6}He + ^{197}Au system. For the last system, experimental angular distributions are available at some near barrier energies [10, 47]. The mass of the targets is very similar, and although the ^{208}Pb is a double-magic nucleus, no significant difference should be expected for both systems.

The values of J, R_{match}, number of bins, and the energy bins range and widths are the as same used for the ^{6}He + ^{208}Pb system. However, the optical potential to describe the interaction between the neutrons and ^{197}Au was taken from Ref. [53]. The ^{4}He + ^{197}Au interaction was taken from Ref. [131]. Some tests using the São Paulo Potential [54] were performed. However, because of the appearance of numeric errors, this attempt was dropped out.

The study of the convergence of the maximum hyper-momentum shows a behavior similar to the one observed in the previous results for the scattering on ^{208}Pb, concerning the breakup angular distribution, as seen in Fig. 6.10. This observable has not converged for the $K_{\max} = 18$. This can be a relevant convergence problem since the experimental data for this observable usually would allow distinguishing the converged curves. This behavior can be observed in Fig. 6.11. At 27 MeV, the maximum of the partial breakup cross section for $K_{\max} = 8$ and 18 has a difference of about 4 mb. This difference remains the same for 29 MeV. However, at 40 MeV, the differences between the partial cross section for each maximum hypermomentum is about 6 mb.

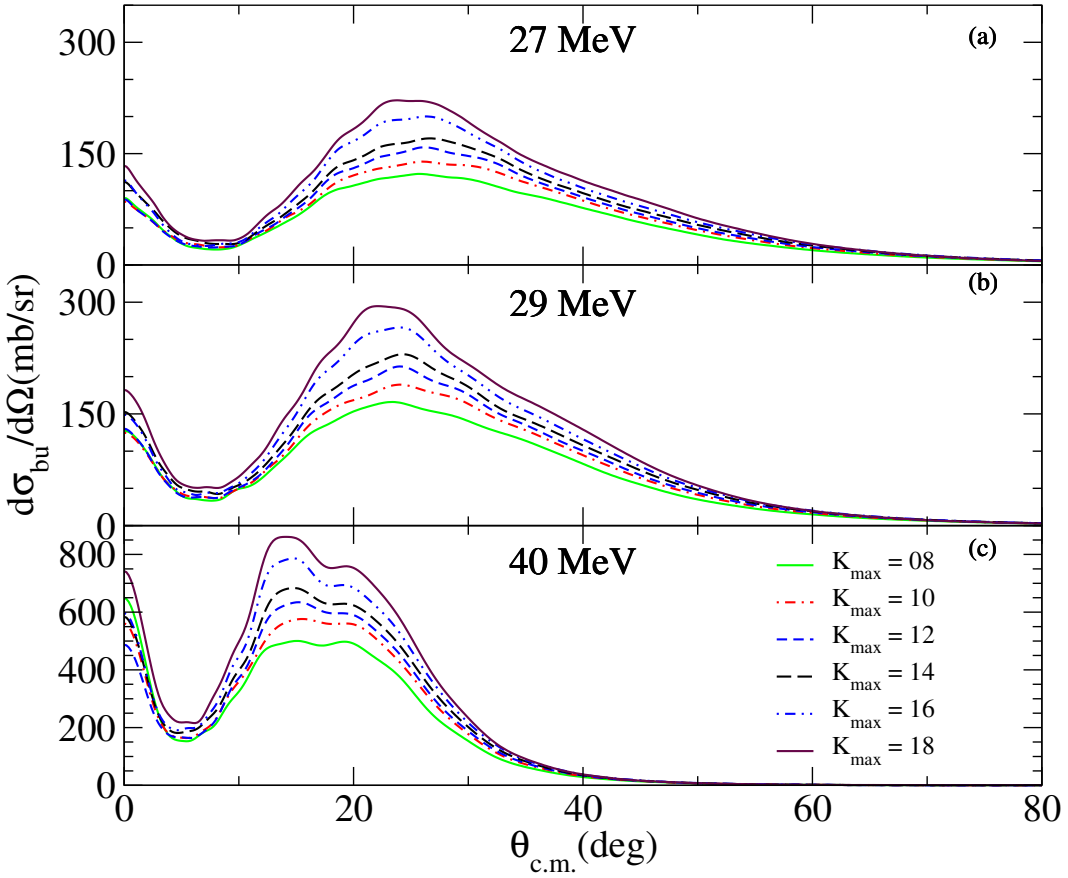

Figure 6.10: Breakup differential cross section for the ^{6}He + ^{197}Au reaction at 27 MeV(a), 29 MeV(b), and 40 MeV(c). It was not possible to produce the theoretical cross section with $K_{\text{Max}} = 18$ at 27 and 29 MeV due to computational limits.

Similar to the ^{208}Pb target observations, the elastic differential cross section for the ^{6}He + ^{197}Au system does not show any significant difference for the various $K_{\max}$ considered (see Fig. 6.12). The theoretical cross section in the energy range agrees with the experimental data taken from Refs. [9, 10].

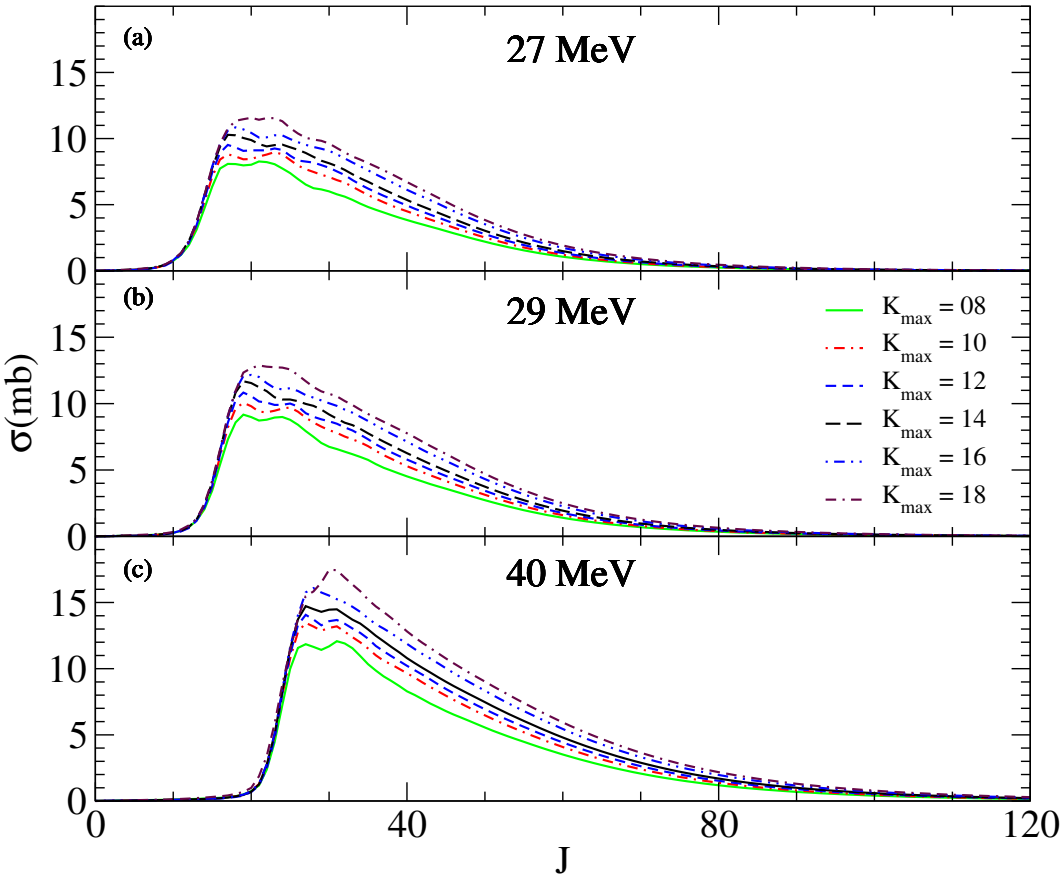

Figure 6.11: Partial breakup cross section for ^{6}He + ^{197}Au reaction at 27 MeV(a), 29 MeV(b), and 40 MeV(c).

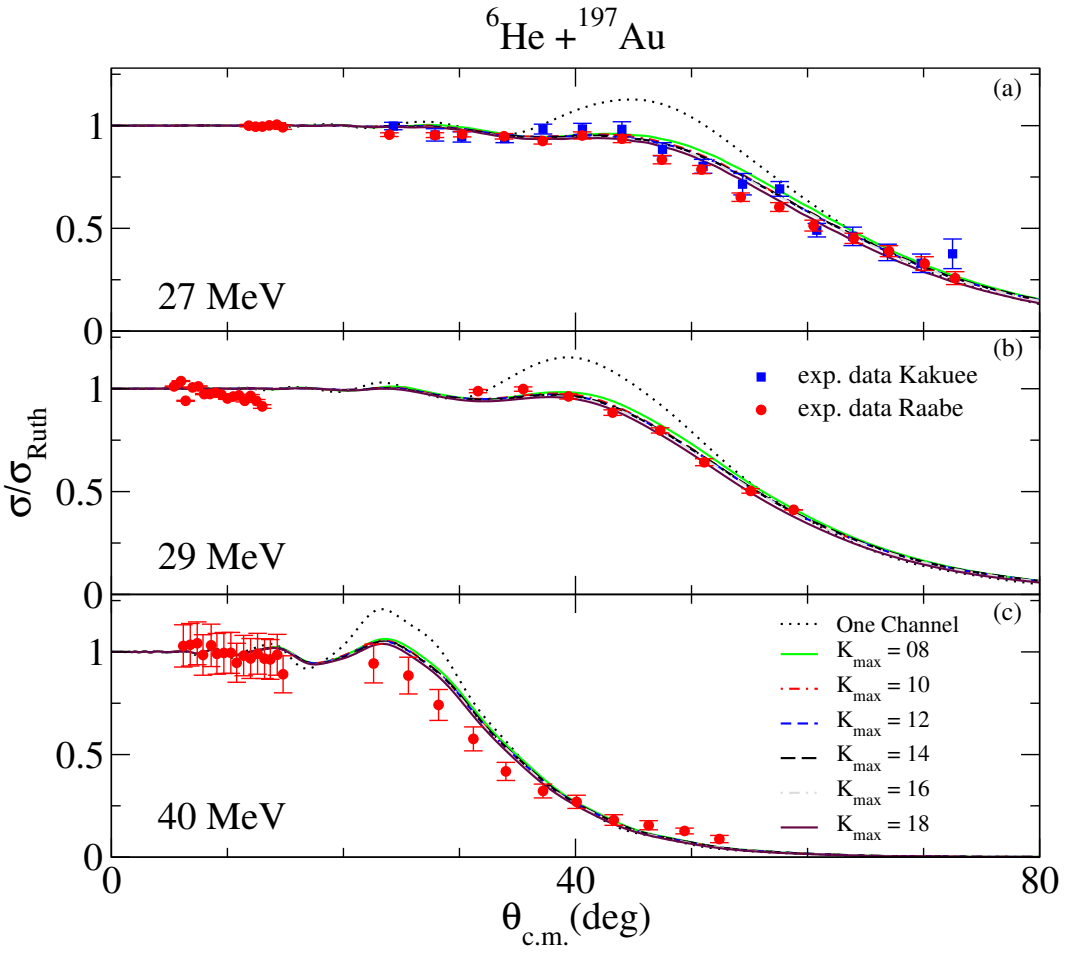

Figure 6.12: Elastic differential cross section for ^{6}He + ^{197}Au reaction at 27 MeV(a), 29 MeV(b), and 40 MeV(c). The experimental data are taken from [9, 10]

Chapter 7
Conclusions

This thesis shows that many interesting phenomena can occur in reactions involving neutron-rich nuclei. While the tools already used can describe the available data satisfactorily, such as coupled channels, coupled reaction channels, etc., some process demands more theory development. Also, many researchers show interest in this topic because neutron-rich nuclei are significant in nucleosynthesis, either in accelerators or astrophysical environments. This work endeavored to collaborate in the discussion and bring some reflections on the subject, applying and developing theoretical techniques to study different nuclear systems and reactions.

As described in chapter 2, the CC method provided good results in describing elastic and inelastic cross sections for the ^{9}Be + ^{197}Au system. The elastic and inelastic angular distribution at energies around the Coulomb barrier were analyzed using the SPP systematic. A very good description of both angular distributions was achieved. In the inelastic scattering, it was shown that the sum of two states (at 270 and 279 keV) was essential to describe the angular distributions.

Besides the inelastic scattering, the neutron transfer channels (stripping and pickup) are very important reaction mechanisms for this system. Dealing with the ^{197}Au(^{9}Be,^{8}Be)^{198}Au reaction, at energies near and above the Coulomb barrier, the theory agrees with the experimental data when many states of the residual ^{198}Au are included. The coupling of the 3.03(2^{+}) resonant state of the ^{8}Be was of utmost relevance to describe the present experimental data. At energies well below the barrier, the experimental data were underestimated. The neutron absorption after the breakup of the ^{9}Be projectile and the direct one-neutron stripping produces the same residual nucleus ^{198}Au. This might suggest that the target could absorb part of the neutrons produced from the breakup. Also, The IAV method can be a solution to this issue. Preliminary calculations showed a good description of the data for low energies and corroborated the importance of the 3.03(2^{+}) resonance state of the ^{8}Be for the cross section.

Concerning the one-neutron pickup reaction ^{197}Au(^{9}Be,^{1}0Be)^{196}Au, it is obtained a fairly good description of the experimental data. The deviation may result from the lack of the microscopic calculation for the spectroscopic amplitudes between the target/residual nucleus overlap. The effect of the breakup mechanism on this channel was also found negligible.

Besides the elastic, inelastic, and one-neutron transfer, we have analyzed the fusion process. To study the effect of the breakup plus transfer channels on the TF and CF, the UFF described in subsection 2.6.1 was used, using the SPP as a bare potential. For

energies above the Coulomb barrier, the CF was hindered by about 45% compared with the benchmark universal fusion function. This is slightly above the 30% - 35% systematic value, but in agreement with the value obtained for the same system by other groups [2,7]. At energies below the barrier, the CF was enhanced in agreement with the results reported in the literature. Concerning the TF, a hindrance of about 10% at energies above the Coulomb barrier was obtained. This result disagrees with the results found for the same system by Li *et al.* [7] and also with the result for the ^{9}Be + ^{208}Pb system [6]. The difference might arrive from the experiential techniques used to measure the experiential data. More experiential data for similar systems are required to derive a definite conclusion

The fusion cross section of the open neutron shell nuclei ^{41,45}K is significantly reduced compared to the closed neutron shell isotopes ^{39,47}K for both targets, ^{16}O and ^{28}Si. In the ^{16}O target case, the cross section is overpredicted when considering the 2pF densities. Using more realistic density distributions from DHB calculations resulted in a reduction of the predicted fusion cross section as compared to the systematics. For the open-shell nuclei, the DHB densities in the SPP provided a reasonable description from the experimental data, particularly for the K isotopes. However, the cross section for the closed-shell nuclei is still overpredicted, particularly above the barrier.

For the ^{28}Si target case, when using the DHB matter density, the theoretical description of the fusion cross section for closed-shell nuclei provided a reasonable description of the data. The theory significantly underpredicts the measured cross section for the open-shell nuclei, particularly below the barrier. However, a closer look at the system shows that the coupling with the transfer channels may cause the effect of enhancing the experimental data. This shows the necessity for further analysis of this system and systems that exhibit similar structures to understand better the mechanisms involved.

To analyze the 6He+208Pb elastic angular distribution, it was performed 4-body CDCC calculations. An attempt to check the convergence for other observables was performed. The CDCC calculations were extended for the ^{208}Pb to the ^{197}Au target, for which experimental elastic scattering angular distributions are also available.

In any coupled channel calculation, it is required to truncate the model space. Sometimes the truncation occurs for physical reasons and others due to computational limits. In this thesis, the truncation of the maximum hyper-momentum was governed by describing reasonably well reaction observables like the elastic and the breakup differential cross sections. The $B(E1)$ shows some dependence on the maximum $K_{\max}$, demanding values larger than 8, used to describe the elastic scattering in previous studies. On the contrary, the $B(E2)$ distributions remain almost insensitive to the inclusion of values of $K_{\max} > 8$. Some dependence on $K_{\max}$ were found in the eigenphases, mainly in the $J^{\pi} = 1^{-}$. The breakup angular distributions seem to be more sensitive to the values of $K_{\max}$, especially in the peak dominated by Coulomb interactions. In the same way, the partial breakup distributions is very sensitive to changes in $K_{\max}$. On the other hand, the convergence of the elastic cross section is faster, demanding lower values of $K_{\max}$, as shown in Ref [41]. The agreement with the experimental elastic angular distributions was very good.

The results of the theoretical calculations on ^{6}He + ^{197}Au system corroborated the

results for the ^{208}Pb target. The elastic differential cross section also converged faster than other observables using the same $K_{\max} = 8$ as in the case of the ^{208}Pb target. The dependence of the elastic scattering on $K_{\max}$ may be more significant in the reactions involving light nuclei, as shown in Ref. [132]. The elastic cross section for the ^{6}He + ^{197}Au system was quite sensitive to the α + ^{197}Au potential.

The convergence of the breakup differential cross section is slower, as observed for ^{208}Pb target. It is important to state that for the breakup cross section we did not achieve the full convergence $K_{\max}$ (even for $K_{\max} = 18$), due to computational limits.

The good description of the elastic scattering angular distributions proved that the CDCC method using hyperspherical coordinates for the projectile is a reliable model to perform four-body calculations usually needed to study the breakup process for Borromean projectiles.

Bibliography

1 JOHNSTONE, J. E.; SINGH, V.; GIRI, R.; HUDAN, S.; VADAS, J.; DESOUZA, R. T.; ACKERMANN, D.; CHBIHI, A.; HOURDILLE, Q.; ABBOTT, A.; BALHOFF, C.; HANNAMAN, A.; MCINTOSH, A. B.; SORENSEN, M.; TOBIN, Z.; WAKHLE, A.; YENNELLO, S. J.; FAMIANO, M. A.; BROWN, K. W.; SANTAMARIA, C.; LUBIAN, J.; SOLER, H. O.; CARLSON, B. V. Proton and neutron exchange as a prelude to fusion at near-barrier energies. *Phys. Rev. C*, American Physical Society, v. 106, p. L011603, Jul 2022. Disponível em: <https://link.aps.org/doi/10.1103/PhysRevC.106.L011603>.

2 GOLLAN, F.; ABRIOLA, D.; ARAZI, A.; CARDONA, M. A.; BARBARÁ, E. de; JESÚS, J. de; HOJMAN, D.; BETAN, R. M. I.; LUBIAN, J.; PACHECO, A. J.; PAES, B.; SCHNEIDER, D.; SOLER, H. O. One-neutron transfer, complete fusion, and incomplete fusion from the ^{9}Be + ^{197}Au reaction. *Phys. Rev. C*, American Physical Society, v. 104, p. 024609, Aug 2021. Disponível em: <https://link.aps.org/doi/10.1103/PhysRevC.104.024609>.

3 KAUSHIK, M.; GUPTA, G.; THAKUR, S.; KRISHNAMOORTHY, H.; SINGH, P. P.; PARKAR, V. V.; NANAL, V.; SHRIVASTAVA, A.; PILLAY, R. G.; MAHATA, K.; RAMACHANDRAN, K.; PAL, S.; PALSHETKAR, C. S.; PANDIT, S. K. Fusion of the borromean nucleus ^{9}Be with a ^{197}Au target at near-barrier energies. *Phys. Rev. C*, American Physical Society, v. 101, p. 034611, Mar 2020. Disponível em: <https://link.aps.org/doi/10.1103/PhysRevC.101.034611>.

4 FANG, Y. D.; GOMES, P. R. S.; LUBIAN, J.; ZHOU, X. H.; ZHANG, Y. H.; HAN, J. L.; LIU, M. L.; ZHENG, Y.; GUO, S.; WANG, J. G.; QIANG, Y. H.; WANG, Z. G.; WU, X. G.; HE, C. Y.; ZHENG, Y.; LI, C. B.; HU, S. P.; YAO, S. H. Fusion and one-neutron stripping reactions in the 9 be+ 186 w system above the coulomb barrier. *Phys. Rev. C*, v. 87, n. 2, p. 024604, 2013.

5 GOMES, P.; LUBIAN, J.; PAES, B.; GARCIA, V.; MONTEIRO, D.; PADRÓN, I.; FIGUEIRA, J.; ARAZI, A.; CAPURRO, O.; FIMIANI, L. *et al.* Near-barrier fusion, breakup and scattering for the 9be+ 144sm system. *Nuclear Physics A*, Elsevier, v. 828, n. 3-4, p. 233–252, 2009.

6 DASGUPTA, M.; GOMES, P.; HINDE, D.; MORAES, S.; ANJOS, R.; BERRIMAN, A.; BUTT, R. D.; CARLIN, N.; LUBIAN, J.; MORTON, C. *et al.* Effect of breakup on the fusion of li 6, li 7, and be 9 with heavy nuclei. *Physical Review C*, APS, v. 70, n. 2, p. 024606, 2004.

7 LI, G. S.; WANG, J. G.; LUBIAN, J.; SOLER, H. O.; FANG, Y. D.; LIU, M. L.; ZHANG, N. T.; ZHOU, X. H.; ZHANG, Y. H.; GAO, B. S.; QIANG, Y. H.; GUO, S.; WANG, S. C.; WANG, K. L.; ZHENG, K. K.; LI, R.; ZHENG, Y. Fusion reactions in the ^{9}Be +^{197} Au system above the coulomb barrier. *Phys.*

Rev. C, American Physical Society, v. 100, p. 054601, Nov 2019. Disponível em: <https://link.aps.org/doi/10.1103/PhysRevC.100.054601>.

8 ACOSTA, L.; SÁNCHEZ-BENÍTEZ, A.; GÓMEZ, M.; MARTEL, I.; PÉREZ-BERNAL, F.; PIZARRO, F.; RODRÍGUEZ-QUINTERO, J.; RUSEK, K.; ALVAREZ, M.; ANDRÉS, M. *et al.* Elastic scattering and α-particle production in 6 he+ 208 pb collisions at 22 mev. *Physical Review C*, APS, v. 84, n. 4, p. 044604, 2011.

9 RAABE, R. Tese (Doutorado) — Katholieke Universiteit Leuven, 2001. Disponível em: <http://www.fys.kuleuven.ac.be/iks/lisol/research/6he4he/PhDthesis.pdf>.

10 KAKUEE, O.; ALVAREZ, M.; ANDRéS, M.; CHERUBINI, S.; DAVINSON, T.; Di Pietro, A.; GALSTER, W.; GóMEZ-CAMACHO, J.; LAIRD, A.; LAMEHI-RACHTI, M.; MARTEL, I.; MORO, A.; RAHIGHI, J.; SáNCHEZ-BENITEZ, A.; SHOTTER, A.; SMITH, W.; VERVIER, J.; WOODS, P. Long range absorption in the scattering of 6he on 208pb and 197au at 27 mev. *Nuclear Physics A*, v. 765, n. 3, p. 294–306, 2006. ISSN 0375-9474. Disponível em: <https://www.sciencedirect.com/science/article/pii/S0375947405012005>.

11 ALEXANDER, A. *Infinitesimal: How a dangerous mathematical theory shaped the modern world*. [S.l.]: Macmillan, 2014.

12 GENET, M. The discovery of uranic rays: a short step for henri becquerel but a giant step for science. *Radiochimica Acta*, De Gruyter Oldenbourg, v. 70, n. s1, p. 3–12, 1995.

13 THOMSON, J. J. Xl. cathode rays. *The London, Edinburgh, and Dublin Philosophical Magazine and Journal of Science*, Taylor & Francis, v. 44, n. 269, p. 293–316, 1897.

14 HON, G.; GOLDSTEIN, B. R. Jj thomson's plum-pudding atomic model: The making of a scientific myth. *Annalen der Physik*, v. 525, n. 8-9, p. A129–A133, 2013.

15 RUTHERFORD, E.; SODDY, F. Lx. radioactive change. *The London, Edinburgh, and Dublin Philosophical Magazine and Journal of Science*, Taylor & Francis, v. 5, n. 29, p. 576–591, 1903.

16 RUTHERFORD, E. Liv. collision of α particles with light atoms. iv. an anomalous effect in nitrogen. *The London, Edinburgh, and Dublin Philosophical Magazine and Journal of Science*, Taylor & Francis, v. 37, n. 222, p. 581–587, 1919.

17 THOMPSON, I. J.; NUNES, F. M. *Nuclear reactions for astrophysics: principles, calculation and applications of low-energy reactions*. [S.l.]: Cambridge University Press, 2009.

18 YAHIRO, M.; ISERI, Y.; KAMEYAMA, H.; KAMIMURA, M.; KAWAI, M. Chapter iii. effects of deuteron virtual breakup on deuteron elastic and inelastic scattering. *Progress of Theoretical Physics Supplement*, Oxford Academic, v. 89, p. 32–83, 1986.

19 AUSTERN, N.; ISERI, Y.; KAMIMURA, M.; KAWAI, M.; RAWITSCHER, G.; YAHIRO, M. Continuum-discretized coupled-channels calculations for three-body models of deuteron-nucleus reactions. *Physics Reports*, Elsevier, v. 154, n. 3, p. 125–204, 1987.

20 KOLATA, J.; GUIMARAES, V.; PETERSON, D.; SANTI, P.; WHITE-STEVENS, R.; DEYOUNG, P.; PEASLEE, G. F.; HUGHEY, B.; ATALLA, B.; KERN, M. *et al.* Sub-barrier fusion of h 6 e with b 209 i. *Physical review letters*, APS, v. 81, n. 21, p. 4580, 1998.

21 LEMASSON, A.; SHRIVASTAVA, A.; NAVIN, A.; REJMUND, M.; KEELEY, N.; ZELEVINSKY, V.; BHATTACHARYYA, S.; CHATTERJEE, A.; FRANCE, G. D.; JACQUOT, B. *et al.* Modern rutherford experiment: Tunneling of the most neutron-rich nucleus. *Phys. Rev. Lett.*, APS, v. 103, n. 23, p. 232701, 2009.

22 DASGUPTA, M.; HINDE, D.; HAGINO, K.; MORAES, S.; GOMES, P.; ANJOS, R.; BUTT, R.; BERRIMAN, A.; CARLIN, N.; MORTON, C. *et al.* Fusion and breakup in the reactions of 6 li and 7 li nuclei with 209 bi. *Physical Review C*, APS, v. 66, n. 4, p. 041602, 2002.

23 CUBERO, M.; FERNÁNDEZ-GARCÍA, J.; RODRÍGUEZ-GALLARDO, M.; ACOSTA, L.; ALCORTA, M.; ALVAREZ, M.; BORGE, M.; BUCHMANN, L.; DIGET, C. A.; FALOU, H. A. *et al.* Do halo nuclei follow rutherford elastic scattering at energies below the barrier? the case of li 11. *Physical review letters*, APS, v. 109, n. 26, p. 262701, 2012.

24 DASGUPTA, M.; HINDE, D.; BUTT, R. D.; ANJOS, R.; BERRIMAN, A.; CARLIN, N.; GOMES, P.; MORTON, C.; NEWTON, J.; TOLEDO, A. S. D. *et al.* Fusion versus breakup: Observation of large fusion suppression for 9 b e+ 208 pb. *Physical review letters*, APS, v. 82, n. 7, p. 1395, 1999.

25 FANG, Y. D.; GOMES, P. R. S.; LUBIAN, J.; LIU, M. L.; ZHOU, X. H.; JUNIOR, D. R. M.; ZHANG, N. T.; ZHANG, Y. H.; LI, G. S.; WANG, J. G.; GUO, S.; QIANG, Y. H.; GAO, B. S.; ZHENG, Y.; LEI, X. G.; WANG, Z. G. Complete and incomplete fusion of ^{9}Be + ^{169}Tm,^{187} Re at near-barrier energies. *Phys. Rev. C*, American Physical Society, v. 91, p. 014608, Jan 2015.

26 KAUSHIK, M.; GUPTA, G.; THAKUR, S.; KRISHNAMOORTHY, H.; SINGH, P. P.; PARKAR, V. V.; NANAL, V.; SHRIVASTAVA, A.; PILLAY, R. G.; MAHATA, K.; RAMACHANDRAN, K.; PAL, S.; PALSHETKAR, C. S.; PANDIT, S. K. Fusion of the borromean nucleus ^{9}Be with a ^{197}Au target at near-barrier energies. *Phys. Rev. C*, American Physical Society, v. 101, p. 034611, Mar 2020. Disponível em: <https://link.aps.org/doi/10.1103/PhysRevC.101.034611>.

27 SIGNORINI, C.; YOSHIDA, A.; WATANABE, Y.; PIERROUTSAKOU, D.; STROE, L.; FUKUDA, T.; MAZZOCCO, M.; FUKUDA, N.; MIZOI, Y.; ISHIHARA, M. *et al.* Subbarrier fusion in the systems 11, 10be+ 209bi. *Nuclear Physics A*, Elsevier, v. 735, n. 3-4, p. 329–344, 2004.

28 SAKURAGI, Y.; YAHIRO, M.; KAMIMURA, M. Chapter vi. microscopic coupled-channels study of scattering and breakup of light heavy-ions. *Progress of Theoretical Physics Supplement*, Narnia, v. 89, p. 136–211, 1986.

29 NUNES, F.; THOMPSON, I. Multistep effects in sub-coulomb breakup. *Physical Review C*, APS, v. 59, n. 5, p. 2652, 1999.

30 TOSTEVIN, J.; NUNES, F.; THOMPSON, I. Calculations of three-body observables in 8 b breakup. *Physical Review C*, APS, v. 63, n. 2, p. 024617, 2001.

31 SUMMERS, N.; NUNES, F.; THOMPSON, I. Extended continuum discretized coupled channels method: Core excitation in the breakup of exotic nuclei. *Physical Review C*, APS, v. 74, n. 1, p. 014606, 2006.

32 MUKERU, B.; LEKALA, M. L.; LUBIAN, J.; TOMIO, L. Theoretical analysis of 8li+ 208pb reaction and the critical angular momentum for complete fusion. *Nuclear Physics A*, Elsevier, v. 996, p. 121700, 2020.

33 GUIMARÃES, V.; CARDOZO, E.; SCARDUELLI, V.; LUBIAN, J.; KOLATA, J.; O'MALLEY, P.; BARDAYAN, D.; AGUILERA, E.; MARTINEZ-QUIROZ, E.; LIZCANO, D. *et al.* Strong coupling effect in the elastic scattering of the c 10+ ni 58 system near barrier. *Physical Review C*, APS, v. 100, n. 3, p. 034603, 2019.

34 MAZZOCCO, M.; KEELEY, N.; BOIANO, A.; BOIANO, C.; COMMARA, M. L.; MANEA, C.; PARASCANDOLO, C.; PIERROUTSAKOU, D.; SIGNORINI, C.; STRANO, E. *et al.* Elastic scattering for the b 8 and be 7+ pb 208 systems at near-coulomb barrier energies. *Physical Review C*, APS, v. 100, n. 2, p. 024602, 2019.

35 MORO, A.; CASAL, J.; GÓMEZ-RAMOS, M. Investigating the 10li continuum through 9li (d, p) 10li reactions. *Physics Letters B*, Elsevier, v. 793, p. 13–18, 2019.

36 AGUILERA, E.; MARTINEZ-QUIROZ, E.; LIZCANO, D.; GÓMEZ-CAMACHO, A.; KOLATA, J.; LAMM, L.; GUIMARÃES, V.; LICHTENTHÄLER, R.; CAMARGO, O.; BECCHETTI, F. *et al.* Reaction cross sections for b 8, be 7, and li 6+ ni 58 near the coulomb barrier: Proton-halo effects. *Physical Review C*, APS, v. 79, n. 2, p. 021601, 2009.

37 PARKAR, V.; JHA, V.; KAILAS, S. Exploring contributions from incomplete fusion in li 6, 7+ bi 209 and li 6, 7+ pt 198 reactions. *Physical Review C*, APS, v. 94, n. 2, p. 024609, 2016.

38 CAMACHO, A. G.; LUBIAN, J.; ZHANG, H.; ZHOU, S.-G. Cdcc calculations of fusion of 6li with targets 144sm and 154sm: effect of resonance states. *Chinese Physics C*, IOP Publishing, v. 41, n. 12, p. 124103, 2017.

39 MATSUMOTO, T.; KAMIZATO, T.; OGATA, K.; ISERI, Y.; HIYAMA, E.; KAMIMURA, M.; YAHIRO, M. New treatment of breakup continuum in the method of continuum discretized coupled channels. *Physical Review C*, APS, v. 68, n. 6, p. 064607, 2003.

40 MATSUMOTO, T.; EGAMI, T.; OGATA, K.; ISERI, Y.; KAMIMURA, M.; YAHIRO, M. Coulomb breakup effects on the elastic cross section of ^{6}He+^{209}Bi scattering near coulomb barrier energies. *Phys. Rev. C*, American Physical Society, v. 73, p. 051602, May 2006. Disponível em: <https://link.aps.org/doi/10.1103/PhysRevC.73.051602>.

41 RODRÍGUEZ-GALLARDO, M.; ARIAS, J. M.; GÓMEZ-CAMACHO, J.; JOHNSON, R. C.; MORO, A. M.; THOMPSON, I. J.; TOSTEVIN, J. A. Four-body continuum-discretized coupled-channels calculations using a transformed harmonic oscillator basis. *Phys. Rev. C*, American Physical Society, v. 77, p. 064609, Jun 2008. Disponível em: <https://link.aps.org/doi/10.1103/PhysRevC.77.064609>.

42 RODRÍGUEZ-GALLARDO, M.; ARIAS, J.; GÓMEZ-CAMACHO, J.; MORO, A.; THOMPSON, I.; TOSTEVIN, J. Four-body continuum-discretized coupled-channels calculations. *Physical Review C*, APS, v. 80, n. 5, p. 051601, 2009.

43 DOORNENBAL, P.; SCHEIT, H.; TAKEUCHI, S.; AOI, N.; LI, K.; MATSUSHITA, M.; STEPPENBECK, D.; WANG, H.; BABA, H.; CRAWFORD, H.; HOFFMAN, C. R.; HUGHES, R.; IDEGUCHI, E.; KOBAYASHI, N.; KONDO, Y.; LEE, J.; MICHIMASA, S.; MOTOBAYASHI, T.; SAKURAI, H.; TAKECHI, M.; TOGANO, Y.; WINKLER, R.; YONEDA, K. In-beam γ-ray spectroscopy of ^{34,36,38}Mg: Merging the n=20 and n=28 shell quenching. *Phys. Rev. Lett.*, American Physical Society, v. 111, p. 212502, Nov 2013. Disponível em: <https://link.aps.org/doi/10.1103/PhysRevLett.111.212502>.

44 KANUNGO, R.; TANIHATA, I.; OZAWA, A. Observation of new neutron and proton magic numbers. *Physics Letters B*, v. 528, n. 1, p. 58–64, 2002. ISSN 0370-2693. Disponível em: <https://www.sciencedirect.com/science/article/pii/S0370269302012066>.

45 KEELEY, N.; KEMPER, K. W.; RUSEK, K. Dynamic polarization potentials and dipole polarizabilities of ^{11}li, ^{6}he and ^{6}li compared. *Phys. Rev. C*, American Physical Society, v. 88, p. 017602, Jul 2013. Disponível em: <https://link.aps.org/doi/10.1103/PhysRevC.88.017602>.

46 CANTO, L.; GOMES, P.; DONANGELO, R.; HUSSEIN, M. Fusion and breakup of weakly bound nuclei. *Physics Reports*, v. 424, n. 1, p. 1–111, 2006. ISSN 0370-1573. Disponível em: <https://www.sciencedirect.com/science/article/pii/S037015730500459X>.

47 RUSEK, K.; MARTEL, I.; GÓMEZ-CAMACHO, J.; MORO, A.; RAABE, R. Three-body continuum-discretized coupled-channel calculations for he 6 scattering from heavy nuclei. *Physical Review C*, APS, v. 72, n. 3, p. 037603, 2005.

48 MORO, A.; RUSEK, K.; ARIAS, J.; GÓMEZ-CAMACHO, J.; RODRÍGUEZ-GALLARDO, M. Improved di-neutron cluster model for he 6 scattering. *Physical Review C*, APS, v. 75, n. 6, p. 064607, 2007.

49 FERNÁNDEZ-GARCÍA, J. P.; CUBERO, M.; RODRÍGUEZ-GALLARDO, M.; ACOSTA, L.; ALCORTA, M.; ALVAREZ, M. A. G.; BORGE, M. J. G.; BUCHMANN, L.; DIGET, C. A.; FALOU, H. A.; FULTON, B. R.; FYNBO, H. O. U.; GALAVIZ, D.; GÓMEZ-CAMACHO, J.; KANUNGO, R.; LAY, J. A.; MADURGA, M.; MARTEL, I.; MORO, A. M.; MUKHA, I.; NILSSON, T.; SÁNCHEZ-BENÍTEZ, A. M.; SHOTTER, A.; TENGBLAD, O.; WALDEN, P. ^{11}Li breakup on ^{208}Pb at energies around the coulomb barrier. *Phys. Rev. Lett.*, American Physical Society, v. 110, p. 142701, Apr 2013. Disponível em: <https://link.aps.org/doi/10.1103/PhysRevLett.110.142701>.

50 ARAZI, A.; CASAL, J.; RODRÍGUEZ-GALLARDO, M.; ARIAS, J. M.; FILHO, R. L.; ABRIOLA, D.; CAPURRO, O. A.; CARDONA, M. A.; CARNELLI, P. F. F.; BARBARÁ, E. de; NIELLO, J. F.; FIGUEIRA, J. M.; FIMIANI, L.; HOJMAN, D.; MARTÍ, G. V.; HEIMMAN, D. M.; PACHECO, A. J. ^{9}Be +^{120} Sn scattering at near-barrier energies within a four-body model. *Phys. Rev. C*, American Physical Society, v. 97, p. 044609, Apr 2018. Disponível em: <https://link.aps.org/doi/10.1103/PhysRevC.97.044609>.

51 CASAL, J.; RODRÍGUEZ-GALLARDO, M.; ARIAS, J. M. ^{9}Be elastic scattering on ^{208}Pb and ^{27}Al within a four-body reaction framework. *Phys. Rev. C*, American Physical Society, v. 92, p. 054611, Nov 2015. Disponível em: <https://link.aps.org/doi/10.1103/PhysRevC.92.054611>.

52 ICHIMURA, M.; AUSTERN, N.; VINCENT, C. M. Equivalence of post and prior sum rules for inclusive breakup reactions. *Phys. Rev. C*, American Physical Society, v. 32, p. 431–439, Aug 1985. Disponível em: <https://link.aps.org/doi/10.1103/PhysRevC.32.431>.

53 KONING, A.; DELAROCHE, J. Local and global nucleon optical models from 1 kev to 200 mev. *Nuclear Physics A*, v. 713, n. 3, p. 231–310, 2003. ISSN 0375-9474. Disponível em: <https://www.sciencedirect.com/science/article/pii/S0375947402013210>.

54 CHAMON, L. C.; CARLSON, B. V.; GASQUES, L. R.; PEREIRA, D.; CONTI, C. D.; ALVAREZ, M. A. G.; HUSSEIN, M. S.; RIBEIRO, M. A. C.; ROSSI, E. S.; SILVA, C. P. Toward a global description of the nucleus-nucleus interaction. *Phys. Rev. C*, American Physical Society, v. 66, p. 014610, Jul 2002. Disponível em: <https://link.aps.org/doi/10.1103/PhysRevC.66.014610>.

55 PEREIRA, D.; LUBIAN, J.; OLIVEIRA, J.; de Sousa, D.; CHAMON, L. An imaginary potential with universal normalization for dissipative processes in heavy-ion reactions. *Physics Letters B*, v. 670, n. 4, p. 330–335, 2009. ISSN 0370-2693. Disponível em: <https://www.sciencedirect.com/science/article/pii/S0370269308013543>.

56 SINGH, V.; JOHNSTONE, J. E.; GIRI, R.; HUDAN, S.; VADAS, J.; DESOUZA, R. T.; ACKERMANN, D.; CHBIHI, A.; HOURDILLE, Q.; ABBOTT, A.; BALHOFF, C.; HANNAMAN, A.; MCINTOSH, A. B.; SORENSEN, M.; TOBIN, Z.; WAKHLE, A.; YENNELLO, S. J.; FAMIANO, M. A.; BROWN, K. W.; SANTAMARIA, C.; LUBIAN, J.; SOLER, H. O.; CARLSON, B. V. Impact of shell structure on the fusion of neutron-rich mid-mass nuclei. *Phys. Rev. C*, American Physical Society, v. 104, p. L041601, Oct 2021. Disponível em: <https://link.aps.org/doi/10.1103/PhysRevC.104.L041601>.

57 SATCHLER, G. Heavy-ion scattering and reactions near the coulomb barrier and "threshold anomalies". *Physics Reports*, v. 199, n. 3, p. 147–190, 1991. ISSN 0370-1573. Disponível em: <https://www.sciencedirect.com/science/article/pii/037015739190066U>.

58 HUSSEIN, M. S.; GOMES, P. R. S.; LUBIAN, J.; CHAMON, L. C. New manifestation of the dispersion relation: Breakup threshold anomaly. *Phys. Rev. C*, American Physical Society, v. 73, p. 044610, Apr 2006. Disponível em: <https://link.aps.org/doi/10.1103/PhysRevC.73.044610>.

59 PEREIRA, D.; LINARES, R.; OLIVEIRA, J.; LUBIAN, J.; CHAMON, L.; GOMES, P.; CUNSOLO, A.; CAPPUZZELLO, F.; CAVALLARO, M.; CARBONE, D.; FOTI, A. Nuclear rainbow in the 16o+27al system: The role of couplings at energies far above the barrier. *Physics Letters B*, v. 710, n. 3, p. 426–429, 2012. ISSN 0370-2693. Disponível em: <https://www.sciencedirect.com/science/article/pii/S0370269312003061>.

60 FACIO, B. D.; UMERJEE, R. K.; GAMMEL, J. L. Coupled-channel schrödinger-equation model for neutron-alpha and deuteron-triton scattering. i. *Phys. Rev.*,

American Physical Society, v. 151, p. 819–826, Nov 1966. Disponível em: <https://link.aps.org/doi/10.1103/PhysRev.151.819>.

61 CANTO, L. F.; DONANGELO, R.; HUSSEIN, M. S.; LOTTI, P.; LUBIAN, J.; RANGEL, J. Theoretical considerations about heavy-ion fusion in potential scattering. *Phys. Rev. C*, American Physical Society, v. 98, p. 044617, Oct 2018. Disponível em: <https://link.aps.org/doi/10.1103/PhysRevC.98.044617>.

62 WONG, C. Y. Interaction barrier in charged-particle nuclear reactions. *Phys. Rev. Lett.*, American Physical Society, v. 31, p. 766–769, Sep 1973. Disponível em: <https://link.aps.org/doi/10.1103/PhysRevLett.31.766>.

63 GLAS, D.; MOSEL, U. Limitation on complete fusion during heavy-ion collisions. *Phys. Rev. C*, American Physical Society, v. 10, p. 2620–2622, Dec 1974. Disponível em: <https://link.aps.org/doi/10.1103/PhysRevC.10.2620>.

64 GOMES, P. R. S.; LUBIAN, J.; PADRON, I.; ANJOS, R. M. Uncertainties in the comparison of fusion and reaction cross sections of different systems involving weakly bound nuclei. *Phys. Rev. C*, American Physical Society, v. 71, p. 017601, Jan 2005. Disponível em: <https://link.aps.org/doi/10.1103/PhysRevC.71.017601>.

65 CANTO, L. F.; GOMES, P. R. S.; LUBIAN, J.; CHAMON, L. C.; CREMA, E. Disentangling static and dynamic effects of low breakup threshold in fusion reactions. *Journal of Physics G: Nuclear and Particle Physics*, IOP Publishing, v. 36, n. 1, p. 015109, nov 2008. Disponível em: <https://doi.org/10.1088/0954-3899/36/1/015109>.

66 CANTO, L.; GOMES, P.; LUBIAN, J.; CHAMON, L.; CREMA, E. Dynamic effects of breakup on fusion reactions of weakly bound nuclei. *Nuclear Physics A*, v. 821, n. 1, p. 51–71, 2009. ISSN 0375-9474. Disponível em: <https://www.sciencedirect.com/science/article/pii/S0375947409001092>.

67 YANG, L.; LIN, C.; YAMAGUCHI, H.; LEI, J.; WEN, P.; MAZZOCCO, M.; MA, N.; SUN, L.; WANG, D.; ZHANG, G.; ABE, K.; CHA, S.; CHAE, K.; DIAZ-TORRES, A.; FERREIRA, J.; HAYAKAWA, S.; JIA, H.; KAHL, D.; KIM, A.; KWAG, M.; La Commara, M.; Navarro Pérez, R.; PARASCANDOLO, C.; PIERROUTSAKOU, D.; RANGEL, J.; SAKAGUCHI, Y.; SIGNORINI, C.; STRANO, E.; XU, X.; YANG, F.; YANG, Y.; ZHANG, G.; ZHONG, F.; LUBIAN, J. Insight into the reaction dynamics of proton drip-line nuclear system 17f+58ni at near-barrier energies. *Physics Letters B*, v. 813, p. 136045, 2021. ISSN 0370-2693. Disponível em: <https://www.sciencedirect.com/science/article/pii/S0370269320308480>.

68 DESCOUVEMONT, P.; TURSUNOV, E.; BAYE, D. Three-body continuum states on a lagrange mesh. *Nuclear Physics A*, Elsevier, v. 765, n. 3-4, p. 370–389, 2006.

69 FULTON, B. R.; COWIN, R. L.; WOOLLISCROFT, R. J.; CLARKE, N. M.; DONADILLE, L.; FREER, M.; LEASK, P. J.; SINGER, S. M.; NICOLI, M. P.; BENOIT, B.; HANAPPE, F.; NINANE, A.; ORR, N. A.; TILLIER, J.; STUTTGÉ, L. Exclusive breakup measurements for ^{9}Be. *Phys. Rev. C*, American Physical Society, v. 70, p. 047602, Oct 2004. Disponível em: <https://link.aps.org/doi/10.1103/PhysRevC.70.047602>.

70 ASHWOOD, N. I.; FREER, M.; MILLENER, D. J.; ORR, N. A.; CARSTOIU, F.; AHMED, S.; ANGÉLIQUE, J. C.; BOUCHAT, V.; CATFORD, W. N.; CLARKE, N. M.; CURTIS, N.; HANAPPE, F.; HOROI, M.; KERCKX, Y.; LECOUEY, J. L.; MARQUÉS, F. M.; MATERNA, T.; NORMAND, G.; PAIN, S.; ć, N. Soi; TIMIS, C.; UNSHAKOVA, A.; ZIMAN, V. A. High-energy two-neutron removal from ^{10}Be. *Phys. Rev. C*, American Physical Society, v. 72, p. 024314, Aug 2005. Disponível em: <https://link.aps.org/doi/10.1103/PhysRevC.72.024314>.

71 PAPKA, P.; BROWN, T. A. D.; FULTON, B. R.; WATSON, D. L.; FOX, S. P.; GROOMBRIDGE, D.; FREER, M.; CLARKE, N. M.; ASHWOOD, N. I.; CURTIS, N.; ZIMAN, V.; MCEWAN, P.; AHMED, S.; CATFORD, W. N.; MAHBOUB, D.; TIMIS, C. N.; BALDWIN, T. D.; WEISSER, D. C. Decay path measurements for the 2.429 mev state in ^{9}Be: Implications for the astrophysical $\alpha + \alpha + n$ reaction. *Phys. Rev. C*, American Physical Society, v. 75, p. 045803, Apr 2007. Disponível em: <https://link.aps.org/doi/10.1103/PhysRevC.75.045803>.

72 BROWN, T. A. D.; PAPKA, P.; FULTON, B. R.; WATSON, D. L.; FOX, S. P.; GROOMBRIDGE, D.; FREER, M.; CLARKE, N. M.; ASHWOOD, N. I.; CURTIS, N.; ZIMAN, V.; MCEWAN, P.; AHMED, S.; CATFORD, W. N.; MAHBOUB, D.; TIMIS, C. N.; BALDWIN, T. D.; WEISSER, D. C. Decay studies for states in ^{9}Be up to 11 mev: Insights into the n+^{8}Be and α+^{5}He cluster structure. *Phys. Rev. C*, American Physical Society, v. 76, p. 054605, Nov 2007. Disponível em: <https://link.aps.org/doi/10.1103/PhysRevC.76.054605>.

73 TILLEY, D.; KELLEY, J.; GODWIN, J.; MILLENER, D.; PURCELL, J.; SHEU, C.; WELLER, H. Energy levels of light nuclei a=8,9,10. *Nuclear Physics A*, v. 745, n. 3, p. 155–362, 2004. ISSN 0375-9474. Disponível em: <https://www.sciencedirect.com/science/article/pii/S0375947404010267>.

74 BURDA, O.; NEUMANN-COSEL, P. von; RICHTER, A.; FORSSÉN, C.; BROWN, B. A. Resonance parameters of the first $1/2^+$ state in ^{9}Be and astrophysical implications. *Phys. Rev. C*, American Physical Society, v. 82, p. 015808, Jul 2010. Disponível em: <https://link.aps.org/doi/10.1103/PhysRevC.82.015808>.

75 ARNOLD, C. W.; CLEGG, T. B.; ILIADIS, C.; KARWOWSKI, H. J.; RICH, G. C.; TOMPKINS, J. R.; HOWELL, C. R. Cross-section measurement of ^{9}be$(\gamma, n)^{8}$be and implications for $\alpha + \alpha + n \rightarrow {}^{9}$be in the r process. *Phys. Rev. C*, American Physical Society, v. 85, p. 044605, Apr 2012. Disponível em: <https://link.aps.org/doi/10.1103/PhysRevC.85.044605>.

76 GOLLAN, F.; ABRIOLA, D.; ARAZI, A.; CARDONA, M.; BARBARÁ, E. de; HOJMAN, D.; BETAN, R. I.; MARTI, G.; PACHECO, A.; RODRIGUES, D. *et al.* Energy dependence of the optical potential of the weakly bound 9be projectile on the 197au target. *Nuclear Physics A*, Elsevier, v. 1000, p. 121789, 2020.

77 THOMPSON, I. J. I. j. thompson, comput. phys. rep. 7, 167 (1988). *Comput. Phys. Rep.*, v. 7, p. 167, 1988.

78 BARNARD, E.; VILLIERS, J. D.; ENGELBRECHT, C.; REITMANN, D. The level structure of 197au. *Nucl. Phys. A*, Elsevier, v. 167, n. 3, p. 511–528, 1971.

79 GASQUES, L.; CHAMON, L.; GOMES, P.; LUBIAN, J. Comparison between heavy-ion reaction and fusion processes for hundreds of systems. *Nuclear Physics A*, v. 764, p. 135–148, 2006. ISSN 0375-9474. Disponível em: <https://www.sciencedirect.com/science/article/pii/S0375947405010870>.

80 UMBELINO, U.; PIRES, K. C. C.; LICHTENTHÄLER, R.; SCARDUELLI, V.; SCOTTON, G. A.; LÉPINE-SZILY, A.; AES, V. G.; LUBIAN, J.; PAES, B.; FERREIRA, J. L.; ALVAREZ, M. A. G.; SHORTO, J. M. B.; APPANNABABU, S.; AO, M. Assun ç CONDORI, R. P.; MORCELLE, V. Two-neutron transfer in ^{7}Be + ^{9}Be collisions. *Phys. Rev. C*, American Physical Society, v. 99, p. 064617, Jun 2019. Disponível em: <https://link.aps.org/doi/10.1103/PhysRevC.99.064617>.

81 *NuShellX for Windows and Linux http://www.garsington.eclipse.co.uk/.*

82 MORO, A. Private Communication.

83 UTSUNO, Y.; CHIBA, S. Multiparticle-multihole states around ^{16}O and correlation-energy effect on the shell gap. *Phys. Rev. C*, American Physical Society, v. 83, p. 021301, Feb 2011. Disponível em: <https://link.aps.org/doi/10.1103/PhysRevC.83.021301>.

84 HUDAN, S.; DESOUZA, R. T.; UMAR, A. S.; LIN, Z.; HOROWITZ, C. J. Enhanced dynamics in fusion of neutron-rich oxygen nuclei at above-barrier energies. *Phys. Rev. C*, American Physical Society, v. 101, p. 061601, Jun 2020. Disponível em: <https://link.aps.org/doi/10.1103/PhysRevC.101.061601>.

85 DESOUZA, R.; SINGH, V.; HUDAN, S.; LIN, Z.; HOROWITZ, C. Effect of increasing neutron-excess on the fusion cross-section in 1215c + 12c at above-barrier energies. *Physics Letters B*, v. 814, p. 136115, 2021. ISSN 0370-2693. Disponível em: <https://www.sciencedirect.com/science/article/pii/S0370269321000551>.

86 UMAR, A. S.; OBERACKER, V. E.; HOROWITZ, C. J. Microscopic sub-barrier fusion calculations for the neutron star crust. *Phys. Rev. C*, American Physical Society, v. 85, p. 055801, May 2012. Disponível em: <https://link.aps.org/doi/10.1103/PhysRevC.85.055801>.

87 FURNSTAHL, R. The unedf project. *Nuclear Physics News*, Taylor Francis, v. 21, n. 2, p. 18–24, 2011. Disponível em: <https://doi.org/10.1080/10619127.2011.581139>.

88 GASQUES, L. R.; CHAMON, L. C.; PEREIRA, D.; ALVAREZ, M. A. G.; ROSSI, E. S.; SILVA, C. P.; CARLSON, B. V. Global and consistent analysis of the heavy-ion elastic scattering and fusion processes. *Phys. Rev. C*, American Physical Society, v. 69, p. 034603, Mar 2004. Disponível em: <https://link.aps.org/doi/10.1103/PhysRevC.69.034603>.

89 GASQUES, L. R.; AFANASJEV, A. V.; BEARD, M.; LUBIAN, J.; NEFF, T.; WIESCHER, M.; YAKOVLEV, D. G. São paulo potential as a tool for calculating *s* factors of fusion reactions in dense stellar matter. *Phys. Rev. C*, American Physical Society, v. 76, p. 045802, Oct 2007. Disponível em: <https://link.aps.org/doi/10.1103/PhysRevC.76.045802>.

90 BECKERMAN, M.; SALOMAA, M.; SPERDUTO, A.; ENGE, H.; BALL, J.; DIRIENZO, A.; GAZES, S.; CHEN, Y.; MOLITORIS, J. D.; NAI-FENG, M. Dynamic influence of valence neutrons upon the complete fusion of massive nuclei. *Phys. Rev. Lett.*, American Physical Society, v. 45, p. 1472–1475, Nov 1980. Disponível em: <https://link.aps.org/doi/10.1103/PhysRevLett.45.1472>.

91 STOKSTAD, R. G.; GROSS, E. E. Analysis of the sub-barrier fusion of ^{16}O+^{148,150,152,154}Sm. *Phys. Rev. C*, American Physical Society, v. 23, p. 281–294, Jan 1981. Disponível em: <https://link.aps.org/doi/10.1103/PhysRevC.23.281>.

92 ABRIOLA, D.; DIGREGORIO, D.; TESTONI, J. E.; ETCHEGOYEN, A.; ETCHEGOYEN, M. C.; NIELLO, J. O. F.; FERRERO, A. M. J.; GIL, S.; MACCHIAVELLI, A. O.; PACHECO, A. J.; KITTL, J. Energy dependence of the optical potential for the ^{16}O+^{144}Sm system near the coulomb barrier. *Phys. Rev. C*, American Physical Society, v. 39, p. 546–552, Feb 1989. Disponível em: <https://link.aps.org/doi/10.1103/PhysRevC.39.546>.

93 FISICHELLA, M.; SHOTTER, A. C.; FIGUERA, P.; LUBIAN, J.; PIETRO, A. D.; FERNANDEZ-GARCIA, J. P.; FERREIRA, J. L.; LATTUADA, M.; LOTTI, P.; MUSUMARRA, A.; PELLEGRITI, M. G.; RUIZ, C.; SCUDERI, V.; STRANO, E.; TORRESI, D.; ZADRO, M. Breakup and n-transfer effects on the fusion reactions ^{6,7}Li +^{120,119} Sn around the coulomb barrier. *Phys. Rev. C*, American Physical Society, v. 95, p. 034617, Mar 2017. Disponível em: <https://link.aps.org/doi/10.1103/PhysRevC.95.034617>.

94 CANTO, L.; GOMES, P.; DONANGELO, R.; LUBIAN, J.; HUSSEIN, M. Recent developments in fusion and direct reactions with weakly bound nuclei. *Physics Reports*, v. 596, p. 1–86, 2015. ISSN 0370-1573. Recent developments in fusion and direct reactions with weakly bound nuclei. Disponível em: <https://www.sciencedirect.com/science/article/pii/S0370157315003385>.

95 CARLSON, B. V.; HIRATA, D. Dirac-hartree-bogoliubov approximation for finite nuclei. *Phys. Rev. C*, American Physical Society, v. 62, p. 054310, Oct 2000. Disponível em: <https://link.aps.org/doi/10.1103/PhysRevC.62.054310>.

96 CHAMON, L.; CARLSON, B.; GASQUES, L. São paulo potential version 2 (spp2) and brazilian nuclear potential (bnp). *Computer Physics Communications*, v. 267, p. 108061, 2021. ISSN 0010-4655. Disponível em: <https://www.sciencedirect.com/science/article/pii/S0010465521001739>.

97 RAMAN, S.; NESTOR, C.; TIKKANEN, P. Transition probability from the ground to the first-excited 2+ state of even–even nuclides. *Atomic Data and Nuclear Data Tables*, v. 78, n. 1, p. 1–128, 2001. ISSN 0092-640X. Disponível em: <https://www.sciencedirect.com/science/article/pii/S0092640X01908587>.

98 MONTAGNOLI, G.; STEFANINI, A. M.; ESBENSEN, H.; JIANG, C. L.; CORRADI, L.; COURTIN, S.; FIORETTO, E.; GOASDUFF, A.; GREBOSZ, J.; HAAS, F.; MAZZOCCO, M.; MICHELAGNOLI, C.; MIJATOVIC, T.; MONTANARI, D.; PARASCANDOLO, C.; REHM, K. E.; SCARLASSARA, F.; SZILNER, S.; TANG, X. D.; UR, C. A. Effects of transfer channels on near- and sub-barrier fusion of $^{\mathbf{32}}$s + $^{\mathbf{48}}$ca. *Phys. Rev. C*, American Physical Society, v. 87, p. 014611, Jan 2013. Disponível em: <https://link.aps.org/doi/10.1103/PhysRevC.87.014611>.

99 TROTTA, M.; STEFANINI, A. M.; CORRADI, L.; GADEA, A.; SCARLASSARA, F.; BEGHINI, S.; MONTAGNOLI, G. Sub-barrier fusion of the magic nuclei ^{40,48}Ca+^{48}Ca. *Phys. Rev. C*, American Physical Society, v. 65, p. 011601, Dec 2001. Disponível em: <https://link.aps.org/doi/10.1103/PhysRevC.65.011601>.

100 STEFANINI, A. M.; ACKERMANN, D.; CORRADI, L.; NAPOLI, D. R.; PETRACHE, C.; SPOLAORE, P.; BEDNARCZYK, P.; ZHANG, H. Q.; BEGHINI, S.; MONTAGNOLI, G.; MUELLER, L.; SCARLASSARA, F.; SEGATO, G. F.; SORAMEL, F.; ROWLEY, N. Influence of complex surface vibrations on the fusion of ^{58}Ni + ^{60}Ni. *Phys. Rev. Lett.*, American Physical Society, v. 74, p. 864–867, Feb 1995. Disponível em: <https://link.aps.org/doi/10.1103/PhysRevLett.74.864>.

101 TIMMERS, H.; CORRADI, L.; STEFANINI, A.; ACKERMANN, D.; HE, J.; BEGHINI, S.; MONTAGNOLI, G.; SCARLASSARA, F.; SEGATO, G.; ROWLEY, N. Strong isotopic dependence of the fusion of 40ca + 90,96zr. *Physics Letters B*, v. 399, n. 1, p. 35–39, 1997. ISSN 0370-2693. Disponível em: <https://www.sciencedirect.com/science/article/pii/S0370269397002736>.

102 TIMMERS, H.; ACKERMANN, D.; BEGHINI, S.; CORRADI, L.; HE, J.; MONTAGNOLI, G.; SCARLASSARA, F.; STEFANINI, A.; ROWLEY, N. A case study of collectivity, transfer and fusion enhancement. *Nuclear Physics A*, v. 633, n. 3, p. 421–445, 1998. ISSN 0375-9474. Disponível em: <https://www.sciencedirect.com/science/article/pii/S0375947498001213>.

103 STEFANINI, A. M.; SCARLASSARA, F.; BEGHINI, S.; MONTAGNOLI, G.; SILVESTRI, R.; TROTTA, M.; BEHERA, B. R.; CORRADI, L.; FIORETTO, E.; GADEA, A.; WU, Y. W.; SZILNER, S.; ZHANG, H. Q.; LIU, Z. H.; RUAN, M.; YANG, F.; ROWLEY, N. Fusion of ^{48}Ca +^{90,96} Zr above and below the coulomb barrier. *Phys. Rev. C*, American Physical Society, v. 73, p. 034606, Mar 2006. Disponível em: <https://link.aps.org/doi/10.1103/PhysRevC.73.034606>.

104 STEFANINI, A.; MONTAGNOLI, G.; ESBENSEN, H.; CORRADI, L.; COURTIN, S.; FIORETTO, E.; GOASDUFF, A.; GREBOSZ, J.; HAAS, F.; MAZZOCCO, M.; MICHELAGNOLI, C.; MIJATOVIć, T.; MONTANARI, D.; PASQUALATO, G.; PARASCANDOLO, C.; SCARLASSARA, F.; STRANO, E.; SZILNER, S.; TORRESI, D. Fusion of 40ca + 96zr revisited: Transfer couplings and hindrance far below the barrier. *Physics Letters B*, v. 728, p. 639–644, 2014. ISSN 0370-2693. Disponível em: <https://www.sciencedirect.com/science/article/pii/S037026931301023X>.

105 MA, W. H.; PATEL, D.; YANG, Y. Y.; WANG, J. S.; KANADA-EN'YO, Y.; CHEN, R. F.; LUBIAN, J.; YE, Y. L.; YANG, Z. H.; REN, Z. Z.; MUKHERJEE, S.; MA, J. B.; JIN, S. L.; MA, P.; LI, J. X.; SONG, Y. S.; HU, Q.; BAI, Z.; HUANG, M. R.; LIU, X. Q.; ZHOU, Y. J.; CHEN, J.; GAO, Z. H.; DUAN, F. F.; JIN, S. Y.; XU, S. W.; YU, G. M.; SHI, G. Z.; WANG, Q.; WANG, T. F.; JU, X. Y.; HU, Z. G.; ZHANG, Y. H.; ZHOU, X. H.; XU, H. S.; XIAO, G. Q.; ZHAN, W. L. Observation of ^{6}He $+ t$ cluster states in ^{9}Li. *Phys. Rev. C*, American Physical Society, v. 103, p. L061302, Jun 2021. Disponível em: <https://link.aps.org/doi/10.1103/PhysRevC.103.L061302>.

106 RAABE, R.; SIDA, J. L.; CHARVET, J. L.; ALAMANOS, N.; ANGULO, C.; CASANDJIAN, J. M.; COURTIN, S.; DROUART, A.; DURAND, D. J. C.; FIGUERA, P.; GILLIBERT, A.; HEINRICH, S.; JOUANNE, C.; LAPOUX, V.; LEPINE-SZILY, A.;

MUSUMARRA, A.; NALPAS, L.; PIERROUTSAKOU, D.; ROMOLI, M.; RUSEK, K.; TROTTA, M. No enhancement of fusion probability by the neutron halo of 6he. *Nature*, Nature Publishing Group, v. 431, n. 7010, p. 823–826, 2004.

107 BARIONI, A.; ZAMORA, J. C.; AES, V. G.; PAES, B.; LUBIAN, J.; AGUILERA, E. F.; KOLATA, J. J.; ROBERTS, A. L.; BECCHETTI, F. D.; VILLANO, A.; OJARUEGA, M.; JIANG, H. Elastic scattering and total reaction cross sections for the ^{8}B, ^{7}Be, and ^{6}Li +^{12}c systems. *Phys. Rev. C*, American Physical Society, v. 84, p. 014603, Jul 2011. Disponível em: <https://link.aps.org/doi/10.1103/PhysRevC.84.014603>.

108 LUBIAN, J.; CORREA, T.; AGUILERA, E. F.; CANTO, L. F.; GOMEZ-CAMACHO, A.; QUIROZ, E. M.; GOMES, P. R. S. Effects of breakup couplings on ^{8}B +^{58} Ni elastic scattering. *Phys. Rev. C*, American Physical Society, v. 79, p. 064605, Jun 2009. Disponível em: <https://link.aps.org/doi/10.1103/PhysRevC.79.064605>.

109 RANGEL, J.; LUBIAN, J.; CANTO, L.; GOMES, P. Effect of coulomb breakup on the elastic cross section of the b 8 proton-halo projectile on a heavy, pb 208 target. *Physical Review C*, APS, v. 93, n. 5, p. 054610, 2016.

110 DESCOUVEMONT, P.; BAYE, D. Microscopic theory of the ^{8}Be(α,γ)^{12}c reaction in a three-cluster model. *Phys. Rev. C*, American Physical Society, v. 36, p. 54–59, Jul 1987. Disponível em: <https://link.aps.org/doi/10.1103/PhysRevC.36.54>.

111 ZHANG, G. L.; ZHANG, G. X.; LIN, C. J.; LUBIAN, J.; RANGEL, J.; PAES, B.; FERREIRA, J. L.; ZHANG, H. Q.; QU, W. W.; JIA, H. M.; YANG, L.; MA, N. R.; SUN, L. J.; WANG, D. X.; ZHENG, L.; LIU, X. X.; CHU, X. T.; YANG, J. C.; WANG, J. S.; XU, S. W.; MA, P.; MA, J. B.; JIN, S. L.; BAI, Z.; HUANG, M. R.; ZANG, H. L.; YANG, B.; LIU, Y. Angular distribution of elastic scattering induced by ^{17}F on medium-mass target nuclei at energies near the coulomb barrier. *Phys. Rev. C*, American Physical Society, v. 97, p. 044618, Apr 2018. Disponível em: <https://link.aps.org/doi/10.1103/PhysRevC.97.044618>.

112 KEELEY, N.; RAABE, R.; ALAMANOS, N.; SIDA, J. Fusion and direct reactions of halo nuclei at energies around the coulomb barrier. *Progress in Particle and Nuclear Physics*, v. 59, n. 2, p. 579–630, 2007. ISSN 0146-6410. Disponível em: <https://www.sciencedirect.com/science/article/pii/S0146641007000397>.

113 KEELEY, N.; ALAMANOS, N.; KEMPER, K.; RUSEK, K. Elastic scattering and reactions of light exotic beams. *Progress in Particle and Nuclear Physics*, v. 63, n. 2, p. 396–447, 2009. ISSN 0146-6410. Disponível em: <https://www.sciencedirect.com/science/article/pii/S0146641009000519>.

114 KOLATA, J.; GUIMARÃES, V.; AGUILERA, E. Elastic scattering, fusion, and breakup of light exotic nuclei. *The European Physical Journal A*, Springer, v. 52, n. 5, p. 1–38, 2016.

115 CANTO, L.; GUIMARÃES, V.; LUBIÁN, J.; HUSSEIN, M. The total reaction cross section of heavy-ion reactions induced by stable and unstable exotic beams: the low-energy regime. *The European Physical Journal A*, Springer, v. 56, n. 11, p. 1–44, 2020.

116 PANDIT, S. K.; JHA, V.; MAHATA, K.; SANTRA, S.; PALSHETKAR, C. S.; RAMACHANDRAN, K.; PARKAR, V. V.; SHRIVASTAVA, A.; KUMAWAT, H.; ROY, B. J.; CHATTERJEE, A.; KAILAS, S. Investigation of cluster structure of ^{9}be from high precision elastic scattering data. *Phys. Rev. C*, American Physical Society, v. 84, p. 031601, Sep 2011. Disponível em: <https://link.aps.org/doi/10.1103/PhysRevC.84.031601>.

117 KEELEY, N.; KEMPER, K. W.; RUSEK, K. ^{5}He$+\alpha$ cluster model of ^{9}Be breakup. *Phys. Rev. C*, American Physical Society, v. 64, p. 031602, Aug 2001. Disponível em: <https://link.aps.org/doi/10.1103/PhysRevC.64.031602>.

118 PARKAR, V. V.; JHA, V.; PANDIT, S. K.; SANTRA, S.; KAILAS, S. Exploring the breakup and transfer coupling effects in ^{9}be elastic scattering. *Phys. Rev. C*, American Physical Society, v. 87, p. 034602, Mar 2013. Disponível em: <https://link.aps.org/doi/10.1103/PhysRevC.87.034602>.

119 RODRÍGUEZ-GALLARDO, M.; ARIAS, J.; GÓMEZ-CAMACHO, J.; JOHNSON, R.; MORO, A.; THOMPSON, I.; TOSTEVIN, J. Continuum effects: Structure and reactions of 6he. *The European Physical Journal Special Topics*, Springer, v. 150, n. 1, p. 51–52, 2007.

120 FARIA, P. N. de; LICHTENTHÄLER, R.; PIRES, K. C. C.; MORO, A. M.; LÉPINE-SZILY, A.; AES, V. G.; MENDES, D. R.; ARAZI, A.; RODRÍGUEZ-GALLARDO, M.; BARIONI, A.; MORCELLE, V.; MORAIS, M. C.; CAMARGO, O.; NEZ, J. A. N.; AO, M. Assun çĖlastic scattering and total reaction cross section of ^{6}He $+^{120}$ Sn. *Phys. Rev. C*, American Physical Society, v. 81, p. 044605, Apr 2010. Disponível em: <https://link.aps.org/doi/10.1103/PhysRevC.81.044605>.

121 PIRES, K. C. C.; LICHTENTHÄLER, R.; LÉPINE-SZILY, A.; AES, V. G.; FARIA, P. N. de; BARIONI, A.; JUNIOR, D. R. M.; MORCELLE, V.; CONDORI, R. P.; MORAIS, M. C.; ZAMORA, J. C.; CREMA, E.; MORO, A. M.; RODRÍGUEZ-GALLARDO, M.; AO, M. Assun ç SHORTO, J. M. B.; MUKHERJEE, S. Experimental study of ^{6}He $+^{9}$ Be elastic scattering at low energies. *Phys. Rev. C*, American Physical Society, v. 83, p. 064603, Jun 2011. Disponível em: <https://link.aps.org/doi/10.1103/PhysRevC.83.064603>.

122 MATSUMOTO, T.; HIYAMA, E.; OGATA, K.; ISERI, Y.; KAMIMURA, M.; CHIBA, S.; YAHIRO, M. Continuum-discretized coupled-channels method for four-body nuclear breakup in he 6+ c 12 scattering. *Physical Review C*, APS, v. 70, n. 6, p. 061601, 2004.

123 EGAMI, T.; MATSUMOTO, T.; OGATA, K.; YAHIRO, M. Description of four-body breakup reaction with the method of continuum-discretized coupled-channels. *Progress of Theoretical Physics*, Oxford University Press, v. 121, n. 4, p. 789–807, 2009.

124 DESCOUVEMONT, P.; DRUET, T.; CANTO, L. F.; HUSSEIN, M. S. Low-energy ^{9}Be $+^{208}$ Pb scattering, breakup, and fusion within a four-body model. *Phys. Rev. C*, American Physical Society, v. 91, p. 024606, Feb 2015. Disponível em: <https://link.aps.org/doi/10.1103/PhysRevC.91.024606>.

125 TILLEY, D.; CHEVES, C.; GODWIN, J.; HALE, G.; HOFMANN, H.; KELLEY, J.; SHEU, C.; WELLER, H. Energy levels of light nuclei a= 5, 6, 7. *Nuclear Physics A*, Elsevier, v. 708, n. 1-2, p. 3–163, 2002.

126 BANG, J.; GIGNOUX, C. A realistic three-body model of 6li with local interactions. *Nuclear Physics A*, v. 313, n. 1, p. 119–140, 1979. ISSN 0375-9474. Disponível em: <https://www.sciencedirect.com/science/article/pii/0375947479905712>.

127 ARAI, K.; SUZUKI, Y.; LOVAS, R. G. Structure of ^{6}He with an extended three-cluster model. *Phys. Rev. C*, American Physical Society, v. 59, p. 1432–1439, Mar 1999. Disponível em: <https://link.aps.org/doi/10.1103/PhysRevC.59.1432>.

128 THOMPSON, I.; NUNES, F.; DANILIN, B. Face: a tool for three body faddeev calculations with core excitation. *Computer physics communications*, Elsevier, v. 161, n. 1-2, p. 87–107, 2004.

129 THOMPSON, I. J. *Sturmxx*. <www.fresco.org.uk/programs/sturmxx/index.html>, Last accessed on 2020-01-08.

130 THOMPSON, I. J. Ij thompson, comput. phys. rep. 7, 167 (1988). *Comput. Phys. Rep.*, v. 7, p. 167, 1988.

131 AVRIGEANU, M.; VON OERTZEN, W.; PLOMPEN, A.; AVRIGEANU, V. Optical model potentials for -particles scattering around the coulomb barrier on a100 nuclei. *Nuclear Physics A*, v. 723, n. 1, p. 104–126, 2003. ISSN 0375-9474. Disponível em: <https://www.sciencedirect.com/science/article/pii/S037594740301159X>.

132 MORCELLE, V.; PIRES, K.; RODRíGUEZ-GALLARDO, M.; LICHTENTHäLER, R.; LéPINE-SZILY, A.; GUIMARãES, V.; de Faria, P.; Mendes Junior, D.; MORO, A.; GASQUES, L.; LEISTENSCHNEIDER, E.; Pampa Condori, R.; SCARDUELLI, V.; MORAIS, M.; BARIONI, A.; ZAMORA, J.; SHORTO, J. Four-body effects in the he6+ni58 scattering. *Physics Letters B*, v. 732, p. 228–232, 2014. ISSN 0370-2693. Disponível em: <https://www.sciencedirect.com/science/article/pii/S0370269314001993>.